POLITECNICO
MILANO 1863

SCUOLA DI INGEGNERIA INDUSTRIALE
E DELL'INFORMAZIONE

Executive Summary of the Thesis

Numerical modelling of cavitation effects in blood flows

Laurea Magistrale in Aeronautical Engineering - Ingegneria Aeronautica

Author: Matteo Zemello

Advisor: Prof. Luca Dedè

Co-advisors: Prof. Stefano Berrone, Dr. Ivan Fumagalli, Michele Bucelli

Academic year: 2020-2021

1. Introduction

This thesis aims at developing a stabilized finite element method for numerical modeling of cavitating flows, with a specific focus on cavitation effects in blood flows.
Cavitation is a phenomenon in which the static pressure of a liquid reduces to below the liquid's vapor pressure, leading to the formation of small vapor-filled cavities. Cavitation is quite an ubiquitous phenomenon both in natural and industrial processes; experimental evidence proved that it occurs also in the human cardiocirculatory system, the most common cause being interaction of blood with valves regulating the flow, especially when they are replaced by mechanical prostheses [2]. The occurrence of this phenomenon entails several drawbacks: when vapor bubbles collapse, they can damage the prostheses structure and the blood cells, resulting in an enhanced erosion of the valve's leaflets and promoting thrombus formation. It is clear, therefore, that being able to predict and model cavitation has considerable implications in clinical applications.
Despite several experiments, numerical simulations on cavitation effects in blood flows are limited. To bridge this gap, we proposed a numerical model able to include cavitation effects and predict the occurrence of cavitation. We developed a volume of fluid (VOF) model, in which the fluid is considered as an homogeneous mixture of liquid and vapor phase, and the evolution of the vapor fraction is described by an advection-diffusion-reaction equation coupled to the mass and momentum conservation equations of the mixture. We adopted the Zwart model [5] to derive the expression of the liquid-vapor mass transfer.
The cavitation model is discretized by means of SUPG-stabilized finite elements. For spatial discretization we relied on piecewise linear Lagrangian polynomials; time discretization was performed by means of finite differences, specifically Backward Differentation Formulas (BDF) of order one. The fluid flow and cavitation solvers have been implemented in `life`$^{\texttt{x}}$ [1], a C++ FE library under development at MOX laboratories at Politecnico di Milano, mainly focused on cardiac applications. The two solvers have been coupled in a staggered partitioned manner for versatility: at each timestep, the vapor fraction distribution is determined first, and then the homogeneous mixture equations are solved for pressure and mixture velocity.
We tested the model on different benchmarks:

- flow past a circular cylinder;
- flow in a nozzle benchmark proposed by the

Food and Drug Administration (FDA);
- flow past an idealized bileaflet valve geometry.

We show how the model predicts the occurrence of cavitation and the relevant flow features such as the pressure distribution, the divergence of the velocity field and the shear stresses. In the following, we present the mathematical and numerical model, and finally the numerical results.

2. Mathematical model

Let Ω be the physical domain and let $\Gamma = \partial\Omega$ be its boundary. We denote with $\mathbf{x} \in \Omega$ the spatial coordinates and with $t \in (0, T]$ the temporal coordinate. In the framework of the VOF methods, we define the volume vapor fraction:

$$\alpha(\mathbf{x}, t) = \frac{V_v}{V_m}, \tag{1}$$

where V_v is the volume of the vapor phase and V_m is the volume of the mixture. Once the phase indicator is defined, we denote with ρ_m and μ_m the density and viscosity of the mixture:

$$\rho_m = \alpha\rho_v + (1-\alpha)\rho_v, \tag{2}$$
$$\mu_m = \alpha\rho_v + (1-\alpha)\rho_v, \tag{3}$$

where ρ_v and ρ_l are the constant vapor and liquid densities. The same holds for viscosity.
To obtain the final form of the cavitation model, we couple the mixture mass and momentum conservation system with the equation of the net vapor phase as follows.
The mixture mass and momentum system reads:

$$\begin{cases} \dfrac{\partial\rho_m}{\partial t} + \nabla\cdot(\rho_m\mathbf{u}) = 0, & \text{in } \Omega\times(0,T], \\ \dfrac{\partial(\rho_m\mathbf{u})}{\partial t} + \nabla\cdot(\rho_m\mathbf{u}\otimes\mathbf{u}) = \\ \qquad -\nabla P + \nabla\cdot(2\mu\nabla^S(\mathbf{u})), & \text{in } \Omega\times(0,T], \end{cases} \tag{4}$$

where $\mathbf{u}(\mathbf{x}, t) \in \mathbb{R}^3$ is the mixture velocity, $P(\mathbf{x}, t) \in \mathbb{R}$ is the pressure and the symmetric gradient is defined as: $\nabla^S(\mathbf{u}) = 1/2(\nabla\mathbf{u}+\nabla\mathbf{u}^T)$.
The equation for the vapor phase reads [5]:

$$\frac{\partial\alpha}{\partial t} + \nabla\cdot(\alpha\mathbf{u}) + \kappa\Delta\alpha = \frac{\dot{S}_\alpha(\alpha, P)}{\rho_v}, \quad \text{in } \Omega\times(0,T], \tag{5}$$

where $\dot{S}_\alpha$ is the liquid-vapor mass transfer term, specific to the cavitation model and κ is a diffusion parameter introduced in this formulation to regularize the interfaces between fluid volumes with null and finite value of α and facilitate the numerical solution of the equation for α.
The expression of the liquid-vapor mass transfer rate $\dot{S}_\alpha$ is developed following the model proposed by Zwart et al. [5]. We start from the Rayleigh-Plesset equation, describing the growth of a vapor bubble in a liquid:

$$R_B\frac{d^2R_B}{dt^2} + \frac{3}{2}(\frac{dR_B}{dt})^2 + \frac{2\sigma}{R_B} = \frac{P - P_v}{\rho_l}, \tag{6}$$

where R_B represents the bubble radius, σ represents the surface tension coefficient and P_v is the vapor pressure. Zwart proposed to simplify the second order terms and introduce some dimensional arguments, resulting in the following expression for the mass transfer rate:

$$\dot{S}_\alpha(\alpha, P) = \underbrace{F_{vap}\frac{3r_{nuc}(1-\alpha)\rho_v}{R_B}\sqrt{\frac{2}{3}\frac{\max(P_v - P, 0)}{\rho_l}}}_{\text{(vaporization)}} - \underbrace{F_{cond}\frac{3\alpha\rho_v}{R_B}\sqrt{\frac{2}{3}\frac{\max(P - P_v, 0)}{\rho_l}}}_{\text{(condensation)}}. \tag{7}$$

The positive contribution describes vaporization and depends on the nucleation site radius R_B, the nucleation volume fraction r_{nuc} and a user defined calibration coefficient F_{vap}; the negative term describes condensation and is proportional to a corresponding calibration coefficient F_{cond}. Zwart et al. [5] have provided values for the model parameters, calibrated to match experimental data for a variety of fluids and devices:

$$\begin{aligned} F_{\text{vap}} &= 50.0 \quad [-], \\ F_{\text{cond}} &= 0.01 \quad [-], \\ r_{\text{nuc}} &= 10^{-4} \quad [-], \\ R_B &= 10^{-6} \quad [m]. \end{aligned}$$

2.1. Coupled problem in strong formulation

The continuous problems (4) and (5) are coupled and the following continuous problem holds; let us assume that Γ is subdivided in a subset Γ_D, where Dirichlet conditions are prescribed, and a subset Γ_N, where Neumann conditions are set, such that $\Gamma = \Gamma_D \cup \Gamma_N$. In a time interval $(0, T]$

with $T > 0$, the problem reads:

$$\begin{cases} \rho\dfrac{\partial \mathbf{u}}{\partial t} + \rho\mathbf{u}\cdot\nabla\mathbf{u} + \nabla P + \\ \quad -\nabla\cdot\big(2\mu\nabla^S(\mathbf{u})\big) = 0 & \text{in } \Omega\times(0,T], \\ \nabla\cdot\mathbf{u} - \Big(\dfrac{1}{\rho_v} - \dfrac{1}{\rho_l}\Big)\dot{S}_\alpha = 0 & \text{in } \Omega\times(0,T], \\ \dfrac{\partial \alpha}{\partial t} + \nabla\cdot(\alpha\mathbf{u}) + \\ \quad -\kappa\Delta\alpha - \dfrac{\dot{S}_\alpha(\alpha,P)}{\rho_v} = 0 & \text{in } \Omega\times(0,T], \\ \mathbf{u} = \mathbf{g}, \qquad \alpha = \gamma & \text{on } \Gamma_D\times(0,T], \\ (-P\mathbf{I} + 2\mu\nabla^S(\mathbf{u}))\cdot\hat{\mathbf{n}} = \mathbf{h} & \text{on } \Gamma_N\times(0,T], \\ (\alpha\mathbf{u} - \kappa\nabla\alpha)\cdot\hat{\mathbf{n}} = \eta & \text{on } \Gamma_N\times(0,T], \\ \mathbf{u} = \mathbf{u}_0, \quad \alpha = \alpha_0 & \text{in } \Omega\times\{0\}. \end{cases} \tag{8}$$

3. Numerical model

Let us define the finite element spaces used for space discretization; Φ^h, V^h and Q^h are introduced for the vapor fraction α^h, the mixture velocity $\mathbf{u}^h$ and the pressure P^h, respectively:

$$\begin{aligned} \Phi^h &:= \Phi \cap X_r^h, \\ \Phi_0^h &:= \Phi_0 \cap X_r^h, \\ \mathcal{V}_g^h &= V_g^h \times Q^h, \\ \mathcal{V}_0^h &= V_0^h \times Q^h, \end{aligned}$$

$$V_g^h := V_g \cap [X_r^h]^3, V_0^h := V_0 \cap [X_r^h]^3, Q^h := Q \cap X_r^h.$$

X_r^h is the space of piecewise Lagrangian polynomial functions of degree $r \geq 1$ on each element K of the partition $\mathcal{T}^h$ of Ω:

$$X_r^h := \{x^h \in C^0(\bar{\Omega}) : x^h|_K \in \mathbb{P}_r, \forall K \in \mathcal{T}^h\}.$$

For time discretization, we employ the Backward Difference Formula (BDF) of order 1 ($\sigma = 1$). Given a uniform timestep, Δt, we denote with x_n^h the approximation of x^h at time $t_n = n\Delta t$. The time derivatives are therefore approximated as:

$$\frac{\partial x^h}{\partial t} \approx \frac{\alpha_\sigma x_{n+1}^h - x_{n,BDF_\sigma}^h}{\Delta t},$$

where $\alpha_\sigma = 1$ and $x_{n,BDF_\sigma}^h = x_n^h$, when $\sigma = 1$. The non-linearities in the convection term of the mixture momentum equation, and the coupling terms in the α transport equation are treated semi-implicitly, extrapolating quantities at time t_{n+1} with Newton-Gregory polynomials. When $\sigma = 1$:

$$\begin{aligned} \mathbf{u}_{n+1,EXT_\sigma}^h &= \mathbf{u}_n^h, \\ P_{n+1,EXT_\sigma}^h &= P_n^h. \end{aligned}$$

In order to numerically solve the coupled problem, a staggered approach is employed: the transport equation of the vapor fraction and the mixture mass and momentum system are solved sequentially at each timestep. In these settings the outline of the solution procedure is the following: We define a uniform partition $t_n = n\Delta t$, $n = 0, 1, \ldots$ of the time interval. The quantities at time t_n are known; then for each $n = 0, 1, \ldots$,

1. Evaluate $\mathbf{u}_{n+1,EXT_\sigma}^h$ and P_{n+1,EXT_σ}^h on the Gaussian quadrature points of the elements of the computational grid;
2. Solve a time step of the SUPG-stabilized, linear discrete vapor transport problem: find $\alpha_{n+1}^h \in \Phi^h$:

$$\begin{aligned} &\Big(\frac{\alpha_\sigma\alpha_{n+1}^h - \alpha_{n,BDF_\sigma}^h}{\Delta t}, \phi^h\Big) - (\alpha_{n+1}^h\mathbf{u}_{n+1,EXT_\sigma}^h, \nabla\phi^h) \\ &+(\kappa\nabla\alpha_{n+1}^h, \nabla\phi^h) - \Big(\frac{\dot{S}_\alpha(\alpha_{n+1}^h, P_{n+1,EXT_\sigma}^h)}{\rho_v}, \phi^h\Big) \\ &+\sum_{K\in\mathcal{T}_h} \Big[\Big(\tau_\phi(\mathbf{u}_{n+1,EXT_\sigma}^h) r_\phi(\alpha_{n+1}^h, \mathbf{u}_{n+1,EXT_\sigma}^h, P_{n+1,EXT_\sigma}^h)\Big), \\ &\frac{1}{2}(\nabla\cdot\mathbf{u}_{n+1,EXT_\sigma}^h)\phi^h + \mathbf{u}_{n+1,EXT_\sigma}^h\cdot\nabla\phi^h\Big)_K\Big] \\ &= \big(\eta_{n+1}, \phi^h\big)_{\Gamma_N}, \end{aligned}$$

   $\forall\phi^h \in \Phi_0^h$, for all $n \geq \sigma - 1$.
   The terms under the sum are the SUPG stabilization terms, where:
   - K denotes a generic cell of $\mathcal{T}_h$;
   - r_ϕ is the residual of the equation for α:

$$\begin{aligned} r_\phi(\alpha^h, \mathbf{u}^h, P^h)) = \frac{\partial\alpha^h}{\partial t} + \nabla\cdot(\alpha^h\mathbf{u}^h) \\ -\kappa\Delta\alpha^h - \frac{\dot{S}_\alpha(\alpha^h, P^h)}{\rho_v}; \end{aligned}$$

   - the stabilization parameter τ_ϕ reads:

$$\begin{aligned} \tau_\phi(\mathbf{u}^h) = \Big[\Big(\frac{\sigma}{\Delta t}\Big)^2 + \mathbf{u}^h\cdot\mathbf{G}\mathbf{u}^h \\ +C_I\kappa^2\mathbf{G}:\mathbf{G} + s^2\Big]^{-1/2}. \end{aligned}$$

   $\mathbf{G}$ is the element controvariant metric tensor: $G_{ij} = \sum_{k=1}^3 \frac{\partial\xi_k}{\partial x_i}\frac{\partial\xi_k}{\partial x_j}$, where $\mathbf{x} = \{x_i\}_{i=1}^3$ are the physical coordinates of element K and $\xi = \{\xi_i\}_{i=1}^3$ the coordinates in parametric space, $C_I = 60\cdot 2^{2-r}$, $s = \frac{\partial\dot{S}_\alpha(\alpha,P)}{\partial\alpha}$.
3. Evaluate α_{n+1}^h on the Gaussian quadrature points of the elements of the computational grid;
4. Solve a time step of the SUPG-stabilized, semi-implicit mixture mass and momentum conservation system:

find $\{\mathbf{u}^h_{n+1}, P^h_{n+1}\} \in \mathcal{V}^h_g$:

$$\begin{aligned}
&\Big(\rho^h(\alpha^h_{n+1})\frac{\alpha_\sigma \mathbf{u}^h_{n+1} - \mathbf{u}^h_{n,BDF_\sigma}}{\Delta t}, \mathbf{v^h}\Big) \\
&+\big(\rho^h(\alpha^h_{n+1})\mathbf{u}^h_{n+1,EXT_\sigma}\cdot\nabla\mathbf{u}^h_{n+1}, \mathbf{v}^h\big) \\
&+(2\mu^h(\alpha^h_{n+1})\nabla^S\mathbf{u}^h_{n+1}, \nabla\mathbf{v}^h) - \big(P^h_{n+1}, \nabla\cdot\mathbf{v}^h\big) \\
&+\big(\nabla\cdot\mathbf{u}^h_{n+1}, q^h\big) \\
&-\Big(\big(\frac{1}{\rho_v}-\frac{1}{\rho_l}\big)\dot{S}_\alpha(\rho^h(\alpha^h_{n+1}), P^h_{n+1}), q^h\Big) \\
+\sum_{K\in\mathcal{T}_h}\Big[&\Big(\tau_M(\mathbf{u}^h_{n+1,EXT_\sigma})\mathbf{r}_M(\alpha^h_{n+1}, \mathbf{u}^h_{n+1}, P^h_{n+1})), \\
&\rho^h\mathbf{u}^h_{n+1,EXT_\sigma}\cdot\nabla\mathbf{v}^h + \nabla q^h\Big)_K + \\
&+\Big(\tau_C(\mathbf{u}^h_{n+1,EXT_\sigma})r_C(\alpha^h_{n+1}, \mathbf{u}^h_{n+1}, P^h_{n+1})), \\
&\nabla\cdot\mathbf{v}^h\Big)_K\Big] = \\
&= (\mathbf{h}_{n+1}, \mathbf{v}^h)_{\Gamma_N},
\end{aligned}$$

$\forall\{\mathbf{v}^h, q^h\} \in \mathcal{V}^h_0$, for all $n \geq \sigma - 1$.

The terms under the sum are the SUPG stabilization terms, where:

- $\mathbf{r}_M$ is the residual of the momentum equation for the mixture:

$$\begin{aligned}
\mathbf{r}_M(\alpha^h, \mathbf{u}^h, P^h) = \rho^h\frac{\partial\mathbf{u}^h}{\partial t} + \rho^h\mathbf{u}^h\cdot\nabla\mathbf{u}^h \\
+\nabla P^h - \mu^h\Delta\mathbf{u}^h;
\end{aligned}$$

- r_C is the residual of the continuity equation for the mixture:

$$\begin{aligned}
r_C(\alpha^h, \mathbf{u}^h, P^h) = \nabla\cdot\mathbf{u}^h \\
-\Big(\frac{1}{\rho_v}-\frac{1}{\rho_l}\Big)\dot{S}_\alpha(\alpha^h, P^h);
\end{aligned} \tag{9}$$

- the stabilization parameter τ_M reads:

$$\begin{aligned}
\tau_M(\alpha^h, \mathbf{u}^h) = \Big[{\rho^h}^2\Big(\frac{\sigma}{\Delta t}\Big)^2 + {\rho^h}^2\mathbf{u}^h\cdot\mathbf{G}\mathbf{u}^h \\
+C_r{\mu^h}^2\mathbf{G}:\mathbf{G}\Big]^{-1/2}
\end{aligned}$$

- the stabilization parameter τ_C reads:

$$\tau_C(\alpha^h, \mathbf{u}^n) = \big(\tau_M\mathbf{g}\cdot\mathbf{g}\big)^{-1}.$$

$C_r = 60\cdot 2^{2-r}$ and $\mathbf{g}$ is the metric tensor defined as: $g_i = \sum_{k=1}^3 \frac{\partial\xi_k}{\partial x_i}$.

We highlight that in the problem solved at step 2, we use the explicit formulation of the pressure P^h_{n+1,EXT_σ} in the definition of $\dot{S}_\alpha$, whereas in step 4, we use the implicit formulation P^h_{n+1}. This is done to foster the staggered solver stability and is supported by an estimate of the energy on the mixture velocity and confirmed by numerical results.

4. Numerical results

In this section we present the numerical results on the three different benchmarks. We first define two dimensionless groups governing the flow: the Reynolds and the cavitation number:

$$\mathbb{R}e = \frac{\rho u D}{\mu}, \tag{10}$$

$$\sigma_{\text{cav}} = \frac{P - P_v}{1/2\rho u^2}, \tag{11}$$

in each of the following sections, we provide the values of these two numbers, as well as the reference velocity u and pressure P for the adimensionalization.

As for the fluid properties, we select the blood literature values for density and viscosity for both liquid and vapor phases at 37°C:

$$\rho_l = 1060 \quad \text{kg/m}^3, \quad \mu_l = 3.30\cdot 10^{-3} \quad \text{Pa·s},$$
$$\rho_v = 0.485 \quad \text{kg/m}^3, \quad \mu_v = 4.71\cdot 10^{-5} \quad \text{Pa·s}.$$

4.1. Numerical simulation of the cavitating cylinder benchmark

As a first benchmark, we study the transient cavitation over a circular cylinder. It allows a simple representation of cavitation phenomena over bluff bodies. We validate and compare results with [3] by choosing the same value for the Reynolds number computed with the inlet velocity: $\mathbb{R}e = 200$. Non-cavitating results ($\sigma_{\text{cav}} = 2.0$) are compared to cavitating results ($\sigma_{\text{cav}} = 1.0$).

As for the boundary conditions, we impose a Dirichlet time evolving ramp velocity profile at the inlet, a no-slip condition on the cylinder surface, zero normal flux on the channel walls and a homogeneous pressure boundary on the outlet. Regarding the vapor fraction α, we impose a homogeneous Dirichlet boundary condition (BC) on the inlet and a homogeneous Neumann BC on the outlet, channel walls and cylinder surface.

As the liquid accelerates past the bluff body, pressure drops in the shear layer, resulting in cavitation inception. The shear layer rolls up into vortexes with cavitating cores, as shown in Figure 1, they are shed from the body into the wake and collapse. The model, compared to [3], predicts accurately:

- the bubble inception location on the cylinder surface, which is at an angle $\theta = 65°$ from the stagnation point;

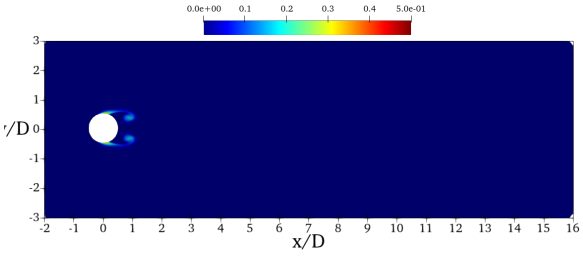

Figure 1: **Instantaneous vapor fraction contour.**

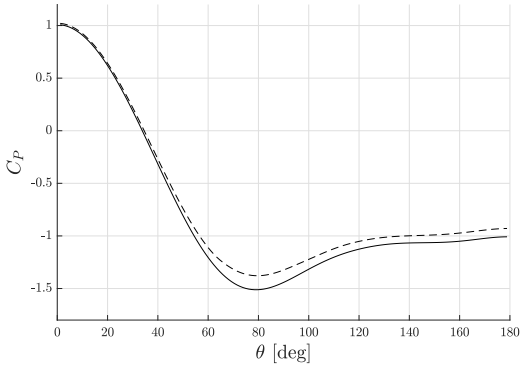

Figure 2: **Mean pressure coefficient distribution on the cylinder surface:** —— $\sigma_{\text{cav}} = 2.0$, - - - $\sigma_{\text{cav}} = 1.0$.

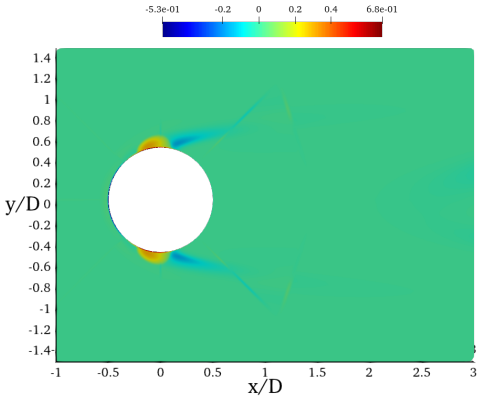

Figure 3: **Divergence of the velocity field.**

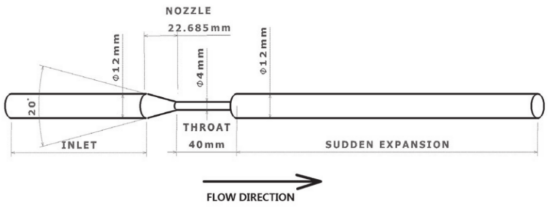

Figure 4: **FDA geometry.** Image taken from [4]

- the decreasing in the magnitude of the minimum value of the pressure coefficient on the cylinder surface $C_P = \frac{P-P_\infty}{1/2\rho_l u_\infty^2}$, plotted in Figure 2. This occurs because once the flow cavitates, the pressure in the vapor region remains close to the vapor pressure;
- the divergence of the velocity field, plotted in Figure 3. Positive values of velocity divergence correspond to vapor bubble formation; negative values of divergence are instead due to some bubble collapsing back to the liquid phase;
- the unsteady loads on the cylinder: cavitation reduces the Strouhal number computed using the vortex shedding frequency by 11%, a similar result is found in [3].

4.2. Numerical simulation of the nozzle FDA benchmark

As second test case we consider the FDA nozzle benchmark. Its geometry was proposed by the US Food and Drug Administration (FDA) as a reference to validate CFD codes for biological simulations of the circulatory system in [4] and is shown in Figure 4. Analogous Venturi-like configurations are typical in mechanical heart valves (MHVs). We evaluate two different sets of boundary conditions at the inlet: a ramp and pulsatile inlet velocity. We set a no-slip boundary condition on the nozzle walls and a pressure BC on the outlet. For α, we set homogeneous Dirichlet on the inlet and homogeneous Neumann on the nozzle walls and at the outlet. The Reynolds number and the cavitation number are computed using the mean velocity in the throat: $\mathbb{R}e = 500$, $\sigma_{\text{cav}} = 0.23$.
The main outcomes are:

- in both the ramp and pulsatile case, when the maximum value of the inlet velocity is reached, a jet develops in the expansion region of the nozzle, resulting in local pressure drops near the front that induce cavitation as shown in Figure 5;
- positive values of vapor fraction are also produced at the end of the throat due to local pressure drops, and accumulated in the region near the step due to the recirculating flow generated by the jet;
- in the case of the pulsatile flow, when the inlet velocity decreases, pressure drops in the whole domain resulting in cavitation in the throat. This is observed also in experimental studies of cavitation across MHVs;
- the shear stresses and the wall shear stresses in the non-cavitating and cavitating case

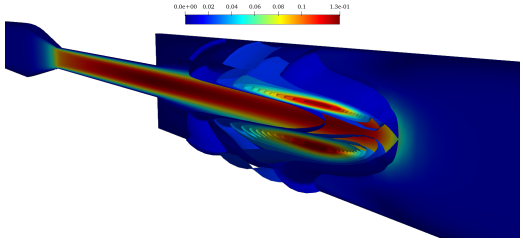

Figure 5: **Tridimensional view of the α contours.** In the backgorund the axial velocity contour is shown.

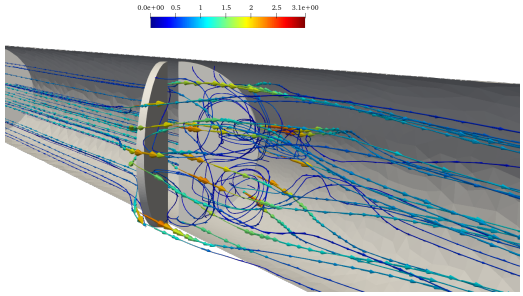

Figure 6: **Flow streamlines colored by velocity magnitude.** Instance at $t = 0.625T$.

are computed. When cavitation is active, the stresses are higher, resulting in an enhanced damage on the nozzle walls and on the blood tissue. This confirms the need to model cavitation to estimate shear stresses in blood flows across MHVs.

4.3. Numerical simulation of an idealized valve geometry

As a third case study, we consider a simplified geometry of a bileaflet MHV, modelled as a straight cylinder with two semicircular leaflets in a fixed position, as shown in Figure 6. We set a homogeneous Dirichlet boundary condition on the inlet for α, and a homogeneous Neumann on the other boundaries (channel wall, outlet, leaflet surface). We set a pulsatile inlet condition on the velocity, no-slip on the channel walls and on the leaflets, and a pressure BC on the outlet. The values of the flow rate, periodicity T, and pressure are chosen accordingly to available data on the mitral valve dynamics.
The main results of this test case are:

- the cavitation model provides good results by means of velocity distribution and turbulent instantaneous structures, visualized through Q-criterion contours: the cavitation model proves suitable for turbulent regimes ($\mathbb{R}e = 4900$);
- we find a peek velocity of 3 m/s across the valve as shown in Figure 6; this value matches the experimental results on squeeze flows across MHVs;
- in the wake, the vapor bubbles have a lifetime of the order of $10 - 20$ ms, this result matches the experimental measurements by [2]. Recirculating flows convey vapor bubbles towards the valve, where they collapse. Figure 7 shows instances of a vapor bubble dynamics. Figure 8 shows the α contour $t = 0.75T$;
- we find larger values of the shear stress if cavitation bubbles interact with the leaflets, with respect to the non-cavitating regions.

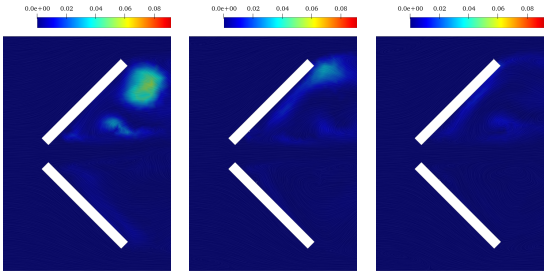

(a) $t = t_0$ (b) $t = t_0 + 20$ ms (c) $t = t_0 + 40$ ms

Figure 7: **Vapor bubble collapse dynamics.**

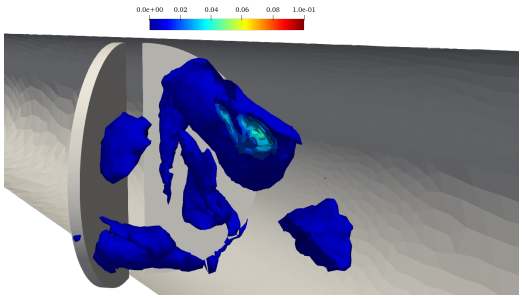

Figure 8: **Tridimensional view of the α contours.**

5. Conclusions

The model showed effective in predicting the occurrence of cavitation, providing consistent results with the literature. Moreover, we demonstrated the relevance of modelling cavitation to accurately predict the flow features such as the pressure distribution, the velocity divergence and the shear stresses, which are crucial to determine the deterioration effects of cavitation on the blood tissue and the valve structure. Nu-

merical results confirmed the efficacy of the proposed method which provides a tool that can be adopted in the MHVs engineering, towards improved designs and clinical applications. Future developments of this work can include tests on more complex and more realistic geometries, as well as extensions to the model to account for the motion of the leaflets, and a coupling with a turbulence model.

References

[1] `life`$^{\texttt{x}}$. `https://lifex.gitlab.io/`.

[2] E. Rambod et al. A physical model describing the mechanism for formation of gas microbubbles in patients with mitral mechanical heart valves. *Annals of Biomedical Engineering*, 1999.

[3] A. Gnanaskandan and K. Mahesh. Numerical investigation of near-wake characteristics of cavitating flow over a circular cylinder. *Journal of Fluid Mechanics*, 2016.

[4] R. Malinauskas, P. Hariharan, and et al. FDA benchmark medical device flow models for CFD validation. *ASAIO journal*, 2017.

[5] P. Zwart, A.G. Gerber, and T. Belamri. A two-phase flow model for predicting cavitation dynamics. *Fifth International Conference on Multiphase Flow*, 2004.

POLITECNICO
MILANO 1863

SCUOLA DI INGEGNERIA INDUSTRIALE
E DELL'INFORMAZIONE

Numerical Modelling of Cavitation Effects in Blood Flows

Tesi di Laurea Magistrale in
Aeronautical Engineering - Ingegneria Aeronautica

Author: **Matteo Zemello**

Student ID: 942003
Advisor: Prof. Luca Dedè
Co-advisors: Prof. Stefano Berrone, Dr. Ivan Fumagalli, Michele Bucelli
Academic Year: 2020-21

Abstract

This work aims at modelling cavitation phenomena occurring in blood flows. Cavitation is a phenomenon in which the static pressure of a liquid falls below the liquid's vapour pressure, leading to the formation of small vapor-filled cavities. Several *in vitro* and *in vivo* studies demonstrated that cavitation is likely to occur in blood flows in individuals with an implanted mechanical heart valve prosthesis, however numerical simulation of these phenomena is still limited. The main objective of the work is to provide an effective computational tool to numerically simulate and predict the occurrence of cavitation towards better designs and clinical implications. The Zwart-Gerber-Belamri model, an homogeneous Volume of Fluid mixture model, is selected to model cavitation. We provide and implement a proper discretization by means of the finite element method in a finite element library. Three different geometries are considered to test the model: simple geometries allow a direct comparison with literature results, whereas some insights are provided when complex geometries are considered to model the occurrence of cavitation across mechanical heart valves towards better designs. The cavitation model demonstrated capable of predicting cavitation in a wide range of geometries and conditions; numerical results confirmed that cavitation effects have to be considered to properly predict the flow features, especially the shear stresses across the valves, and their clinical consequences.

Keywords: Heart cavitation, Zwart cavitation model, VOF, MHVs

Abstract in lingua italiana

Questa tesi si pone come obiettivo modellare i fenomeni di cavitazione che si verificano nell'apparato cardiocircolatorio. La cavitazione è un fenomeno in cui la pressione di un liquido scende sotto la pressione di vapore del liquido stesso, portando alla formazione di piccole cavità di vapore. Diversi studi *in vitro* ed *in vivo* hanno dimostrato che fenomeni di cavitazione si verificano spesso nel flusso sanguineo di pazienti con protesi meccaniche di valvole cardiache, tuttavia la simulazione numerica di questo fenomeno è molto limitata. L'obiettivo principale di questa tesi è quindi quello di fornire uno strumento computazionale efficace per modellare e prevedere il verificarsi di fenomeni di cavitazione verso migliori design e implicazioni cliniche. Il modello di Zwart-Gerber-Belamri, un modello di miscela omogenea Volume of Fluid, è scelto per modellare la cavitazione. Viene discretizzato attraverso il metodo degli elementi finiti e implementato in una libreria ad elementi finiti. Tre diverse geometrie vengono considerate per testare il modello: le geometrie più semplici permettono un confronto diretto con i risultati presenti in letteratura, mentre geometrie più complesse portano a diverse considerazioni utili a migliorare il design delle valvole. Il modello di cavitazione si è dimostrato efficace nel predirre la cavitazione in un ampio spettro di geometrie e condizioni; i risultati numerici hanno confermato che gli effetti della cavitazione sono da tenere in considerazione per valutare correttamente le caratteristiche dei flussi sanguinei, specialmente gli shear stresses a cavallo delle valvole, e le loro conseguenze cliniche.

Parole chiave: Heart cavitation, Zwart cavitation model, VOF, MHVs

Contents

Introduction

Although the word *cavitation* was firstly coined by R.E. Froude and then cited by Barnaby and Thornycroft in 1895 [78], this phenomenon was discovered much earlier by L. Euler in his studies on water turbines in 1754 [17]. In the last century, cavitation phenomena have been observed and studied in a countless of engineering and research fields [8, 40, 81]. In this thesis work we focus on cavitation effects in biomedical applications, more precisely on numerical modelling of cavitation occurring in blood flows.

Cavitation in blood mainly occurs in the presence of implanted mechanical valves regulating the flow, when native valves are replaced by mechanical prostheses. The first phenomenological observations are dated back in the early 90s [41], when *in vitro* experiments on a mechanical heart valve (MHV) demonstrated the valve's tendency to cavitate. In more recent years, cavitation have been studied to engineer better valve designs and avoid several drawbacks associated with these phenomena [60]: cavitation, indeed, shortens the operating life of the prostheses due to the accelerated valves damage caused by the collapsing bubbles and the higher shear stresses deteriorate the blood tissue, making the use of anticoagulants compulsory [16].

In the literature different studies provide suggestions for improved designs that limit the occurrence of cavitation as, for example, through the use of softer materials [59]. However, the problem is still considered an open question and numerical studies on cavitation across mechanical valves are limited. For this reason, we propose a numerical model able to predict cavitation and model cavitation effects.

We carried out a literature research on cavitation phenomena and on the most common strategies employed to perform numerical simulations of cavitation. Cavitation in blood flows occurs mostly in the form of cloud cavitation [63], thus it is not advisable to track each liquid-vapor interface, instead a volume of fluid (VOF) method is preferable: in the whole domain the local vapor volume fraction is computed at each timestep and the fluid is considered as an homogeneous mixture of liquid and vapor phase. We adopted the Zwart-Gerber-Belamri cavitation model [85], since it demonstrated effective in modeling cavitation in Venturi-type geometries which resemble MHVs at the closing stage.

We developed the formulation of the model, coupling the mixture mass and momentum system with the equation describing the evolution of the vapor fraction. This resulted in a non zero velocity divergence when some evaporation or condensation process takes place, which provided a significant contribution in the energy estimate on the velocity.

We proposed a novel stabilized finite element formulation for the numerical modeling of cavitating flows. For spatial discretization we relied on piecewise linear Lagrangian polynomials; time discretization was performed by means of finite differences, in particular Backward Differentation Formulas (BDF) [62] of order one. The fluid flow and cavitation solvers have been implemented in `life`$^{\texttt{x}}$ [3], a C++ FE library under development at MOX laboratories at Politecnico di Milano, mainly focused on cardiac applications. The two solvers have been coupled in a staggered partitioned manner for versatility: at each timestep, the vapor fraction distribution is determined first, and then the homogeneous mixture equations are solved for pressure and mixture velocity.

We have tested the model on different geometries: the first benchmark provided an example of cavitation past bluff bodies and allowed a direct comparison with the literature [26]; we then studied a benchmark proposed by the Food and Drug Administration (FDA) to validate CFD codes for cardiovascular applications; finally a bileaflet valve geometry at the closing stage is considered. We show that the model is effective in predicting the occurrence of cavitation, providing consistent results with the literature. Moreover, we demonstrated the relevance of modelling cavitation to accurately predict the flow features such as the pressure distribution, the velocity divergence and the shear stresses, which are crucial to determine the deterioration effects of cavitation on the blood tissue [36]. In short, numerical results confirmed the efficacy of the proposed method which provided a tool that can be adopted in the MHVs engineering, towards improved designs and clinical applications.

The thesis is structured as follows: in Chapter 1 a literature review of cavitation phenomena in blood flows and a review of the cavitation modelling strategies are presented. In Chapter 2 the Zwart-Gerber-Belamri cavitation model in strong and weak formulation is described; the dimensionless groups governing the flow are derived and the cavitation number is defined. In Chapter 3 the problem is formulated by means of stabilized finite elements and the coupling of the staggered solvers is discussed, providing details on the solution algorithm. Chapters 4, 5 and 6 present the numerical results on different geometries. In Chapter 4 the results of the cylinder benchmark are analyzed and compared to the literature [26]. Chapter 5 is dedicated to the FDA nozzle benchmark. Chapter 6, presents the results on a 3D geometry resembling a bileaflet MHV. Finally, in Chapter 7 we summarize the main findings of the thesis, highlighting possible extensions.

1 | Cavitation phenomenon

Cavitation is a phenomenon in which the static pressure of a liquid reduces to below the liquid's vapour pressure, leading to the formation of small vapor-filled cavities. When pressure recovers to values higher than the vapor pressure, bubbles collapse, generating shock waves that can damage machinery.

This phenomenon is quite ubiquitous both in natural and industrial systems. One of the most famous examples of cavitation in nature are pistol shrimps which are able to generate a cavitating high speed water jet through a special shaped claw [39]; this ability is used for stunning and hunting preys and for communication purposes. Cavitation has also been studied in many engineering contexts, mainly the ones involving marine propellers [20], hydrofoils [40], machinery [8] and mechanical valves [81], where cavitation needs to be avoided to prevent damage caused by the bubbles collapse [56].

In more recent years researchers started to investigate possible applications of cavitation, understanding that bubble collapse could produce some advantages in many engineering fields. Examples include industrial mixing machines used to mix or break down suspended particles in a colloidal liquid compound, such as paint mixture or milk [13]; cavitation can play an important role in promoting the fuel and oxidizer mixing in fuel nozzles [6, 25]. Cavitation is exploited also in bioengineering applications, for instance in the destruction of kidney stones in shock wave lithotripsy [24], industrial cleaning applications [72] and for food and beverage applications, where it has been applied to egg pasteurization [4].

Despite having been studied in several fields of application, as depicted in the previous paragraphs, cavitation is still considered a complex phenomenon, difficult to understand and to predict through numerical modelling. The main purpose of the present work is to focus on a specific application investigating the effects of cavitation in blood flows, providing evidences of the need to consider this issue and proposing a numerical model able to predict the occurrence of cavitation.

1.1. Cavitation phenomena in blood flows

Cavitation in human blood circulation can seldom occur in physiological conditions: in an healthy patient in rest condition, blood cavitation does not take place, whereas it is very likely to occur for a patient who suffered from a heart valve disease and had the flawed valve replaced with an implanted mechanical prosthesis [5]. The first valve replacement on a human patient was performed in 1962 by surgeon Alfred Gunning from Oxford [50], and nowadays approximately 280.000 cardiac valve substitutes are implanted globally every year, half of which are mechanical valve prostheses (MVP) [82].

Starting from the early 90s, the issue of heart valve cavitation started receiving some careful attention by several researchers, because of the increasing number of mechanical valve installed. As first step these studies were mainly focused on *in vitro* phenomenon observations [41], then some *in vivo* measurements were taken, measuring the high frequency pressure fluctuations caused by cavitation bubble formation and collapse after valve closure, mainly focusing on mitral MVPs [83]. Through a high fidelity, piezoelectric pressure transducer the root mean square (RMS) value of the mitral pressure signal during a 5 ms interval after valve closure was calculated and used as a measure of cavitation intensity, finding good accordance with the *in vitro* set of measurements.

Right after the first experimental campaigns, researchers started wondering if the phenomenon observed across the valve had the same nature of the already known propellers cavitation or was due to other reasons. In 1999 Rambod et al. [63] provided a detailed physical description of the measured cavitation phenomena across heart MVPs. High intensity transient signals due to microbubbles and cloud cavitation have been recorded at the instant of closure of all the different mechanical heart valves (MHV) tested by his team. They postulated that, as in every phase transition process, cavitation is facilitated by a local structural inhomogeneity in the fluid, as for example pre-existing gaseous nuclei in the liquid. Then, two mechanisms appear to drive the growth of nuclei in the blood stream: diffusion, which mildly enlarges the nuclei, followed by sudden pressure drop, which initializes the rapid growth. The pressure drop is driven by the high trans-valvular velocity reached at the valve closure, inducing a local pressure approximately equal to the vapor pressure of water at the working temperature. These bubbles have a very short lifetime of approximately $8 - 10$ ms and can be effectively described by cloud cavitation. Some images taken from the original work of rambod et al. [63] are reported in Figure 1.1. They show the evolution of the cavitation clouds across a St. Jude Medical bileaflet mechanical valve at closure.

Rambod [63] also observed that a few bubbles had a longer lifetime ($1-2$ s). He postulated

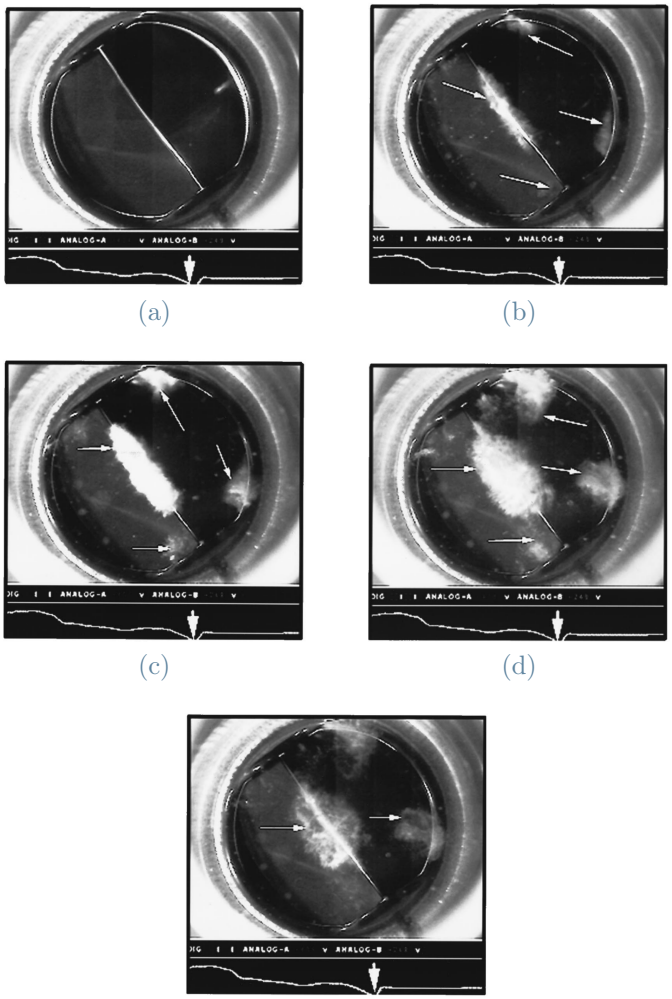

Figure 1.1: **The sequence of gas-filled microbubbles formation in a 29 mm mitral St. Jude Medical bileaflet mechanical valve at closure. (a)** End-diastolic period < 1 ms prior to complete closure, **(b)** the burst at the instant of closure and formation of clouds of microbubbles (t_0) **(c)** dissipation of clouds at about $t_0 + 5$ ms, **(d)** and **(e)** pressure recovery and growth of persisting gas-filled bubbles at approximately $t_0 + 8$ ms. Adapted from [63].

a physical explanation different from the cavitation cloud, due to the substantial difference in characteristic times: the bubbles with a longer lifetime are hypothesized to be filled with released gas due to the pressure drops. The longer bubble lifetime could be due to the time needed to reabsorb the released gas in blood. N_2 has proved to be the most likely gas [22] to be responsible for this phenomenon.

Starting from the Rambod's pioneering work, different researchers tried to understand the reason for cavitation across mechanical heart valves. A comprehensive review of the different studies is reported in [59].

There are different types of prosthetic heart valves, which can be categorized as mechanical valves or bioprosthetic valves, made from animal tissue. In this work, we mostly focus on MHVs because it has been proven that bioprostheses are not likely to cavitate just as a native heart valves [5]. However, mechanical heart valve have many advantages and their lower risk to benefit ratio has led the American and European guidelines on valvular heart disease to recommend the use of mechanical prostheses in patients younger than 60 years of age [29]. Their main advantage with respect to bioprosthetic valves is the extended lifetime. Indeed, valves made of animal tissue suffer of an accelerated structural valve deterioration, requiring reoperation after 20 years on average [79].

Mechanical valves are mainly divided in two types: monoleaflet and bileaflet; Figure 1.2 shows examples of popular valve designs. Different studies demonstrated that both the designs suffer from cavitation problems which is mainly due to the closing dynamic. In monoleaflet valves, high velocity squeeze flows and hammer phenomenon are generated when the leaflet hits the seat stop. This induces local pressure drops which lead to cavitation inception. Reducing the contact area and the closing velocity is beneficial in diminishing the cavitation effects [46], as well as more flexible leaflet tips [12]. In bileaflet valves, cavitation is mainly due to the high speed squeeze flows generated during the closure of the second leaflet [37] whereas large scale vortexes formed at the instance of closure play a minor role in cavitation inception [44]. *In vitro* studies on mechanical heart valves mounted in an electrohydraulic total artificial heart [43] demonstrated that cavitation bubble density is higher in monoleaflet valves designs. This effect was motivated with the higher closing velocity observed for the monoleaflet design with respect to bileaflet valves.

After observing the cavitation phenomenon across mechanical heart valves, scientists tried to understand the clinical implications of this phenomenon. The clinical relevance of cavitation is mostly related to cavitation clouds of small bubbles collapsing after a very short lifetime of few milliseconds. The first clinical implication of cavitation is in fact due to the collapse of the cavitation bubbles which can damage the mechanical heart valves structures and the blood cells. Scanning electron microscopy of explanted valves revealed confined areas of pitting and erosion on the leaflet and the housing after only 36 months of service [38]. At the same time bubble collapse damages blood cells, inducing the release of cell contents (fragments of monocytes and platelets) into the blood [36]. The release of tissue factor into the bloodstream is the primary initiator of blood coagulation and thrombus formation seen in patients with mechanical heart valve implants [66], making anticoagulation therapies compulsory for patients with an implanted MHV. Another important effect of cavitation is the formation of gaseous emboli. Potthast et al. [58] supported the

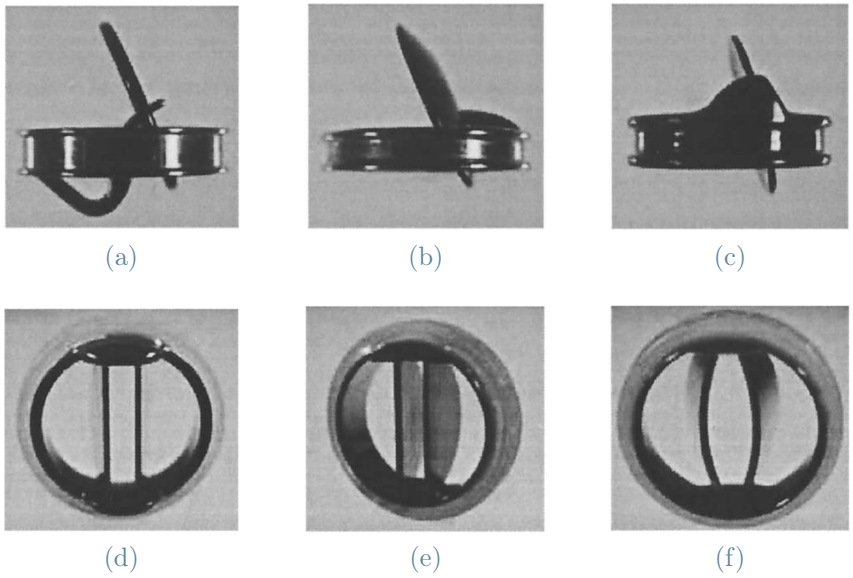

Figure 1.2: **Photographs of different MHVs. The upper row provides examples of monoleaflet valves, whereas in the lower row bileaflet valves are shown. (a)** Medtronic Hall valve, **(b)** Björk-Shiley valve, **(c)** Omnicarbon valve, **(d)** St. Jude valve, **(e)** ATS valve, **(f)** Sorin valve. Adapted from [42].

idea that cavitation is the key factor in the appearance of gaseous microemboli at heart valve prostheses which have been identified also in the cranial circulation of some mechanical heart valve patients through transcranial Doppler ultrasonography [53] representing a serious threat for atherosclerotic stenosis of intracranial arteries leading to strokes [21].

As demonstrated in the previous paragraphs, cavitation phenomena can take place across mechanical heart valves and a better understanding of these occurrences could have significant clinical implications. Numerical modelling of cavitation in blood flows would allow for improved mechanical valves designs reducing one of the main drawbacks of these kind of prostheses.

1.2. Modelling cavitation

Cavitation modeling involves the simulation of multiphase flows and poses great challenges, due to the need to track intefaces between the different fluid phases and the large and discontinuous properties variations across them. Two different models are commonly used for the simulations of multiphase and multicomponent flows.

The first set of models is a generalization of the two-fluid approach [64] where each phase or component is considered to fill a distinct volume and the interfaces between

the volumes are captured explicitly. Typical applications include front tracking methods for the prediction of the motion of large bubbles in a liquid [80] and the capture of any liquid-gas interface through phase-fields models [27]. In those kind of models, in order to capture the transfer of mass for cavitation, an equation of state to correlate density and speed of sound with pressure and temperature is required whereas no additional transport equations are used for the vapor phase, whose void fraction is determined by the mixture composition, known thanks to the interface tracking [47]. These methods have been tested only on simple cases and geometries because they require a great computational effort and are not able to effectively reproduce the small cavitation bubbles populating the bubble clouds observed in the *in vitro* experiments.

In the second approach, the phases or the different components are spatially averaged, and the fluid is considered as an homogeneous mixture. These methods are broadly categorized as Volume of Fluid (VOF) [30], the Level Set (LS) [70] and the Coupled Level Set-Volume of Fluid (CLSVOF) [77]. This class of methods assumes that the pure liquid and vapor phases are incompressible and the two-phase mixture density can be obtained as an interpolation based on a phase indicator coefficient, which is often written as the local phase fraction of either the liquid or the vapor phase. Hence, in addition to the Navier-Stokes system for the mixture there is a supplementary number of scalar transport equations, depending on the number of fluid interfaces to capture. To describe a single component cavitating flow, only one phase indicator is needed, representing e.g. the local vapor volume fraction. In this framework, different models differ in their definition of the rate of transfer of mass between different phases. Merkle et al. [49] used dimensional arguments for bubble clusters to obtain a source term depending on the local pressure and the liquid phase fraction. Later models by Schnerr-Sauer [68], Zwart et al. [85] and Singhal et al. [73] assumed the cavities to be present in the form of clusters of spherical bubbles. The volume fraction occupied by the vapor is considered as the sum of the small vapor bubbles whose evolution is described by a simplified form of the Rayleigh-Plesset equation [57] for spherical bubble dynamics. The source term is hence derived directly from the Rayleigh-Plesset equation. The models differ in the phenomenological arguments related to bubble-bubble interaction

VOF transport equation models have been applied to study several cavitating flow configurations over hydrofoils [34], nozzles [25] and are the current standard models used to study cavitation across industrial valves. We refer the interested reader to Quian et al. [59] for a review. Regarding the specific problem of mechanical heart valves, although a large number of researchers have done many studies on the flow characteristics and structural improvement of MHV, few consider cavitation effects and only rare examples are

found in the literature. In a very recent work, Gao et al. [45],[60] presented a transient computational model for computing the flow and cavitation characteristics of mechanical heart valves, analyzing the mechanism of cavitation using an VOF homogeneous mixture approach exploiting the Singhal [73] cavitation model, available in the commercial software Fluent 17.2 (ANSYS Inc., USA) [2].

The points described in the previous paragraphs led us to consider an homogeneous mixture model to include cavitation in the description of the fluid dynamics of blood flows. In the next chapters the Zwart-Gerber-Belamri model [85] and its coupling with the Navier-Stokes system is presented, as well as its numerical formulation and implementation within a Finite Element library.

2 | Mathematical modeling of cavitation

In this chapter the cavitation model selected for the implementation is developed and described. First of all, a proper phase indicator is defined; then the strong form of the governing equations is presented, motivating the need to couple the Navier-Stokes system for the homogeneous mixture with a transport equation for the vapor fraction phase indicator. After that, the Zwart cavitation model [85] is introduced, describing the dimensional arguments that led to the expressions of the condensation and vaporization terms. Finally, the dimensionless formulation of the coupled system is derived to highlight the dimensionless groups characterizing the flow. Such dimensionless groups will become relevant when validating our results against available literature data, in Chapter 4.

2.1. Governing equations

The strong form of the governing equations is presented before introducing the variational formulation. Let $\Omega \in \mathbb{R}^3$ be the physical domain and let $\Gamma = \partial\Omega$ be its boundary. We denote by $\mathbf{x} \in \Omega$ the spatial coordinates, and with $t \in (0, T]$ the temporal coordinate. At each point of the domain the fluid consists of two phases, namely the liquid phase and the vapor phase, and it is modeled as an homogeneous mixture. In the framework of the volume of fluid (VOF) methods [30], we define two phase indicators $\alpha_v(\mathbf{x}, t)$ and $\alpha_l(\mathbf{x}, t)$ to represent the volume phase fraction of the vapor and the liquid phase over the two-phase liquid-vapor mixture, respectively:

$$\alpha_v = \frac{V_v}{V_m}, \tag{2.1}$$

$$\alpha_l = \frac{V_l}{V_m}. \tag{2.2}$$

Since the sum of the volume occupied by vapor and liquid must be equal to the volume of the mixture, there holds:

$$\alpha_v + \alpha_l = 1. \tag{2.3}$$

Therefore, in a two phase mixture, only one independent phase indicator is needed to fully determine the properties of the mixture. In this work the vapor volume fraction is selected and will be denoted just as α:

$$\alpha_v = \alpha, \tag{2.4}$$

$$\alpha_l = 1 - \alpha. \tag{2.5}$$

Once the phase indicator is defined, the physical properties of the mixture are obtained as a combination of the properties of the liquid and vapor phases. The mixture density ρ_m and the fluid viscosity μ_m read as:

$$\rho_m = \alpha_v \rho_v + \alpha_l \rho_l = \alpha \rho_v + (1 - \alpha)\rho_l, \tag{2.6}$$

$$\mu_m = \alpha_v \mu_v + \alpha_l \mu_l = \alpha \mu_v + (1 - \alpha)\mu_l, \tag{2.7}$$

where ρ_v and ρ_l are the vapor and liquid density respectively which are though to be constant. The same notation holds for viscosity.

Once the phase indicators are defined, the governing equations can be written. The equations are derived imposing conservation of momentum and mass of the mixture, as well as conservation of mass for each phase. We recall the expression of the Navier-Stokes system for an homogeneous mixture:

$$\begin{cases} \dfrac{\partial \rho_m}{\partial t} + \nabla \cdot (\rho_m \mathbf{u}) = 0 & \text{in } \Omega \times (0,T], \quad (2.8a) \\ \dfrac{\partial (\rho_m \mathbf{u})}{\partial t} + \nabla \cdot (\rho_m \mathbf{u} \otimes \mathbf{u}) = -\nabla P + \nabla \cdot \tau & \text{in } \Omega \times (0,T], \quad (2.8b) \\ \mathbf{u} = \mathbf{g} & \text{on } \Gamma_D \times (0,T], \quad (2.8c) \\ (-P\mathbf{I} + \tau) \cdot \hat{\mathbf{n}} = \mathbf{h} & \text{on } \Gamma_N \times (0,T], \quad (2.8d) \\ \mathbf{u} = \mathbf{u}_0 & \text{in } \Omega \times \{0\}. \quad (2.8e) \end{cases}$$

where $\mathbf{u}(\mathbf{x},t) \in \mathbb{R}^3$ is the mixture velocity, $P(\mathbf{x},t) \in \mathbb{R}$ is the pressure, $\tau(\mathbf{x},t) \in \mathbb{R}^3 \times \mathbb{R}^3$ is the deviatoric stress tensor, Γ_D and Γ_N are the Dirichlet and Neumann boundaries, respectively.

In the next sections the strong form of the equation describing the evolution of the vapor fraction and the Navier-Stokes system for the mixture are formulated.

2.1.1. Vapor fraction transport equation

We prescribe the mass conservation for each of the individual mixture species, i.e. vapor and liquid phases. The conditions take the form [85]:

$$\begin{cases} \dfrac{\partial \rho_v \alpha}{\partial t} + \nabla \cdot (\rho_v \alpha \mathbf{u}) = \dot{S}_{\alpha_v} & \text{in } \Omega \times (0,T], \quad (2.9a) \\ \dfrac{\partial \rho_l (1-\alpha)}{\partial t} + \nabla \cdot (\rho_l (1-\alpha) \mathbf{u}) = \dot{S}_{\alpha_l} & \text{in } \Omega \times (0,T]. \quad (2.9b) \end{cases}$$

Equations (2.9a) and (2.9b) represent the conservation of mass for the sole vapor and liquid transition respectively; $\dot{S}_{\alpha_v}$ and $\dot{S}_{\alpha_l}$ are the mass transfer terms representing the phase transition from liquid to vapor or vice versa. (2.9a) and (2.9b) are not independent since only two phases are considered and the mass transfer terms are related: $\dot{S}_{\alpha_v} = -\dot{S}_{\alpha_l}$. This holds because the sum of the mass conservation equations of the sole vapor and liquid phase is the mass conservation of the mixture which is granted by the continuity equation for the mixture (2.8a). For this reason equation (2.9b) is not considered in the following model and the Navier-Stokes system written for the mixture is coupled with only one additional equation which is the mass conservation of the vapor fraction. In the following the notation will be simplified and $\dot{S}_{\alpha_v}$ will be addressed just as $\dot{S}_\alpha$.

Dividing equation (2.9a) by ρ_v, the final form of the transport equation of the phase indicator α is obtained:

$$\frac{\partial \alpha}{\partial t} + \nabla \cdot (\alpha \mathbf{u}) = \frac{\dot{S}_\alpha(\alpha, P)}{\rho_v} \qquad \text{in } \Omega \times (0,T]. \quad (2.10)$$

The right-hand side of the transport equation, $\dot{S}_\alpha(\alpha, P)$, is the term regulating the mass transfer between the liquid and the vapor phase and depends on the specific cavitation model. The derivation and the expression for $\dot{S}_\alpha(\alpha, P)$ is presented in section 2.1.4.

In the following, equation (2.10) is modified introducing a diffusive term $\kappa\Delta\alpha$ in order to regularize the interfaces between fluid volumes with null and finite value of alpha and facilitate the numerical solution of the vapor fraction equation. The influence of the diffusion coefficient κ is evaluated when the numerical results of the benchmarks are presented in Chapter 4 and 5; this is done to avoid introducing an artificial bias in the solution. The equation for α, hence reads:

$$\frac{\partial \alpha}{\partial t} + \nabla \cdot (\alpha \mathbf{u}) + \kappa \Delta \alpha = \frac{\dot{S}_\alpha(\alpha, P)}{\rho_v} \qquad \text{in } \Omega \times (0,T]. \quad (2.11)$$

2.1.2. Mixture mass conservation

The mass conservation of the mixture (2.8a), reads:

$$\frac{\partial \rho_m}{\partial t} + \nabla \cdot (\rho_m \mathbf{u}) = 0 \qquad \text{in } \Omega \times (0, T]. \tag{2.12}$$

During cavitation and condensation, the mixture flow is affected by strong variations of density; therefore to foster the stability of the solver the continuity equation is first written using its non-conservative formulation as suggested in [75]:

$$\frac{\partial \rho_m}{\partial t} + \rho_m \nabla \cdot \mathbf{u} + \mathbf{u} \cdot \nabla \rho_m = 0 \qquad \text{in } \Omega \times (0, T]. \tag{2.13}$$

Equation (2.13) is then rewritten to obtain a leaner formulation: taking the material derivative of equation (2.6) one can write:

$$\frac{\partial \rho_m}{\partial t} + \mathbf{u} \cdot \nabla \rho_m = (\rho_v - \rho_l)\Big(\frac{\partial \alpha}{\partial t} + \mathbf{u} \cdot \nabla \alpha\Big). \tag{2.14}$$

Substituting in equation (2.14) the identities (2.10) and (2.13), one obtains:

$$-\rho_m (\nabla \cdot \mathbf{u}) = (\rho_v - \rho_l)\Big(\frac{\dot{S}_\alpha}{\rho_v} - \alpha(\nabla \cdot \mathbf{u})\Big); \tag{2.15}$$

re-arranging terms:

$$(\rho_v \alpha + \rho_l(1-\alpha))(\nabla \cdot \mathbf{u}) = (\rho_l - \rho_v)\Big(\frac{\dot{S}_\alpha}{\rho_v} - \alpha(\nabla \cdot \mathbf{u})\Big); \tag{2.16}$$

collecting $\nabla \cdot \mathbf{u}$, the final form of the continuity equation for the mixture is obtained:

$$\nabla \cdot \mathbf{u} = \frac{\rho_l - \rho_v}{\rho_v \rho_l} \dot{S}_\alpha = \Big(\frac{1}{\rho_v} - \frac{1}{\rho_l}\Big)\dot{S}_\alpha. \tag{2.17}$$

Therefore, we consider the following form for the continuity equation of the mixture:

$$\nabla \cdot \mathbf{u} = \Big(\frac{1}{\rho_v} - \frac{1}{\rho_l}\Big)\dot{S}_\alpha \qquad \text{in } \Omega \times (0, T]. \tag{2.18}$$

We remark that the divergence of the mixture velocity is no longer zero, as for incompressible flows, because local dilation and compression effects are introduced by the finite mass transfer rate. The incompressibility constraint for each isolated phase is still valid,

indeed if no mass exchange between liquid and vapor happens, $\dot{S}_\alpha = 0$, and equation (2.18) reduces to $\nabla \cdot \mathbf{u} = 0$.

2.1.3. Mixture momentum conservation

The momentum conservation of the mixture (2.8b), reads:

$$\frac{\partial(\rho_m \mathbf{u})}{\partial t} + \nabla \cdot (\rho_m \mathbf{u} \otimes \mathbf{u}) = -\nabla P + \nabla \cdot \tau \qquad \text{in } \Omega \times (0, T]. \tag{2.19}$$

We assume the fluid to be Newtonian, so that τ can be written as a function of the flow velocity $\mathbf{u}$ and first and second viscosities μ_m and λ_m:

$$\tau = \mu_m[(\nabla \otimes \mathbf{u}) + (\nabla \otimes \mathbf{u})^T] + \lambda_m(\nabla \cdot \mathbf{u}) = 2\mu_m \nabla^S(\mathbf{u}) + \lambda_m(\nabla \cdot \mathbf{u}), \tag{2.20}$$

where the symmetric gradient-gradient formulation has been introduced:

$$\nabla^S(\mathbf{u}) = \frac{1}{2}[(\nabla \otimes \mathbf{u}) + (\nabla \otimes \mathbf{u})^T]. \tag{2.21}$$

For simplicity, we will assume $\lambda_m = 0$ so that

$$\tau = 2\mu_m \nabla^S(\mathbf{u}). \tag{2.22}$$

The left-hand side of the equation (2.19) can be rewritten in non-conservative form, expanding the transport term and subtracting the continuity equation of the mixture (2.8a) multiplied by the flow velocity $\mathbf{u}$. With the Einstein notation, there holds:

$$\big(\nabla \cdot (\rho_m \mathbf{u} \otimes \mathbf{u})\big)_i = \partial_j \rho_m u_i u_j = u_i \partial_j(\rho_m u_j) + \rho_m u_j \partial_j u_i = \big(\mathbf{u}\nabla \cdot (\rho_m \mathbf{u})\big)_i + \big(\rho_m \mathbf{u} \cdot \nabla \mathbf{u}\big)_i, \tag{2.23}$$

thus, it follows:

$$\begin{aligned} \frac{\partial(\rho_m \mathbf{u})}{\partial t} + \nabla \cdot (\rho_m \mathbf{u} \otimes \mathbf{u}) = \\ = \rho_m \frac{\partial \mathbf{u}}{\partial t} + \cancel{\left[\mathbf{u}\frac{\partial \rho_m}{\partial t} + \mathbf{u}\nabla \cdot (\rho_m \mathbf{u})\right]} + \rho_m \mathbf{u} \cdot \nabla \mathbf{u} = \\ = \rho_m \frac{\partial \mathbf{u}}{\partial t} + \rho_m \mathbf{u} \cdot \nabla \mathbf{u}. \end{aligned} \tag{2.24}$$

The final strong formulation of the momentum equation is:

$$\rho_m \frac{\partial \mathbf{u}}{\partial t} + \rho_m \mathbf{u} \cdot \nabla \mathbf{u} + \nabla P - \nabla \cdot \big(2\mu_m \nabla^S(\mathbf{u})\big) = 0 \qquad \text{in } \Omega \times (0, T]. \tag{2.25}$$

2.1.4. Zwart cavitation model

In section 2.1.1, the expression of the generic transport equation for the vapor volume fraction (2.11) has been derived. In this section the expression of the liquid-vapor mass transfer $\dot{S}_\alpha$ is presented following, the model proposed by Zwart et al. [85].

Like in other cavitation models [68, 73], the expression of $\dot{S}_\alpha$ is derived from the Rayleigh-Plesset equation which describes the growth of a vapor bubble in a liquid [57]:

$$R_B \frac{d^2 R_B}{dt^2} + \frac{3}{2}(\frac{dR_B}{dt})^2 + \frac{2\sigma}{R_B} = \frac{P - P_v}{\rho_l}, \tag{2.26}$$

wherein R_B represents the bubble radius, σ represents the surface tension coefficient, and P_v represents the vapor pressure.

Following [68] and [73], Zwart neglected the second order terms and the surface tension obtaining a simplified expression for the evolution of the bubble radius R_B:

$$\frac{dR_B}{dt} = \sqrt{\frac{2}{3}\frac{P_v - P}{\rho_l}}. \tag{2.27}$$

Equation (2.27) is called the Rayleigh relation and it is considered an adequate description for the so-called inertia controlled bubble growth if the system pressure is sufficiently low and the pressure difference $P_v - P$ is large [68].

The volume of a single bubble is $V_B = \frac{4}{3}\pi R_B^3$, hence the rate of change of mass of a single bubble can be computed as:

$$\frac{dm_B}{dt} = 4\pi R_B^2 \rho_v \sqrt{\frac{2}{3}\frac{P_v - P}{\rho_l}}. \tag{2.28}$$

If there are N_B bubbles per unit volume, and they are assumed to have the same radius R_B, then it is possible to express the vapor volume fraction as:

$$\alpha = V_B N_B = \frac{4}{3}\pi R_B^3 N_B. \tag{2.29}$$

The total interphase mass transfer rate is hence obtained as:

$$\dot{S}_\alpha = N_B \frac{dm_B}{dt} = \frac{3\alpha\rho_v}{R_B}\sqrt{\frac{2}{3}\frac{P_v - P}{\rho_l}}. \tag{2.30}$$

The definition of $\dot{S}_\alpha$ provided in (2.30) has been derived assuming that bubbles only grow, i.e. that mass is only transferred from the liquid to the vapor phase (vaporization). It can be generalized to include condensation:

$$\dot{S}_\alpha = F\frac{3\alpha\rho_v}{R_B}\sqrt{\frac{2}{3}\frac{|P_v - P|}{\rho_l}}\,\text{sign}(P_v - P), \tag{2.31}$$

introducing an empirical calibration coefficient F.

Zwart [85] argued that (2.31) represents well condensation, whereas it is not physically correct in modeling vaporization because it has been obtained assuming that no bubble-bubble interaction takes place. This is true only for the early stages of cavitation, whereas when the vapor fraction increases, the generation of new bubbles must decrease accordingly. To account for this, (2.31) is modified introducing the nucleation site volume fraction r_{nuc}, and replacing α with $r_{nuc}(1-\alpha)$ during vaporization, so that vaporization decreases as alpha increases.

The final form of mass transfer terms of the cavitation model is the following:

$$\dot{S}_\alpha(\alpha, P) = \underbrace{F_{vap}\frac{3r_{nuc}(1-\alpha)\rho_v}{R_B}\sqrt{\frac{2}{3}\frac{\max(P_v - P, 0)}{\rho_l}}}_{\text{(vaporization)}} - \underbrace{F_{cond}\frac{3\alpha\rho_v}{R_B}\sqrt{\frac{2}{3}\frac{\max(P - P_v, 0)}{\rho_l}}}_{\text{(condensation)}}. \tag{2.32}$$

In (2.32), the first part of the right-hand side represents the vaporization term, which is active only when the local pressure is lower than the mixture vapor pressure, whereas the second part is the condensation term.

Substituting (2.32) in (2.10), the Zwart vapor fraction transport equation is obtained:

$$\frac{\partial\alpha}{\partial t} + \nabla\cdot(\alpha\mathbf{u}) + \kappa\Delta\alpha = F_{vap}\frac{3r_{nuc}(1-\alpha)}{R_B}\sqrt{\frac{2}{3}\frac{\max(P_v - P, 0)}{\rho_l}} - F_{cond}\frac{3\alpha}{R_B}\sqrt{\frac{2}{3}\frac{\max(P - P_v, 0)}{\rho_l}}. \tag{2.33}$$

Zwart [85] provided values for the model parameters, calibrated to match experimental data for a variety of fluids and devices. Their meaning, value and unit of measure are summarized in Table 2.1.

Evaporation coefficient	$F_{vap} = 50$	[-]
Condensation coefficient	$F_{cond} = 0.01$	[-]
Nucleation volume fraction	$r_{nuc} = 10^{-4}$	[-]
Nucleation site radius	$R_B = 10^{-6}$	[m]

Table 2.1: **Original Zwart model constants.**

2.2. Dimensionless formulation

In this section the dimensionless formulations of the mass and momentum conservation for the flow mixture and the transport equation for the vapor fraction are obtained. This is done to identify the proper dimensionless groups and scaling factors that can be used to compare numerical results with data from the literature. In addition to the Strouhal number $\mathbb{S}t$, Euler number $\mathbb{E}u$ and Reynolds number $\mathbb{R}e$, we introduce the definition of the cavitation number σ, the liquid-vapor density and viscosity ratios R_ρ and R_μ and $\mathbb{R}e_\kappa$, the dimensionless group associated with the diffusion parameter κ.

We introduce the dimensionless variables ($\bar{\rho}$, $\bar{\mu}$ $\bar{\mathbf{u}}$, $\bar{\mathbf{x}}$, $\bar{t}$, $\bar{P}$, $\bar{\kappa}$, $\Delta\bar{P}$) through suitable scaling factors, as follows:

$$\rho = \rho_0\bar{\rho} = \rho_0\bar{\rho}_l[\alpha\frac{\rho_v}{\rho_l} + (1-\alpha)], \tag{2.34}$$

$$\mu = \mu_0\bar{\mu} = \mu_0\bar{\mu}_l[\alpha\frac{\mu_v}{\mu_l} + (1-\alpha)], \tag{2.35}$$

$$\mathbf{u} = u_0\bar{\mathbf{u}}, \tag{2.36}$$

$$\mathbf{x} = L_0\bar{\mathbf{x}}, \tag{2.37}$$

$$t = t_0\bar{t}, \tag{2.38}$$

$$P = P_0\bar{P}, \tag{2.39}$$

$$\kappa = \kappa_0\bar{\kappa}, \tag{2.40}$$

$$P - P_v = (P_0 - P_v)\Delta\bar{P} = \Delta P_0\Delta\bar{P}. \tag{2.41}$$

The other constant dimensional parameters, as the vapor density ρ_v, the liquid density ρ_l, the vapor viscosity μ_v, the liquid viscosity μ_l and R_B are scaled consistently with the corresponding variables in (2.34)-(2.41).

2.2.1. Vapor fraction transport equation

Starting from the strong form of the vapor fraction transport equation (2.33), and substituting the adimensionalizations (2.34)-(2.41), we obtain:

$$\begin{aligned}\frac{1}{t_0}\Big(\frac{\partial\alpha}{\partial\bar{t}}\Big)+\frac{u_0}{L_0}\Big(\bar{\nabla}\cdot(\alpha\mathbf{u})\Big)+\frac{\kappa_0}{L_0^2}\Big(\bar{\kappa}\bar{\nabla}^2\alpha\Big)=\\ \frac{\sqrt{\Delta P_0}}{L_0\sqrt{\rho_0}}\Big(F_{vap}\frac{3r_{nuc}(1-\alpha)}{\bar{R}_B}\sqrt{\frac{2}{3}\frac{\max(-\Delta\bar{P},0)}{\bar{\rho}_l}}-F_{cond}\frac{3\alpha}{\bar{R}_B}\sqrt{\frac{2}{3}\frac{\max(\Delta\bar{P},0)}{\bar{\rho}_l}}\Big),\end{aligned}\tag{2.42}$$

$$\begin{aligned}\frac{L_0}{u_0t_0}\Big(\frac{\partial\alpha}{\partial\bar{t}}\Big)+\Big(\bar{\nabla}\cdot(\alpha\mathbf{u})\Big)+\frac{\kappa_0}{u_0L_0}\Big(\bar{\kappa}\bar{\nabla}^2\alpha\Big)=\\ \sqrt{\frac{\Delta P_0}{\rho_0u_0}}\Big(F_{vap}\frac{3r_{nuc}(1-\alpha)}{\bar{R}_B}\sqrt{\frac{2}{3}\frac{\max(-\Delta\bar{P},0)}{\bar{\rho}_l}}-F_{cond}\frac{3\alpha}{\bar{R}_B}\sqrt{\frac{2}{3}\frac{\max(\Delta\bar{P},0)}{\bar{\rho}_l}}\Big).\end{aligned}\tag{2.43}$$

From the above, we introduce the definition of the Strouhal number $\mathbb{S}t$:

$$\mathbb{S}t=\frac{L_0}{u_0t_0},\tag{2.44}$$

the adimensional group associated with the diffusion $\mathbb{R}e_\kappa$:

$$\mathbb{R}e_\kappa=\frac{u_0L_0}{\kappa_0},\tag{2.45}$$

and the cavitation number σ:

$$\sigma=\frac{P_0-P_v}{\frac{1}{2}\rho_0u_0^2}.\tag{2.46}$$

Substituting the definition of the adimensional groups defined previously, we obtain the non-dimensional transport equation for α:

$$\begin{aligned}\mathbb{S}t\Big(\frac{\partial\alpha}{\partial\bar{t}}\Big)+\Big(\bar{\nabla}\cdot(\alpha\mathbf{u})\Big)+\frac{1}{\mathbb{R}e_\kappa}\Big(\bar{\kappa}\bar{\nabla}^2\alpha\Big)=\\ \sqrt{\frac{\sigma}{2}}\Big(F_{vap}\frac{3r_{nuc}(1-\alpha)}{\bar{R}_B}\sqrt{\frac{2}{3}\frac{\max(-\Delta\bar{P},0)}{\bar{\rho}_l}}-F_{cond}\frac{3\alpha}{\bar{R}_B}\sqrt{\frac{2}{3}\frac{\max(\Delta\bar{P},0)}{\bar{\rho}_l}}\Big).\end{aligned}\tag{2.47}$$

2.2.2. Mass conservation

We rewrite the continuity equation (2.33) using the adimensionalizations (2.34)-(2.41):

$$\frac{u_0}{L_0}\Big(\bar{\nabla}\cdot\bar{\mathbf{u}}\Big)=\frac{\rho_0\sqrt{\Delta P_0}}{L_0\rho_0\sqrt{\rho_0}}\Big((\frac{1}{\frac{\rho_v}{\rho_l}\bar{\rho}_l}-\frac{1}{\bar{\rho}_l})F_{vap}\frac{3r_{nuc}(1-\alpha)(\frac{\rho_v}{\rho_l}\bar{\rho}_l)}{\bar{R}_B}\sqrt{\frac{2}{3}\frac{\max(-\Delta\bar{P},0)}{\bar{\rho}_l}}+ \\ -F_{cond}\frac{3\alpha(\frac{\rho_v}{\rho_l}\bar{\rho}_l)}{\bar{R}_B}\sqrt{\frac{2}{3}\frac{\max(\Delta\bar{P},0)}{\bar{\rho}_l}}\Big), \tag{2.48}$$

$$\Big(\bar{\nabla}\cdot\bar{\mathbf{u}}\Big)=\sqrt{\frac{\Delta P_0}{\rho_0 u_0^2}}\Big((\frac{1}{\frac{\rho_v}{\rho_l}\bar{\rho}_l}-\frac{1}{\bar{\rho}_l})F_{vap}\frac{3r_{nuc}(1-\alpha)(\frac{\rho_v}{\rho_l}\bar{\rho}_l)}{\bar{R}_B}\sqrt{\frac{2}{3}\frac{\max(-\Delta\bar{P},0)}{\bar{\rho}_l}}+ \\ -F_{cond}\frac{3\alpha(\frac{\rho_v}{\rho_l}\bar{\rho}_l)}{\bar{R}_B}\sqrt{\frac{2}{3}\frac{\max(\Delta\bar{P},0)}{\bar{\rho}_l}}\Big). \tag{2.49}$$

We define the liquid-vapour density ratio R_ρ as:

$$R_\rho=\frac{\rho_v}{\rho_l} \tag{2.50}$$

Substituting the definition of the cavitation number and of the density ratio in (2.49), the non-dimensional mass conservation for the mixture is obtained:

$$\Big(\bar{\nabla}\cdot\bar{\mathbf{u}}\Big)=\sqrt{\frac{\sigma}{2}}\Big((\frac{1}{R_\rho\bar{\rho}_l}-\frac{1}{\bar{\rho}_l})F_{vap}\frac{3r_{nuc}(1-\alpha)(R_\rho\bar{\rho}_l)}{\bar{R}_B}\sqrt{\frac{2}{3}\frac{\max(-\Delta\bar{P},0)}{\bar{\rho}_l}}+ \\ -F_{cond}\frac{3\alpha(R_\rho\bar{\rho}_l)}{\bar{R}_B}\sqrt{\frac{2}{3}\frac{\max(\Delta\bar{P},0)}{\bar{\rho}_l}}\Big). \tag{2.51}$$

2.2.3. Momentum conservation

Replacing the definitions of the non-dimensional variables in the strong form of the momentum conservation for the mixture (2.25) the following holds:

$$\frac{\rho_0 u_0}{t_0}\Big(\bar{\rho}\frac{\partial\bar{\mathbf{u}}}{\partial\bar{t}}\Big)+\frac{\rho_0 u_0^2}{L_0}\Big(\bar{\rho}\bar{\mathbf{u}}\cdot\bar{\nabla}\bar{\mathbf{u}}\Big)+\frac{P_0}{L_0}\Big(\bar{\nabla}\bar{P}\Big)-\frac{\mu_0 u_0}{L_0^2}\Big(\bar{\nabla}\cdot\big(2\bar{\mu}\bar{\nabla}^S(\bar{\mathbf{u}})\big)\Big)=0, \tag{2.52}$$

$$\frac{L_0}{u_0 t_0}\Big(\bar{\rho}\frac{\partial\bar{\mathbf{u}}}{\partial\bar{t}}\Big)+\Big(\bar{\rho}\bar{\mathbf{u}}\cdot\bar{\nabla}\bar{\mathbf{u}}\Big)+\frac{P_0}{\rho_0 u_0^2}\Big(\bar{\nabla}\bar{P}\Big)-\frac{\mu_0}{\rho_0 u_0 L_0}\Big(\bar{\nabla}\cdot\big(2\bar{\mu}\bar{\nabla}^S(\bar{\mathbf{u}})\big)\Big)=0. \tag{2.53}$$

It is possible to recognise and define the the Euler number $\mathbb{E}u$:

$$\mathbb{E}u = \frac{P_0}{\rho_0 u_0^2}, \tag{2.54}$$

and the liquid-vapour viscosity ratio:

$$R_\mu = \frac{\mu_v}{\mu_l} \tag{2.55}$$

Substituting the definitions introduced above in (2.53) and making explicit the dependence of the non dimensional density and viscosity on the respective ratios, the final form of the non-dimensional momentum equation reads:

$$\mathbb{S}t\Big(\bar{\rho}(R_\rho)\frac{\partial \bar{\mathbf{u}}}{\partial \bar{t}}\Big) + \Big(\bar{\rho}(R_\rho)\bar{\mathbf{u}}\cdot\bar{\nabla}\bar{\mathbf{u}}\Big) + \mathbb{E}u\Big(\bar{\nabla}\bar{P}\Big) - \frac{1}{\mathbb{R}e}\Big(\bar{\nabla}\cdot\big(2\bar{\mu}(R_\mu)\bar{\nabla}^S(\bar{\mathbf{u}})\Big) = 0. \tag{2.56}$$

2.3. Cavitation model in strong formulation

Coupling the mass conservation (2.18) and the momentum conservation (2.25) for the mixture, with the equation describing the evolution of the vapor fraction (2.33), we state the cavitation model in strong formulation.

Let us assume that Γ is subdivided in a subset Γ_D, where Dirichlet conditions are prescribed, and a subset Γ_N, where Neumann conditions are set, such that $\Gamma = \Gamma_D \cup \Gamma_N$. In a time interval $(0, T]$ with $T > 0$, the problem reads:

$$\begin{cases} \rho\dfrac{\partial \mathbf{u}}{\partial t} + \rho\mathbf{u}\cdot\nabla\mathbf{u} + \nabla P - \nabla\cdot\big(2\mu\nabla^S(\mathbf{u})\big) = 0 & \text{in } \Omega\times(0,T], \\ \nabla\cdot\mathbf{u} - \Big(\dfrac{1}{\rho_v} - \dfrac{1}{\rho_l}\Big)\dot{S}_\alpha = 0 & \text{in } \Omega\times(0,T], \\ \dfrac{\partial \alpha}{\partial t} + \nabla\cdot(\alpha\mathbf{u}) - \kappa\Delta\alpha - \dfrac{\dot{S}_\alpha(\alpha,P)}{\rho_v} = 0 & \text{in } \Omega\times(0,T], \\ \mathbf{u} = \mathbf{g}, \quad \alpha = \gamma & \text{on } \Gamma_D\times(0,T], \\ (-P\mathbf{I} + 2\mu\nabla^S(\mathbf{u}))\cdot\hat{\mathbf{n}} = \mathbf{h} & \text{on } \Gamma_N\times(0,T], \\ (\alpha\mathbf{u} - \kappa\nabla\alpha)\cdot\hat{\mathbf{n}} = \eta & \text{on } \Gamma_N\times(0,T], \\ \mathbf{u} = \mathbf{u}_0, \quad \alpha = \alpha_0 & \text{in } \Omega\times\{0\}. \end{cases} \tag{2.57}$$

The coupled problem reported in (2.57) is written using the conservative formulation of the equation for α, since the transport term is written as $\nabla\cdot(\alpha\mathbf{u})$. Another possibility is considering the non-conservative formulation where $\nabla\cdot(\alpha\mathbf{u}) = \alpha\nabla\cdot\mathbf{u} + \nabla\alpha\cdot\mathbf{u}$. This

reduces in a different expression for the boundary condition Γ_N:

$$\begin{cases} \dfrac{\partial \alpha}{\partial t} + \alpha \nabla \cdot \mathbf{u} + \nabla \alpha \cdot \mathbf{u} - \kappa \Delta \alpha - \dfrac{\dot{S}_\alpha(\alpha, P)}{\rho_v} = 0 & \text{in } \Omega \times (0,T], \\ \alpha = \gamma & \text{on } \Gamma_D \times (0,T], \\ (-\kappa \nabla \alpha) \cdot \hat{\mathbf{n}} = \eta & \text{on } \Gamma_N \times (0,T], \\ \alpha = \alpha_0 & \text{in } \Omega \times \{0\}. \end{cases} \tag{2.58}$$

Both the conservative and non-conservative numerical formulation have been developed, implemented and used to produce numerical results. However, in the following sections of this document, only the conservative formulation is reported. When needed, the non-conservative formulation is recalled and the differences with the conservative formulation are highlighted.

2.4. Cavitation model in weak formulation

Let us introduce the following spaces:

$$\begin{aligned} V_g &:= \{\mathbf{u} \in [H^1(\Omega)]^d : \mathbf{u}|_{\Gamma_D} = \mathbf{g}\}, \\ V_0 &:= \{\mathbf{u} \in [H^1(\Omega)]^d : \mathbf{u}|_{\Gamma_D} = 0\}, \\ Q &:= L^2(\Omega), \\ \mathcal{V}_g &:= V_g \times Q, \\ \mathcal{V}_0 &:= V_0 \times Q. \end{aligned}$$

The system of conservation of mixture mass and momentum in weak formulation reads:

for all $t \in (0,T]$, find $\mathbf{U}(t) = \{\mathbf{u}, P\} \in \mathcal{V}_g$ with $\mathbf{u}(0) = \mathbf{u}_0$:

$$A(\mathbf{U}, \mathbf{W}) = A_1(\mathbf{U}, \mathbf{W}) + A_2(\mathbf{U}, \mathbf{U}, \mathbf{W}) = L(\mathbf{W}), \tag{2.59}$$

for all $\mathbf{W} = \{\mathbf{v}, q\} \in \mathcal{V}_0$ with:

$$\begin{aligned} A_1(\mathbf{U}, \mathbf{W}) = \Big(\rho(\alpha)\frac{\partial \mathbf{u}}{\partial t}, \mathbf{v}\Big) + \big(2\mu(\alpha)\nabla^S \mathbf{u}, \nabla \mathbf{v}\big) - \big(P, \nabla \cdot \mathbf{v}\big) + \\ + \big(\nabla \cdot \mathbf{u}, q\big) - \Big(\big(\frac{1}{\rho_v} - \frac{1}{\rho_l}\big)\dot{S}_\alpha(\rho, P), q\Big), \end{aligned} \tag{2.60}$$

$$A_2(\mathbf{U}, \mathbf{U}, \mathbf{W}) = (\rho(\alpha)\mathbf{u} \cdot \nabla \mathbf{u}, \mathbf{v}), \tag{2.61}$$

$$L(\mathbf{V}) = (\mathbf{h}, \mathbf{v})_{\Gamma_N}, \tag{2.62}$$

where $(\cdot,\cdot)$ denotes the L^2 inner product over Ω and $(\cdot,\cdot)_{\Gamma_N}$ the inner product over Γ_N.

A similar procedure is followed for the transport equation of the vapor fraction α; let us define the spaces:

$$\Phi_\gamma := \{\alpha \in [H^1(\Omega)]^d : \alpha|_{\Gamma_D} = \gamma\},$$
$$\Phi_0 := \{\alpha \in [H^1(\Omega)]^d : \alpha|_{\Gamma_D} = 0\}.$$

The α transport equation in weak formulation reads:

for all $t \in (0, T]$, find $\phi \in \Phi_\gamma$ with $\alpha(0) = \alpha_0$:

$$a(\alpha, \phi) = l(\phi), \tag{2.63}$$

for all $\phi \in \Phi_0$ with:

$$a(\alpha, \phi) = \Big(\frac{\partial \alpha}{\partial t}, \phi\Big) - \big(\alpha \mathbf{u}, \nabla\phi\big) + \big(\kappa\nabla\alpha, \nabla\phi\big) - \Big(\frac{\dot{S}_\alpha(\alpha, P)}{\rho_v}, \phi\Big), \tag{2.64}$$

$$l(\phi) = (\eta, \phi)_{\Gamma_N}. \tag{2.65}$$

Equation (2.59) and (2.64) represent the weak formulation of the coupled problem, let us remark that (2.59) and (2.64) are coupled, since the mixture density and viscosity depend on α and the velocity divergence depends on the liquid-vapor mass transfer rate $\dot{S}_\alpha(\alpha, P)$.

In the non-conservative formulation, instead, the following holds:

$$a(\alpha, \phi) = \Big(\frac{\partial \alpha}{\partial t}, \phi\Big) + \big(\alpha\nabla \cdot \mathbf{u} + \nabla\alpha \cdot \mathbf{u}, \phi\big) + \big(\kappa\nabla\alpha, \nabla\phi\big) - \Big(\frac{\dot{S}_\alpha(\alpha, P)}{\rho_v}, \phi\Big). \tag{2.66}$$

In the Chapter 3 the spatial and temporal discretization are presented for both problems (2.59) and (2.64) as well as the coupling strategy.

3 | Numerical model

In this chapter the numerical model for cavitation is presented. First the space discretization of both (2.59) and (2.64) is developed introducing additional terms responsible for the stabilization in (3.29) and (3.23). Then a full time-space discretization is derived, highlighting the choices undertaken for the terms responsible for the coupling between the vapor fraction transport equation and the system of mixture mass and momentum conservation. The coupling strategy is presented and its effects on the coupling stability and on the energy estimate on the velocity. Finally the numerical methods employed for the advance in time are presented as well as some implementation details.

3.1. Vapor fraction transport equation

In this section, the weak formulation of the vapor fracion transport equation (2.64) is spatially discretized. An additional stabilization term is added in (3.23) to face stabilization problems arising for low values of the diffusion parameter κ, when (2.64) becomes a transport-dominated problem.

3.1.1. Space discretization

Let us define the finite element spaces used for numerical discretization:

$$\Phi^h := \Phi \cap X_r^h,$$
$$\Phi_0^h := \Phi_0 \cap X_r^h,$$

wherein X_r^h is the space of piecewise Lagrangian polynomial functions of degree $r \geq 1$ on each element K of the partition $\mathcal{T}^h$ of Ω:

$$X_r^h := \{x^h \in C^0(\bar{\Omega}) : x^h|_K \in \mathbb{P}_r, \forall K \in \mathcal{T}^h\}. \tag{3.1}$$

The weak formulation of the equation describing the evolution of the volume vapor fraction α can be spatially dicretized and the following Galerkin problem is obtained:

for all $t \in (0,T)$, find $\alpha^h \in \Phi^h$, with $\alpha(0) = \alpha_0$:

$$\left(\frac{\partial \alpha^h}{\partial t}, \phi^h\right) - \left(\alpha^h \mathbf{u}^h, \nabla \phi^h\right) + \left(\kappa \nabla \alpha^h, \nabla \phi^h\right) - \left(\frac{\dot{S}_\alpha(\alpha^h, P^h)}{\rho_v}, \phi^h\right) = \left(\eta, \phi^h\right)_{\Gamma_N}, \tag{3.2}$$

for all $\phi^h \in \Phi_0^h$.

In (3.2), $\mathbf{u}^h$ and P^h are respectively the discrete counterparts of $\mathbf{u}$ and P and are responsible for the coupling with the system of mixture mass and momentum conservation.

3.1.2. SUPG stabilization of the vapor fraction equation

For low values of the diffusion parameter k, the equation for α becomes a convection-dominated transport problem and thus the numerical method could produce numerical instabilities and oscillations in the solution. To prevent these phenomena, a stabilization strategy is proposed: a stabilized and strongly consistent method can be obtained by adding a further term to the Galerkin approximation (3.2) [61], resulting in the following problem:

$$\forall t \in (0,T), \quad \text{find } \alpha^h \in \Phi^h: \quad a(\alpha^h, \phi^h) + \mathcal{L}_h(\alpha^h, f; \phi^h) = (\eta, \phi^h)_{\Gamma_N} \quad \forall \phi^h \in \Psi^h, \tag{3.3}$$

for a suitable form $\mathcal{L}_h(\alpha^h, f; \phi^h)$ satisfying

$$\mathcal{L}_h(\alpha^h, f; \phi^h) = 0 \quad \forall \phi^h \in \Phi^h. \tag{3.4}$$

A possible choice that verifies (3.4) is

$$\mathcal{L}_h(\alpha^h, f; \phi^h) = \sum_{K \in \mathcal{T}_h} (\frac{\partial \alpha^h}{\partial t} + L\alpha^h - f, \tau_\phi \mathcal{I}^{(\beta)}(\phi^h))_{L^2(K)}, \tag{3.5}$$

where

$$L\alpha = -\kappa \nabla \alpha + \nabla \cdot (\alpha \mathbf{u}) + \sigma \alpha, \tag{3.6}$$

$$\sigma \alpha = \frac{\partial \dot{S}_\alpha(\alpha, P)}{\partial \alpha} \alpha, \tag{3.7}$$

$$f = \dot{S}_\alpha(\alpha, P) - \sigma \alpha. \tag{3.8}$$

β and τ_ϕ are parameters to be determined, and

$$\mathcal{I}^{(\beta)}(\phi^h) = L_{SS}(\phi^h) + \beta L_s(\phi^h). \tag{3.9}$$

In equation (3.9), L_S and L_{SS} are the symmetric and the skew-symmetric part of the operator L, respectively. The choice $\beta = 0$ is made, which means that the additional term $\mathcal{L}_h$ corresponds to the *Streamline Upwind Petrov-Galerkin* (SUPG) stabilization scheme [9] which depends only on the skew-symmetric part of the linear operator L. In the following sections we derive the skew-symmetric part of L, and we provide an expression for the stabilization parameter τ_ϕ.

Skew-symmetric part of the operator

Let V be a Hilbert space and V' its dual. An operator $L : V \to V'$ is *symmetric* if:

$$ {}_{V'}\langle L\alpha, \rangle_V = {}_V\langle \alpha, L\phi \rangle_{V'} \qquad \forall \alpha, \phi \in V, \tag{3.10} $$

skew-symmetric when:

$$ {}_{V'}\langle L\alpha, \phi \rangle_V = - {}_V\langle \alpha, L\phi \rangle_{V'} \qquad \forall \alpha, \phi \in V. \tag{3.11} $$

An operator can be split into the sum of its symmetric part L_S and its skew-symmetric part L_{SS}, needed to obtain the expression of the SUPG stabilization term.

To identify L_S and L_SS, we consider two functions $\alpha, \phi \in H_0^1(\Omega)$, and starting from (3.6), we rewrite the transport term as $\nabla \cdot (\alpha \mathbf{u}) = \frac{1}{2}(\nabla \cdot \mathbf{u})\alpha + \frac{1}{2}\mathbf{u} \cdot \nabla\alpha + \frac{1}{2}\nabla \cdot (\alpha\mathbf{u})$:

$$ {}_{V'}\langle L\alpha, \phi \rangle_V = -\kappa(\Delta\alpha, v) + (\frac{1}{2}(\nabla \cdot \mathbf{u})\alpha, \phi) + (\frac{1}{2}\mathbf{u} \cdot \nabla\alpha, \phi) + (\frac{1}{2}\nabla \cdot (\alpha\mathbf{u}), \phi) + (\sigma\alpha, \phi). \tag{3.12} $$

The diffusion term and $(\frac{1}{2}\nabla \cdot (\alpha\mathbf{u}), \phi)$ are integrated by parts:

$$ {}_{V'}\langle L\alpha, \phi \rangle_V = \kappa(\nabla\alpha, \nabla\phi) + (\frac{1}{2}(\nabla \cdot \mathbf{u})\alpha, \phi) + (\frac{1}{2}\nabla\alpha, \phi\mathbf{u}) - (\frac{1}{2}\alpha\mathbf{u}, \nabla\phi) + (\sigma\alpha, \phi). \tag{3.13} $$

The term resulting from diffusion is again integrated by parts. The same is done for $(\frac{1}{2}\nabla\alpha, \phi\mathbf{u})$. The other terms are rearranged to recognise their contribution in the expression of ${}_V\langle \alpha, L\phi \rangle_{V'}$.

$$ {}_{V'}\langle L\alpha, \phi \rangle_V = -\kappa(\alpha, \Delta\phi) + (\alpha, \frac{1}{2}(\nabla \cdot \mathbf{u})\phi) - (\alpha, \frac{1}{2}\nabla \cdot (\phi\mathbf{u})) - (\alpha, \frac{1}{2}\mathbf{u} \cdot \nabla\phi) + (\alpha, \sigma\phi). \tag{3.14} $$

Reordering terms, one can write:

$$ {}_{V'}\langle L\alpha, \phi\rangle_V = -\kappa(\alpha, \Delta\phi) + (\alpha, \frac{1}{2}(\nabla\cdot\mathbf{u})\phi) + (\alpha, \sigma\phi) - (\alpha, \frac{1}{2}\nabla\cdot(\phi\mathbf{u})) - (\alpha, \frac{1}{2}\mathbf{u}\cdot\nabla\phi). \tag{3.15} $$

From the definition of L, the following holds:

$$ {}_{V}\langle \alpha, L\phi\rangle_{V'} = -\kappa(\alpha, \Delta\phi) + (\alpha, \frac{1}{2}(\nabla\cdot\mathbf{u})\phi) + (\alpha, \sigma\phi) + (\alpha, \frac{1}{2}\nabla\cdot(\phi\mathbf{u})) + (\alpha, \frac{1}{2}\mathbf{u}\cdot\nabla\phi). \tag{3.16} $$

The comparison between equation (3.15) and (3.16), following the definitions provided in (3.10) and (3.11) allows to write the expressions of the symmetric and skew-symmetric part of the L operator:

$$ L(\cdot) = L_S(\cdot) + L_{SS}(\cdot), \tag{3.17} $$

$$ L_S(\cdot) = -\kappa\Delta(\cdot) + \frac{1}{2}(\nabla\cdot\mathbf{u})(\cdot) + \sigma(\cdot), \tag{3.18} $$

$$ L_{SS}(\cdot) = \frac{1}{2}\mathbf{u}\cdot\nabla(\cdot) + \frac{1}{2}\nabla\cdot((\cdot)\mathbf{u}). \tag{3.19} $$

Choice of the stabilization parameter τ_ϕ

Following what has been proposed in [7], τ_ϕ is designed by asymptotic scaling arguments developed within the theory of stabilized methods in [71] and [32]. The resulting expression for τ_ϕ is the following:

$$ \tau_\phi = \left[\left(\frac{\sigma}{\Delta t}\right)^2 + \mathbf{u}\cdot\mathbf{G}\mathbf{u} + C_I\kappa^2\mathbf{G}:\mathbf{G} + s^2\right]^{-1/2}, \tag{3.20} $$

where σ is the order of the BDF scheme employed (see 3.3.1) and $\mathbf{G}$ is the element controvariant metric tensor, which is defined as

$$ G_{ij} = \sum_{k=1}^{3} \frac{\partial\xi_k}{\partial x_i}\frac{\partial\xi_k}{\partial x_j}. \tag{3.21} $$

$\mathbf{x} = \{x_i\}_{i=1}^3$ are the coordinates of the element K in physical space and $\xi = \{\xi_i\}_{i=1}^3$ the coordinates of the element $\hat{K}$ in parametric space. $\frac{\partial\xi}{\partial\mathbf{x}}$ is the inverse Jacobian of the element mapping between the reference and the physical domain. C_I is a positive constant, independent of the mesh size, derived from an element-wise inverse estimate [19, 28], and based on the polynomial degree r of the finite element space: $C_I = 60\cdot 2^{r-2}$. s the partial derivative of the mass transfer rate with respect to the local vapor fraction:

$s = \frac{\partial \dot{S}_\alpha}{\partial \alpha}$. For the Zwart model s reads:

$$s = -F_{vap}\frac{3r_{nuc}\rho_v}{R_B}\sqrt{\frac{2}{3}\frac{\max(P_v - P, 0)}{\rho_l}} - F_{cond}\frac{3\rho_v}{R_B}\sqrt{\frac{2}{3}\frac{\max(P - P_v, 0)}{\rho_l}}. \tag{3.22}$$

Stabilized weak formulation

The SUPG stabilization term is added to the weak formulation (3.2). The space discretized stabilized weak formulation of the α transport equation reads:

for all $t \in (0, T)$, find $\alpha^h \in \Phi^h$, with $\alpha(0) = \alpha_0$:

$$\begin{aligned}\left(\frac{\partial \alpha^h}{\partial t}, \phi^h\right) - \left(\alpha^h \mathbf{u}^h, \nabla \phi^h\right) + \left(\kappa \nabla \alpha^h, \nabla \phi^h\right) - \left(\frac{\dot{S}_\alpha(\alpha^h, P^h)}{\rho_v}, \phi^h\right) + \\ + C_S \sum_{K \in \mathcal{T}^h} \left[\left(\tau_\phi(\mathbf{u}^h) r_\phi(\alpha^h, \mathbf{u}^h, P^h)), \mathbf{u}^h \cdot \nabla \phi^h + \frac{1}{2}(\nabla \cdot \mathbf{u}^h)\phi^h\right)\right)_K\Big] \\ = \left(\eta, \phi^h\right)_{\Gamma_N},\end{aligned} \tag{3.23}$$

for all $\phi^h \in \Phi_0^h$.

The first line represents the standard Galerkin finite element terms. The second line consists of the SUPG stabilization terms where:

- K denotes a generic cell of the mesh $\mathcal{T}_h$;
- C_S is an arbitrary coefficient, in the following $C_S = 1.0$;
- the residual r_ϕ has the following expression:

$$r_\phi(\alpha^h, \mathbf{u}^h, P^h)) = \frac{\partial \alpha^h}{\partial t} + \nabla \cdot (\alpha^h \mathbf{u}^h) - \kappa \Delta \alpha^h - \frac{\dot{S}_\alpha(\alpha^h, P^h)}{\rho_v}; \tag{3.24}$$

- the stabilization parameter τ_ϕ has the following expression:

$$\tau_\phi = \left[\left(\frac{\sigma}{\Delta t}\right)^2 + \mathbf{u}^h \cdot \mathbf{G}\mathbf{u}^h + C_I \kappa^2 \mathbf{G} : \mathbf{G} + s^2\right]^{-1/2}. \tag{3.25}$$

3.2. Mixture mass and momentum conservation

In this section the space discretization of the system of the mixture mass and momentum conservation is presented. In section 3.2.2, a stabilization term is added to (3.28), following the same steps performed in section 3.1.2 to obtain (3.23).

3.2.1. Space discretization

Let us define the finite element spaces for the numerical discretization:

$$\mathcal{V}_g^h = V_g^h \times Q^h, \tag{3.26}$$
$$\mathcal{V}_0^h = V_0^h \times Q^h. \tag{3.27}$$

where $V_g^h := V_g \cap [X_r^h]^3$, $V_0^h := V_0 \cap [X_r^h]^3$, $Q^h := Q \cap X_r^h$. The Galerkin problem for (2.59) reads:

for all $t \in (0,T)$, find $\{\mathbf{u}^h, P^h\} \in \mathcal{V}_g^h$ with $\mathbf{u}^h(0) = \mathbf{u}_0$:

$$\begin{aligned}\Big(\rho^h \frac{\partial \mathbf{u}^h}{\partial t}, \mathbf{v^h}\Big) + \big(\rho^h \mathbf{u}^h \cdot \nabla \mathbf{u}^h, \mathbf{v}^h\big) + \big(2\mu^h \nabla^S \mathbf{u}^h, \nabla \mathbf{v}^h\big) - \big(P^h, \nabla \cdot \mathbf{v}^h\big) + \\ + \big(\nabla \cdot \mathbf{u}^h, q^h\big) - \Big(\big(\frac{1}{\rho_v} - \frac{1}{\rho_l}\big)\dot{S}_\alpha(\rho^h, P^h), q^h\Big) = \big(\mathbf{h}, \mathbf{v}^h\big)_{\Gamma_N},\end{aligned} \tag{3.28}$$

for all $\{\mathbf{v}^h, q^h\} \in \mathcal{V}_0^h$,

In the formulation (3.28), ρ^h and μ^h are the mixture density and viscosity respectively, computed as weighted mean of the liquid and vapor properties following the definitions (2.6) and (2.7). The value of α^h is computed on each quadrature point thanks to the coupling with the transport equation.

3.2.2. Stabilization terms

The problem (3.28) is stabilized adding to the weak formulation the SUPG terms. Here only the final form of the semi-discrete formulation is reported since the formulation of the stabilization is already available in the literature [19]:

for all $t \in (0,T)$, find $\{\mathbf{u}^h, P^h\} \in \mathcal{V}_g^h$ with $\mathbf{u}^h(0) = \mathbf{u}_0$:

$$\begin{aligned}\Big(\rho^h \frac{\partial \mathbf{u}^h}{\partial t}, \mathbf{v^h}\Big) + \big(\rho^h \mathbf{u}^h \cdot \nabla \mathbf{u}^h, \mathbf{v}^h\big) + \big(2\mu^h \nabla^S \mathbf{u}^h, \nabla \mathbf{v}^h\big) - \big(P^h, \nabla \cdot \mathbf{v}^h\big) + \\ + \big(\nabla \cdot \mathbf{u}^h, q^h\big) - \Big(\big(\frac{1}{\rho_v} - \frac{1}{\rho_l}\big)\dot{S}_\alpha(\rho^h, P^h), q^h\Big) + \\ + C_S \sum_{K \in \mathcal{T}_h} \Big[\Big(\tau_M(\mathbf{u}^h)\mathbf{r}_M(\alpha^h, \mathbf{u}^h, P^h)), \rho^h \mathbf{u}^h \cdot \nabla \mathbf{v}^h + \nabla q^h\Big)_K + \\ + \Big(\tau_C(\mathbf{u}^h) r_C(\alpha^h, \mathbf{u}^h, P^h)), \nabla \cdot \mathbf{v}^h\Big)_K\Big] = \big(\mathbf{h}, \mathbf{v}^h\big)_{\Gamma_N},\end{aligned} \tag{3.29}$$

for all $\{\mathbf{v}^h, q^h\} \in \mathcal{V}_0^h$.

The first and second line represent the Galerkin finite element terms. The third and fourth line consist of the SUPG stabilization terms where:

- the residual $\mathbf{r}_M$ has the following expression:

$$\mathbf{r}_M(\alpha^h, \mathbf{u}^h, P^h) = \rho^h \frac{\partial \mathbf{u}^h}{\partial t} + \rho^h \mathbf{u}^h \cdot \nabla \mathbf{u}^h + \nabla P^h - \mu^h \Delta \mathbf{u}^h; \tag{3.30}$$

- the residual r_C has the following expression:

$$r_C(\alpha^h, \mathbf{u}^h, P^h) = \nabla \cdot \mathbf{u}^h - \Big(\frac{1}{\rho_v} - \frac{1}{\rho_l}\Big)\dot{S}_\alpha(\alpha^h, P^h); \tag{3.31}$$

- the stabilization parameter τ_M has the following expression:

$$\tau_M(\alpha^h, \mathbf{u}^h) = \Big[(\rho^h)^2\Big(\frac{\sigma}{\Delta t}\Big)^2 + (\rho^h)^2 \mathbf{u}^h \cdot \mathbf{G}\mathbf{u}^h + C_r(\mu^h)^2 \mathbf{G} : \mathbf{G}\Big]^{-1/2}; \tag{3.32}$$

- the stabilization parameter τ_C has the following expression:

$$\tau_C(\alpha^h, \mathbf{u}^n) = \big(\tau_M \mathbf{g} \cdot \mathbf{g}\big)^{-1}. \tag{3.33}$$

In the above definitions $C_r = 60 \cdot 2^{2-r}$ as in (3.20) and $\mathbf{g}$ is the metric vector defined as:

$$g_i = \sum_{k=1}^{3} \frac{\partial \xi_k}{\partial x_i}. \tag{3.34}$$

3.3. Time discretization and coupling strategy

In this section the time discretization of (3.23) and (3.29) is analyzed, then the coupling between the problems is described. A segregated approach is followed, as done in the original model proposed by Zwart [85]. This provides two unique advantages compared to monolithic couplings: firstly it ensures simplicity of linearization and implementation, and secondly it provides the flexibility to possibly couple additional governing equations as demanded by the case being studied. For example, additional equations for turbulence modeling and the ALE mesh update can be similarly coupled using a staggered partitioned method.

3.3.1. Time discretization

For time discretization, employ the Backward Difference Formula (BDF) [62], a family of linear multi-step methods that approximates the derivative of a function at a specific time step t_n as a function of the prevoius timesteps $(t_{n+1}, t_{n-2}, \dots)$. The number of the timesteps considered is the order of the BDF scheme, denoted with σ. Examples of BDF schemes of order $\sigma = 1$ and $\sigma = 2$ are reported in the next paragraph.

Given a uniform timestep Δt, $\mathbf{u}_n^h$, P_n^h and α_n^h are the approximations of $\mathbf{u}^h$, P^h and α^h at time $t_n = n\Delta t$. The time derivatives are therefore approximated as:

$$\frac{\partial \mathbf{u}^h}{\partial t} \approx \frac{\alpha_\sigma \mathbf{u}_{n+1}^h - \mathbf{u}_{n,BDF_\sigma}^h}{\Delta t}, \tag{3.35}$$

$$\frac{\partial \alpha^h}{\partial t} \approx \frac{\alpha_\sigma \alpha_{n+1}^h - \alpha_{n,BDF_\sigma}^h}{\Delta t}, \tag{3.36}$$

where

$$\mathbf{u}_{n,BDF_\sigma}^h = \begin{cases} \mathbf{u}_n^h & \text{for } \sigma = 1, \text{ if } n \geq 1; \\ 2\mathbf{u}_n^h - \frac{1}{2}\mathbf{u}_{n-1}^h & \text{for } \sigma = 2, \text{ if } n \geq 2; \end{cases} \tag{3.37}$$

$$\alpha_{n,BDF_\sigma}^h = \begin{cases} \alpha_n^h & \text{for } \sigma = 1, \text{ if } n \geq 1; \\ 2\alpha_n^h - \frac{1}{2}\alpha_{n-1}^h & \text{for } \sigma = 2, \text{ if } n \geq 2; \end{cases} \tag{3.38}$$

and

$$\alpha_\sigma = \begin{cases} 1 & \text{for } \sigma = 1; \\ \frac{3}{2} & \text{for } \sigma = 2; \end{cases} \tag{3.39}$$

It is worth mentioning the choices undertaken to treat the non-linearities of the problem, due to the convection term $(\rho \mathbf{u}^h \cdot \nabla \mathbf{u}^h)$ in (3.29) and the coupling of the two problems. When needed, a semi-implicit approach is be used in which the non-linear terms $\mathbf{u}_{n+1}^h$ and P_{n+1}^h are extrapolated at time t_{n+1} with Newton-Gregory polynomials [69] as follows:

$$\mathbf{u}_{n+1,EXT_\sigma}^h = \begin{cases} \mathbf{u}_n^h & \text{for } \sigma = 1, \text{ if } n \geq 0; \\ 2\mathbf{u}_n^h - \mathbf{u}_{n-1}^h & \text{for } \sigma = 2, \text{ if } n \geq 1; \end{cases} \tag{3.40}$$

$$P_{n+1,EXT_\sigma}^h = \begin{cases} P_n^h & \text{for } \sigma = 1, \text{ if } n \geq 0; \\ 2P_n^h - P_{n-1}^h & \text{for } \sigma = 2, \text{ if } n \geq 1. \end{cases} \tag{3.41}$$

3.3.2. Fully discretized problem

The fully discrete formulation of problem (3.23) is:

find $\alpha^h_{n+1} \in \Phi^h$:

$$\begin{aligned}
&\Big(\frac{\alpha_\sigma \alpha^h_{n+1} - \alpha^h_{n,BDF_\sigma}}{\Delta t}, \phi^h\Big) - \big(\alpha^h_{n+1}\mathbf{u}^h_{n+1,EXT_\sigma}, \nabla\phi^h\big) + \\
&+\big(\kappa\nabla\alpha^h_{n+1}, \nabla\phi^h\big) - \Big(\frac{\dot{S}_\alpha(\alpha^h_{n+1}, P^h_{n+1,EXT_\sigma})}{\rho_v}, \phi^h\Big) + \\
&+\sum_{K\in\mathcal{T}_h}\Big[\Big(\tau_\phi(\mathbf{u}^h_{n+1,EXT_\sigma}) r_\phi(\alpha^h_{n+1}, \mathbf{u}^h_{n+1,EXT_\sigma}, P^h_{n+1,EXT_\sigma})), \mathbf{u}^h_{n+1,EXT_\sigma}\cdot\nabla\phi^h\Big)_K + \\
&+\Big(\tau_\phi(\mathbf{u}^h_{n+1,EXT_\sigma}) r_\phi(\alpha^h_{n+1}, \mathbf{u}^h_{n+1,EXT_\sigma}, P^h_{n+1,EXT_\sigma})), \frac{1}{2}(\nabla\cdot\mathbf{u}^h_{n+1,EXT_\sigma})\phi^h\Big)_K\Big] = \\
&= \big(\eta_{n+1}, \phi^h\big)_{\Gamma_N},
\end{aligned} \tag{3.42}$$

for all $\phi^h \in \Phi^h_0$, for all $n \geq \sigma - 1$.

The fully discrete formulation of (3.29) is:

find $\{\mathbf{u}^h_{n+1}, P^h_{n+1}\} \in \mathcal{V}^h_g$:

$$\begin{aligned}
&\Big(\rho^h(\alpha^h_{n+1})\frac{\alpha_\sigma \mathbf{u}^h_{n+1} - \mathbf{u}^h_{n,BDF_\sigma}}{\Delta t}, \mathbf{v^h}\Big) + \big(\rho^h(\alpha^h_{n+1})\mathbf{u}^h_{n+1,EXT_\sigma}\cdot\nabla\mathbf{u}^h_{n+1}, \mathbf{v}^h\big) + \\
&+(2\mu^h(\alpha^h_{n+1})\nabla^S\mathbf{u}^h_{n+1}, \nabla\mathbf{v}^h) - \big(P^h_{n+1}, \nabla\cdot\mathbf{v}^h\big) + \\
&+\big(\nabla\cdot\mathbf{u}^h_{n+1}, q^h\big) - \Big(\big(\frac{1}{\rho_v} - \frac{1}{\rho_l}\big)\dot{S}_\alpha(\rho^h(\alpha^h_{n+1}), P^h_{n+1}), q^h\Big) + \\
&+\sum_{K\in\mathcal{T}_h}\Big[\Big(\tau_M(\mathbf{u}^h_{n+1,EXT_\sigma})\mathbf{r}_M(\alpha^h_{n+1}, \mathbf{u}^h_{n+1}, P^h_{n+1})), \rho^h\mathbf{u}^h_{n+1,EXT_\sigma}\cdot\nabla\mathbf{v}^h + \nabla q^h\Big)_K + \\
&+\Big(\tau_C(\mathbf{u}^h_{n+1,EXT_\sigma}) r_C(\alpha^h_{n+1}, \mathbf{u}^h_{n+1}, P^h_{n+1})), \nabla\cdot\mathbf{v}^h\Big)_K\Big] = \\
&= \big(\mathbf{h}_{n+1}, \mathbf{v}^h\big)_{\Gamma_N},
\end{aligned} \tag{3.43}$$

for all $\{\mathbf{v}^h, q^h\} \in \mathcal{V}^h_0$, for all $n \geq \sigma - 1$,

In the source term $\dot{S}_\alpha$, the dependence on pressure is treated with an implicit strategy in (3.43) and an explicit one in (3.42). In principle, the latter may introduce a constraint on the choice of Δt to ensure the stability of the scheme, but the energy estimate that will presented in the section 3.4 and the computational results that are going to be discussed in the next chapters show that such constraint is not extremely strict.

Regarding $\dot{S}_\alpha$ in (3.43), an explicit treatment of pressure $\dot{S}_\alpha(\alpha^h_{n+1}, P^h_n)$ would make such term significantly large for large timesteps because the difference between the local pres-

sure and the vapor pressure is not bounded. This would yield large values of the velocity divergence and thus to high velocity values where cavitation occurs. On the other hand, treating pressure implicitly limits the value of the right-hand side. This reasoning is justified by the energy estimate on the velocity, which is presented in section 3.4.

3.3.3. Numerical methods and solver algorithm

In this section the numerical methods employed to solve (3.42) and (3.43) are presented and the solver algorithm for the coupled problem is developed.

In order to numerically solve the coupled problem, a staggered approach is employed: the transport equation of the vapor fraction and the mixture mass and momentum system are solved sequentially at each timestep. In these settings the outline of the solution procedure is the following:

We define a uniform partition $t_n = n\Delta t$, $n = 0, 1, \dots,$ of the time interval. The quantities at time t_n are known; then for each $n = 0, 1, \dots,$

1. Evaluate $\mathbf{u}^h_{n+1,EXT_\sigma}$ and P^h_{n+1,EXT_σ} on the Gaussian quadrature points of the elements of the computational grid;
2. Solve a time step of the SUPG-stabilized, linear discrete vapor transport problem stated in (3.42) to obtain the distribution of vapor fraction at the following timestep α^h_{n+1};
3. Evaluate α^h_{n+1} on the Gaussian quadrature points of the elements of the computational grid;
4. Solve a time step of the SUPG-stabilized, semi-implicit mixture mass and momentum conservation system stated in (3.43) to obtain the mixture velocity and pressure at the following timestep $\mathbf{u}^h_{n+1}$ and P^h_{n+1}.

In step 2, the linear system resulting from the discretization of the vapor fraction transport equation is solved by the GMRES method [65], using the L_2 norm of the absolute residual as stopping criterion, with a tolerance of 10^{-7}. The block-wise preconditioner aSIMPLE [15], combined with an algebraic multigrid approximation of the single blocks, is employed to speed up the solution of the linear system.

In step 4, the semi-implicit formulation is employed for the advection term. However, this formulation is not linear because pressure is under a square root in $\dot{S}_\alpha$. The non-linear system is solved by means of Newton's method: at each non-linear step $k = 1, 2, \dots, N_{\max}$, until convergence, the jacobian matrix and the residual vector are computed. The lin-

earized system is solved for the increments $\delta\mathbf{u}_{n+1}^{k+1}$ and δP_{n+1}^{k+1}, and the solution is updated as:

$$\mathbf{u}_{n+1}^{k+1} = \mathbf{u}_{n+1}^{k} - \delta\mathbf{u}_{n+1}^{k+1}; \tag{3.44}$$

$$P_{n+1}^{k+1} = P_{n+1}^{k} - \delta P_{n+1}^{k+1}. \tag{3.45}$$

3.3.4. Implementation details

The fully discretized problems (3.42) and (3.43) have been implemented in `life`$^{\mathtt{x}}$ [3], a high performance Finite Element library, written in C++ and based on deal.II [1] finite element core. The transport equation of the volume vapor fraction and the mass and momentum conservation system are solved sequentially at each timestep, hinging upon specific C++ classes: the *FluidDynamics* class and the *CavitationModel* class. Another class, named *CavitationFluid*, contains an instance of both *FluidDynamics* and *CavitationModel* and it is responsible for the interaction between the two sub-classes.

The *FluidDynamics* class, already present in the library, has been modified to consider the effect of the cavitation model on the Navier-Stokes system: when cavitation is active, the continuity equation and the expression of the residuals are properly modified, as well as the definition of the mixture density and viscosity, which have different values in the domain, depending on the value of α on the quadrature points required for the assembling of the finite element approximation of the problems.

The *CavitationModel* class has been developed from scratch; it is responsible for modelling the transport equation for the volume vapor fraction by solving the fully discretized problem (3.42).

The classes are able to interact thanks to the *CavitationFluid* class; this is needed because the two problems are coupled by the variables α, $\mathbf{u}$ and P. Algorithm 1 briefly describes the solution strategy: at each time step the values of the mixture velocity $\mathbf{u}$ and pressure P are computed on the quadrature points and passed to *CavitationModel*. Then the finite element system coming from the α transport equation is assembled considering velocity and pressure as known parameters, resulting in a linear system in α.

Once the equation for α is solved, few sanity checks are performed. This is done because the presence of high gradients, due to the interface between regions with positive and null values for α, could produce unbounded oscillations of α. This problem is partially addressed introducing the artificial diffusivity κ and choosing a small enough timestep but still oscillations to negative value of α are possible. This is unphysical and could introduce numerical instability because the value of α is directly related to the value of the local

density and viscosity. For this reason, at the end of each timestep, the solution of the equation for α is bounded between 0 and 1. This is a common practice in homogeneous mixture models as the same is done in Fluent 17.2 (ANSYS Inc., USA) [2] for similar cavitation models. At the same time, when cavitation is not active, meaning that $P > P_v$ in all the domain, numerical errors could produce a non-zero α field which is summed to the value of α at the previous time step. This results in an unphysical accumulation of α which produces numerical instabilities after several timesteps. Again, this problem is solved through a sanity check on the value of α. If $\alpha \leq 10^{-6}$, the effect of cavitation is considered negligible, hence α is forced to be null.

Once the sanity checks have been performed, the value of α on the quadrature points is passed to the *FluidDynamics* class, where the modified Navier-Stokes system is solved, considering the value of α known. To foster the stability of the coupled solver, in the continuity equation in (3.43) P_{n+1} is used. This requires to use a non-linear solver for the Navier-Stokes system as $\dot{S}_\alpha$ is a non-linear function of the pressure in Zwart model [85]. For this reason the Navier-Stokes system is linearized and solved by means of Newton's method. The linearization process is handled directly by the Automatic Differentiation (AD) tool available in `deal.II` [1]. The tool requires to use continuous functions, but $\dot{S}_\alpha \notin C^0(\mathbb{R})$ in the variable P due to the max function. For this reason in the actual implementation, the max function is smoothed as following:

$$\max(x_1, x_2) = \frac{(x_1 + x_2) + \sqrt{(x_1 - x_2)^2 + \epsilon}}{2}, \tag{3.46}$$

with a small parameter $\epsilon = 10^{-6}$.

Once the Navier-Stokes system is solved, time advances to the next timestep, updating the boundary conditions and the velocity and pressure values on the quadrature points. Algorithm 1 schematically summarizes the solution strategy implemented in the software.

3.4. Energy estimate

In this section, we present an energy estimate on the mixture velocity. We compare the estimate for the incompressible Navier-Stokes system to the same computed for the mixture mass and momentum system employed in the cavitation model. This is done to understand the effects on the energy estimate of the non-zero velocity divergence due to evaporation and condensation processes occurring in cavitating flows. In this section, the dependence of density and viscosity on alpha will be neglected; this allows to keep the computation simpler and isolate and recognize the role of the non-zero divergence in the

Algorithm 1 Partitioned coupling of mixture mass and momentum system with the vapor fraction transport solvers

Input: $\mathbf{u}_0$, P_0, α_0
for $n \leftarrow 0$ to n_{last} **do**
  Compute velocity and pressure fields on quadrature points: $\mathbf{u}_{n+1,EXT_\sigma}$, P_{n+1,EXT_σ}
  Cavitation linear solver: Solve for α_{n+1}
  Perform sanity checks on α_{n+1}
  Output α_{n+1}
  Compute α on quadrature points: α_{n+1}
  Interpolate density and viscosity fields: $\rho(\alpha_{n+1})$, $\mu(\alpha_{n+1})$
  for $k \leftarrow 0$ to convergence or k_{max} **do**
    Newton non linear iteration:
    Fluid dynamics linear solver: Solve for the update on $\mathbf{u}_{n+1}$, P_{n+1}
  end for
  Output $\mathbf{u}_{n+1}$ and P_{n+1}
end for

energy estimate.

If the incompressible Navier-Stokes system is considered:

$$\begin{cases} \rho\dfrac{\partial \mathbf{u}}{\partial t} + \rho\mathbf{u}\cdot\nabla\mathbf{u} - \mu\Delta\mathbf{u} + \nabla P = 0 & \text{in } \Omega\times(0,T], \\ \nabla\cdot\mathbf{u} = 0 & \text{in } \Omega\times(0,T], \\ \mathbf{u} = 0 & \text{on } \partial\Omega\times(0,T], \\ \mathbf{u} = \mathbf{u_0} & \text{in } \Omega\times\{0\}. \end{cases} \tag{3.47}$$

the following energy estimate holds [18]:

$$||\mathbf{u}(t)||^2_{L^2} + \int_0^t \mu||\nabla\mathbf{u}(\tau)||^2_{L^2}d\tau \leq C||\mathbf{u}(0)||^2_{L^2}, \qquad \forall t\in[0,T), \tag{3.48}$$

with some constant $C = C(\Omega) > 0$. The energy estimate (3.48) can be obtained by eliminating the pressure contribution with an Helmholtz-Leray projection and considering that the advection term produces a null contribution in the energy balance. These two considerations hold if only if velocity is a solenoidal field, hence it is not valid in the cavitating case.

We consider the following system; in (3.49) the velocity divergence has a non null value

in the domain Ω:

$$\begin{cases} \rho\dfrac{\partial \mathbf{u}}{\partial t} + \rho\mathbf{u}\cdot\nabla\mathbf{u} - \mu\Delta\mathbf{u} + \nabla P = 0 & \text{in } \Omega\times(0,T], \\ \nabla\cdot\mathbf{u} = k & \text{in } \Omega\times(0,T], \\ \mathbf{u} = \mathbf{g} & \text{on } \partial\Omega\times(0,T], \\ \mathbf{u} = \mathbf{u_0} & \text{in } \Omega\times\{0\}. \end{cases} \tag{3.49}$$

Computing the energy estimate for (3.49) is a more difficult task because all the simplifications performed thanks to $\nabla\cdot\mathbf{u} = 0$ are no longer valid.

Following the procedure developed in [18], we use a perturbation argument and write $\mathbf{u} = \mathbf{v} + \mathbf{E}$ where $\mathbf{E}$ is the solution of the Stokes problem reported below with some associated pressure h:

$$\begin{cases} \rho\dfrac{\partial \mathbf{E}}{\partial t} - \mu\Delta\mathbf{E} + \nabla h = 0 & \text{in } \Omega\times(0,T], \\ \nabla\cdot\mathbf{E} = k & \text{in } \Omega\times(0,T], \\ \mathbf{E} = \mathbf{g} & \text{on } \partial\Omega\times(0,T], \\ \mathbf{E} = \mathbf{E_0} & \text{in } \Omega\times\{0\}. \end{cases} \tag{3.50}$$

Substituting the definition of $\mathbf{u} = \mathbf{v} + \mathbf{E}$ in (3.49), the system becomes:

$$\begin{cases} \rho\dfrac{\partial \mathbf{v}}{\partial t} - \mu\Delta\mathbf{v} + \rho(\mathbf{v}+\mathbf{E})\cdot\nabla(\mathbf{v}+\mathbf{E}) + \nabla P^* = 0 & \text{in } \Omega\times(0,T], \\ \nabla\cdot\mathbf{v} = 0 & \text{in } \Omega\times(0,T], \\ \mathbf{v} = 0 & \text{on } \partial\Omega\times(0,T], \\ \mathbf{v} = \mathbf{v_0} & \text{in } \Omega\times\{0\}, \end{cases} \tag{3.51}$$

with associated pressure $P^* = P - h$ and homogeneous conditions for $\mathbf{v}$.

The system presented in (3.51) is called *perturbed Navier-Stokes system*. It is possible to prove the following theorem which provides an energy estimate similar to the one obtained in the incompressible framework [18]:

Theorem 3.1. *Suppose:*

$$\begin{gathered} \mathbf{v_0} \in L^2(\Omega), \\ \mathbf{E} \in L^s(0,T;L^q(\Omega)), \quad \nabla\cdot\mathbf{E} = k \in L^4(0,T;L^2(\Omega)), \\ 4 \le s < \infty, \quad 4 \le q < \infty, \quad \frac{2}{s} + \frac{3}{q} = 1, \end{gathered}$$

Then there exists at least one weak solution $\mathbf{v}$ *of the perturbed system (3.51) in* $[0,T)\times\Omega$ *with initial data* $\mathbf{v}_0$. *The solution* $\mathbf{v}$ *satisfies with some constant* $C = C(\Omega) > 0$ *the following energy estimate*[1]*:*

$$||\mathbf{v}(t)||_{L_2}^2 + \int_0^\tau \mu||\nabla\mathbf{v}(\tau)||_{L_2}^2 d\tau \leq C\Big(||\mathbf{v_0}||_{L_2}^2 + \int_0^t ||\mathbf{E}(\tau)||_{L_4}^4 d\tau\Big)\exp(C||k||_{2,4;t}^4 + C||\mathbf{E}||_{q,s;t}^s), \tag{3.52}$$

for each $0 \leq t < T$.

Differently from the energy estimate for the incompressible Navier-Stokes system (3.48), in (3.52), new terms appear in the upper bound of the energy estimate. Let us focus on the definition of κ in the Zwart cavitation model:

$$k = \dot{S}_\alpha(\alpha, P) = \underbrace{F_{vap}\frac{3r_{nuc}(1-\alpha)\rho_v}{R_B}\sqrt{\frac{2}{3}\frac{\max(P_v - P, 0)}{\rho_l}}}_{\text{(vaporization)}} - \underbrace{F_{cond}\frac{3\alpha\rho_v}{R_B}\sqrt{\frac{2}{3}\frac{\max(P - P_v, 0)}{\rho_l}}}_{\text{(condensation)}}. \tag{3.53}$$

In the definition of k in the Zwart cavitation model, the pressure plays an important role in the vaporization and condenstation terms: if at a specific timestep t^*, the pressure reduces to below the vapor pressure, k is no longer zero and the upper bound of the energy estimate at t^* changes according to Theorem 3.1, since some energy contribution is injected in the system. To limit the amount of energy injected in the system when some liquid evaporates, the pressure in the definition of $\dot{S}_\alpha$ in the mixture mass conservation (3.43) is treated implicitly (P_{n+1}) as mentioned in section 3.3.2. By doing so, the resulting pressure of the mixture does not reduce much with respect to the vapor pressure P_v and the energy injected in the system is limited. This is confirmed by the numerical results: if an explicit formulation in time (P_n) is used in the definition of $\dot{S}_\alpha$, the resulting mixture velocity magnitude is overestimated and the model provides unphysical results, mainly because too much energy has been introduced in the system. If, instead, an implicit formulation in time (P_{n+1}) is used, the system is stable and provides significant results which match the expected outcomes when compared to the literature.

[1]For $1 \leq, s \leq \infty$ the Bochner space $L^s(0,T;L^q(\Omega))$ is equipped with the norm $||\cdot||_{q,s;t} = (\int_0^t ||\cdot||_q^s d\tau)^{\frac{1}{s}}$ when $s < \infty$ and $||\cdot||_{q,\infty;t} = \operatorname{ess\,sup}_{(0,t)} ||\cdot||_q$ when $s = \infty$.

4 | Numerical simulation of the cavitating cylinder benchmark

In this chapter, numerical results of the first benchmark are presented. The homogeneous mixture model described in the previous chapters is used to study the transient cavitation over a circular cylinder. This benchmark has been selected because it allows a simple representation of cavitation phenomena past bluff bodies; although cavitation on lifting bodies has been extensively studied both experimentally and numerically, relatively fewer studies exist for bluff bodies. However, the final aim of this thesis work is to provide a tool able to simulate cavitation across cardiac valves, which are not streamlined, thus cavitation over bluff bodies has to be take into account. To numerically validate our model, we compare our results with the work of [26]; similarly to the model developed in this thesis, the cavitation model used in [26] is an homogeneous mixture model.

Figure 4.1 shows the schematic of a low-Reynolds-number cavitating flow over a cylinder. As the liquid accelerates past the bluff body, pressure drops in the shear layer, resulting in cavitation inception. The shear layer then rolls up into vortexes and, depending on the conditions, the vortexes can also cavitate. These vortexes are shed from the body into the relatively high-pressure region in the wake, where vapor bubbles collapse due to the higher pressure.

The numerical simulations are preformed at low Reynolds number in the computational domain shown in Figure 4.2. The solver is tridimensional but for this test case the mesh has only one element in the third direction; this is done to lower the computational time and does not ruin the quality of the results, since the flow is laminar. The domain is chosen wide enough to be able to capture the wake of the cylinder, moreover the cylinder has a small offset with respect to the centerline of the domain since the center is located $0.05D$ upwards with respect to the centerline, where D is the diameter of the cylinder. This is done to ensure that this geometry results in vortex shedding at moderate Reynolds numbers as usually done for low Reynolds cylinder benchmarks [67]. More details on the grid generation process are provided in the section 4.1.

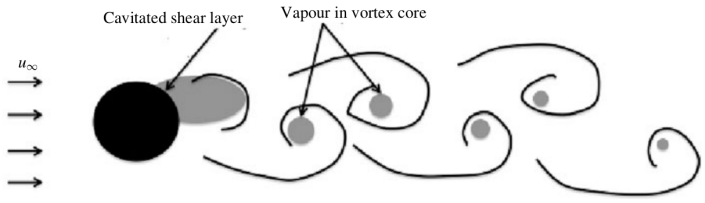

Figure 4.1: **Schematic of vortex shedding and vapour formation in flow over a circular cylinder at low Reynolds number.** Taken from [26]

In section 4.3, we present the numerical results of the cavitating cylinder benchmark: we perform a comparison between cavitating and non-cavitating flows and we compare our results with the one form [26]; to perform a comparison, we ensure the same values of the adimensional groups describing the flow.

We fix the value of the Reynolds number computed using the upstream quantities and the cylinder diameter D: $\mathbb{R}e = \frac{\rho u D}{\mu} = 200$.

The cavitation number $\sigma = \frac{P - P_v}{1/2 \rho u^2}$ is computed using the outlet pressure as reference. Different values of σ are achieved by varying the value of the outlet pressure, keeping constant the value of the vapor pressure P_v. A non-cavitating case is analysed, where $\sigma = 2$, as well as a cavitating setup, where $\sigma = 1.0$.

The density and viscosity ratios R_ρ and R_μ are computed by using the values for blood, which are similar to the one found for water. At an ambient temperature of 37°C, which is the physiological working temperature for blood, density and viscosity for the liquid and saturated vapor are [45]:

$$\rho_l = 1060 \quad \text{kg/m}^3 \qquad \mu_l = 3.30 \cdot 10^{-3} \quad \text{Pa·s}$$
$$\rho_v = 0.485 \quad \text{kg/m}^3 \qquad \mu_v = 4.71 \cdot 10^{-5} \quad \text{Pa·s}$$

The resulting values for the density and viscosity ratios are:

$$R_\rho = 4.85 \cdot 10^{-4} \qquad R_\mu = 1.43 \cdot 10^{-2}$$

Regarding the cavitation model, a tuning of the evaporation and condensation constant has been performed. This is a normal practice for homogeneous mixture models [52] that depend on user defined constants. In this test case $F_{\text{vap}} = 50.0$, $F_{\text{cond}} = 0.1$.

As for the temporal discretization, in the following simulations we use a fixed value of the time step: $\Delta t = 10^{-3}$ s which ensured stable solutions. If it is normalized through the reference quantities, the dimensionless timestep reads: $\Delta \bar{t} = \Delta t u_\infty / D = 0.02$.

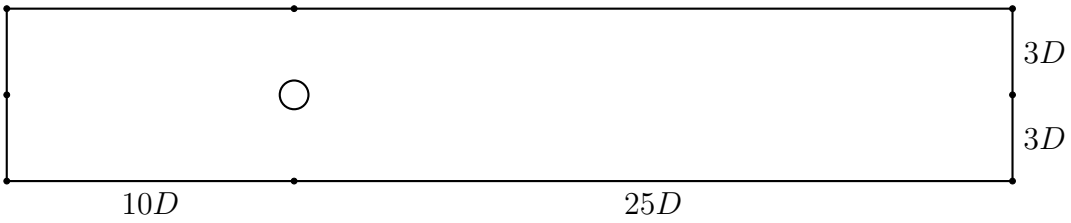

Figure 4.2: **Two-dimension view of the computational domain.**

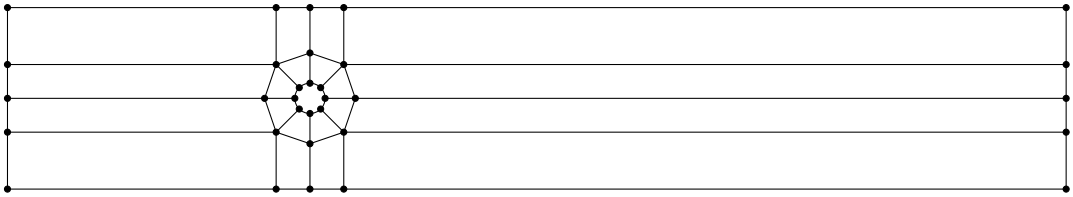

Figure 4.3: **Block subdivision of the computational domain.**

4.1. Mesh generation

Gmsh [23] is used for mesh generation; it is an open source 3D finite element grid generator designed to provide a fast, light and user-friendly meshing tool. `life`^{x} can handle both hexahedral and tetrahedral meshes; for this test case an hexahedral mesh is used. Due to the presence of the curved cylinder surface, an orthogonal mesh is not advisable, as well as an O-grid because both would result in highly skewed and deformed cells at the boundaries. For this reason a block structured approach is preferred. At the same time, defining different blocks allows more flexibility and a more effective refinements: the regions nearby the cylinder are meshed as O-grids and refined in order to better catch the occurrence of cavitation. The same is done for the blocks in the wake of the cylinder, where the grid has to be fine enough to catch the behaviour of the wake. Figure 4.3 shows the different blocks in which the computational domain is divided. To perform 3D simulations, the planar mesh is extruded in the third direction.

In Figure 4.4 some screenshots of the three different meshes are reported. The mesh spacing for the fine grid is $0.008D \times 0.01D$ in the radial and azimuthal directions near the cylinder and stretches to $0.017D \times 0.02D$ at approximately $2D$ downstream and then further stretches to $0.06D \times 0.05D$ at a distance of $5D$ downstream. The coarse grid has a near-wall mesh spacing of $0.03D \times 0.02D$ and stretches to $0.06D \times 0.06D$ at approximately $2D$ downstream. These spacings are comparable to the ones used in the reference work [26]; moreover, mesh convergence analysis has been performed and is described in the following sections.

In Table 4.1 the main features of each grid are reported: the number of the cells of the

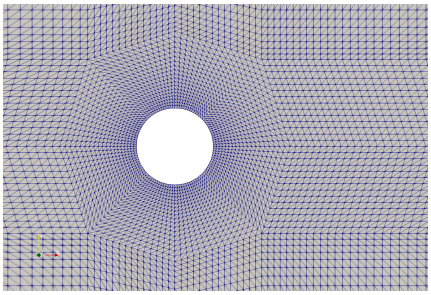

(a) Mesh 1: Coarse grid.

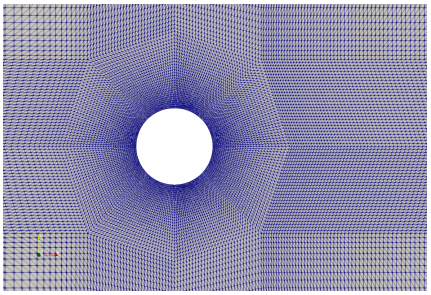

(b) Mesh 2: Medium grid.

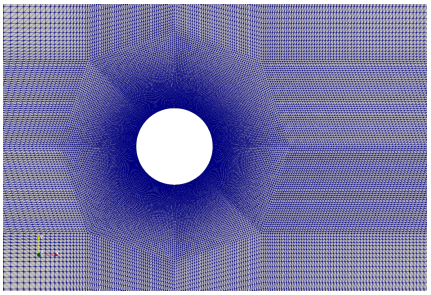

(c) Mesh 3: Fine grid.

Figure 4.4: **Screenshots of the different grids.**

different meshes, the number of active degrees of freedom (DOFs), and the maximum, minumum and mean value of the cell diameters: $h_{\max}$, $h_{\min}$ and h_{mean}.

4.2. Boundary conditions

In this section, we provide boundary conditions for the mixture velocity $\mathbf{u}$, pressure P and vapor fraction α.

As for the vapor fraction α, an homogeneous Dirichlet boundary condition is set at the inlet. This is done because the pressure at the inlet is though to be always greater than the vapor pressure and no cavitation occurs at the inlet. On all the other boundaries, awe impose an homogeneous Neumann boundary condition, meaning that:

$$(\alpha\mathbf{u} - \kappa\nabla\alpha) \cdot \hat{\mathbf{n}} = 0 \qquad \text{on } \Gamma_N \times (0, T] \tag{4.1}$$

We impose a Dirichlet boundary condition for the velocity on the inlet boundary. The velocity is a flat profile, constant in space, but evolving in time through a cosinusoidal ramp function: the final value of the velocity $\mathbf{u}_f$ is reached after some time $t_{\text{load}} = 0.1$s

	Mesh 1	Mesh 2	Mesh 3
Number of cells	10080	27836	57708
Number of velocity DOFs	62088	169860	350124
Number of pressure DOFs	20696	56620	116708
Number of α DOFs	20696	56620	116708
$h_{\mathbf{max}}$	$7.1 \cdot 10^{-2}$ m	$6.5 \cdot 10^{-2}$ m	$5.5 \cdot 10^{-2}$ m
$h_{\mathbf{min}}$	$5.0 \cdot 10^{-3}$ m	$3.3 \cdot 10^{-2}$ m	$2.3 \cdot 10^{-2}$ m
$h_{\mathbf{mean}}$	$2.4 \cdot 10^{-2}$ m	$1.4 \cdot 10^{-2}$ m	$1.0 \cdot 10^{-2}$ m

Table 4.1: **Comparison of the different grids used to perform numerical simulations.**

trough the (4.2) starting from $\mathbf{u}_0 = 0$ at $t_0 = 0$:

$$\mathbf{u}(t) = \begin{cases} \mathbf{u}_0 + (\mathbf{u}_f - \mathbf{u}_0)\frac{1}{2}\Big(1 - \cos\Big(\frac{\pi(t-t_0)}{t_{\text{load}}}\Big)\Big) & t_0 \le t \le t_0 + t_{\text{load}} \\ \mathbf{u}_f & t_0 + t_{\text{load}} \le t \end{cases} \tag{4.2}$$

On the cylinder surface, we impose a no-slip boundary condition, whereas on the channel walls boundaries a zero flux boundary condition is set, imposing $\mathbf{u} \cdot \hat{\mathbf{n}} = 0$.

On the outlet boundary, an homogeneous pressure boundary condition is imposed:

$$\sigma(\mathbf{u}, P)\hat{\mathbf{n}} = -P_{\Gamma_N}\hat{\mathbf{n}} \qquad \text{on } \Gamma_N \times (0, T] \tag{4.3}$$

4.3. Numerical results

In this section we present the numerical results on the different grids described in section 4.1. Simulations were carried out on gigat computing system available at MOX laboratories, using one node with 20 CPUs. The total simulation time, for each simulation, resulted in 4 h 24 min for Mesh 2, and 9 h 48 min for Mesh 3.

This section is divided as follows: first of all the mesh convergence is assessed by comparing the C_L and C_D temporal history resulting from the three different grids, as well as the mean α distribution. Then, a parametric study on the artificial diffusion parameter κ is discussed. Finally the results are presented: first we provide some insights on the time evolution of the flow and then we discuss the peculiar features of the flow such as: the quantity of interest on the cylinder surface, the mean velocity divergence distribution and the unsteady loads on the cylinder.

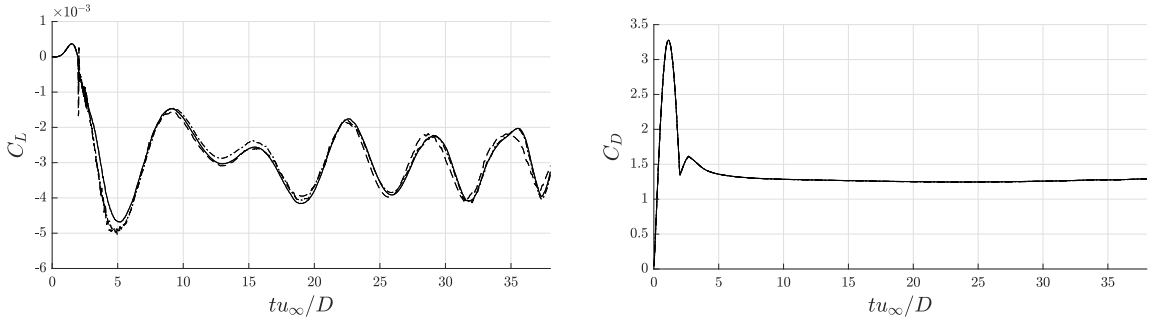

(a) Lift coefficient - C_L. (b) Drag coefficient - C_D.

Figure 4.5: **Comparison of lift (a) and drag (b) coefficient:** - - - coarse mesh (Mesh 1), -·-· medium mesh (Mesh 2), —— fine mesh (Mesh 3).

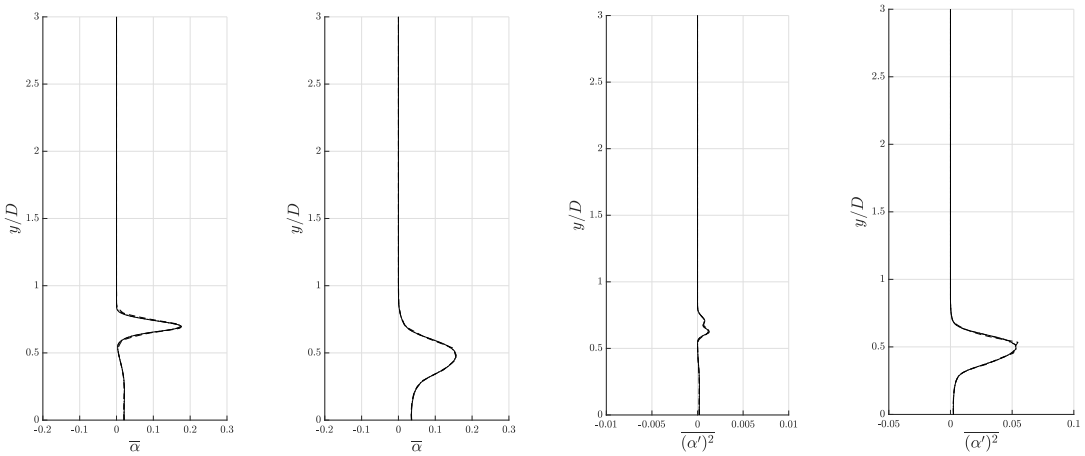

(a) (b) (c) (d)

Figure 4.6: **Comparison of the vapor fraction mean distribution (a,b) and fluctuations (c,d) at $\mathbf{x_1/D = 0.6}$ (a,c) and $\mathbf{x_2/D = 2.0}$ (b,d):** - - - coarse mesh (Mesh 1), -·-· medium mesh (Mesh 2), —— fine mesh (Mesh 3).

4.3.1. Mesh convergence

In Figure 4.5 the temporal evolution of the lift coefficient C_L and the drag coefficient C_D are plotted with respect to the adimesional time $\bar{t} = tu_\infty/D$. The evolution of the velocity ramp is clearly visible in Figure 4.5(b) and ends at $\bar{t} = 2.0$. After a transient, a periodic oscillation is visible in the C_L time history; more comments on the periodic behaviour are provided in section 4.3.6. In Figure 4.6 the α distribution over a vertical line at two different adimensional positions in the wake of the cylinder is plotted : $\bar{x}_1 = x_1/D = 0.6$ and $\bar{x}_2 = x_2/D = 2.0$. Since data are averaged, only half of the domain is considered.

Both Figures 4.5 and 4.6 confirm that mesh convergence is achieved since the results obtained using Mesh 2 and Mesh 3 are almost identical, proving mesh independence.

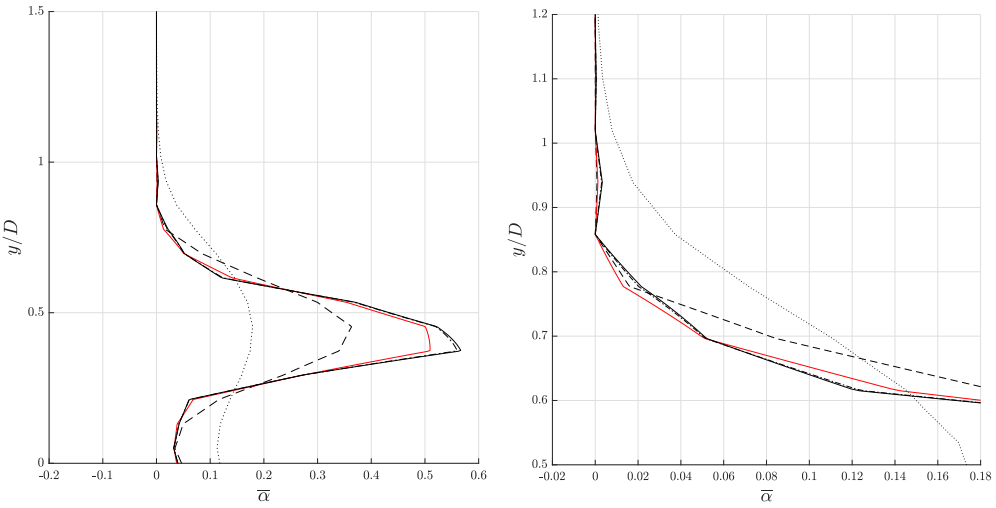

(a) (b) Detail of (a)

Figure 4.7: **Parametric study on the diffusion parameter κ, distribution over a line at x/D = 1.5:** ····· $\kappa = 10^{-2}$, - - - $\kappa = 10^{-3}$, —— $\kappa = 10^{-4}$, -·-·- $\kappa = 10^{-5}$, -··- $\kappa = 10^{-6}$, —— $\kappa = 0.0$,

4.3.2. Parametric study on κ

When presenting the strong formulation of the coupled problem in section 2.3, a diffusion term $(-\kappa\nabla\alpha)$ has been added to the transport equation for α (2.57) to prevent unphysical oscillations across the interfaces with positive and null value of vapor fraction. In this section the influence of the κ parameter is evaluated to understand its effectiveness and to prevent an artificial bias of the solution. In Figure 4.7 the distribution of the mean vapor fraction $\bar{\alpha}$ is plotted over a vertical line located downstream at $x/D = 1.5$ for the different values of diffusion parameter κ. In Figure 4.8 instantaneous of α contours are shown for different values of diffusion parameter κ at $\bar{t} = 8.0$.

Figures 4.7 and 4.8 show that higher values of the diffusion coefficient κ influence the solution, smoothing artificially the α distribution over the line. Smaller values of the parameter k produce similar results starting from $\kappa = 10^{-4}$. However, smaller values of the parameter produce oscillations at the interfaces. This drawback is mitigated by the presence of the SUPG stabilization terms but, starting from $\kappa = 10^{-5}$ some oscillations are visible in Figure 4.7. For this reason, $\kappa = 10^{-4}$ is selected and used in the following. In section 5.3.2 the value of the diffusion coefficient is related to the size of the mesh elements h, we refer to that section for a complete discussion.

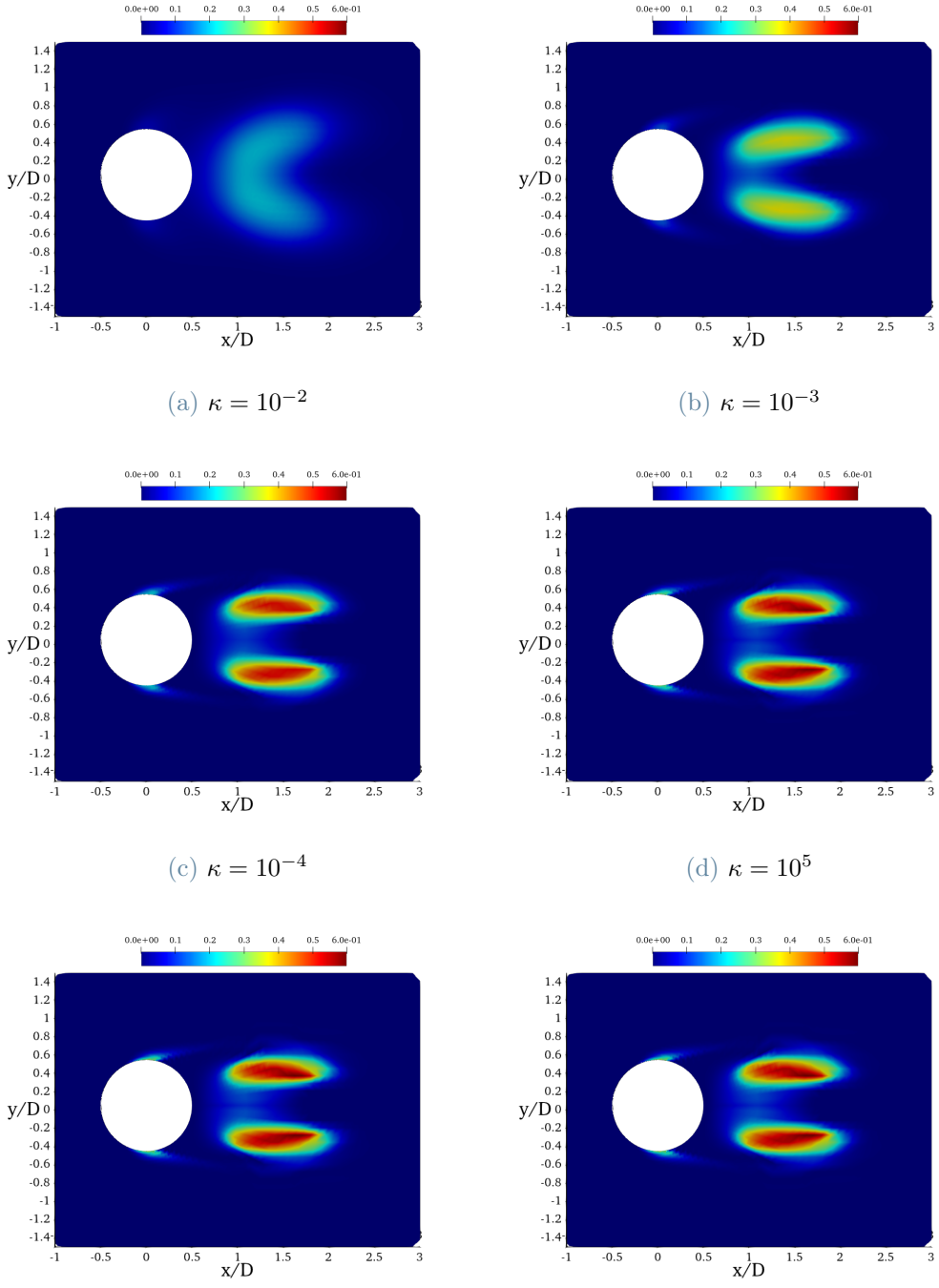

(a) $\kappa = 10^{-2}$ (b) $\kappa = 10^{-3}$

(c) $\kappa = 10^{-4}$ (d) $\kappa = 10^{5}$

(e) $\kappa = 10^{-6}$ (f) $\kappa = 0.0$

Figure 4.8: **Parametric study on the diffusion parameter κ: α contours.** Snapshots at $\bar{t} = 8.0$.

4.3.3. Velocity, pressure and α distribution

In this section the main features of the cavitating flow are analysed. Figures 4.9, 4.10, 4.11 and 4.12 show some snapshots of velocity, pressure and α distribution at different

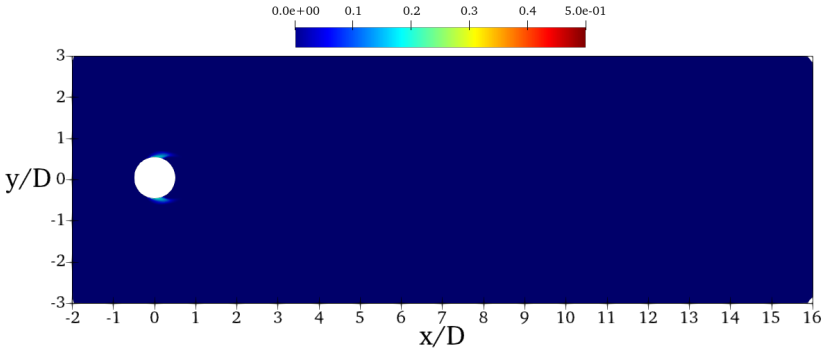

(a) Instantaneous vapor fraction contour.

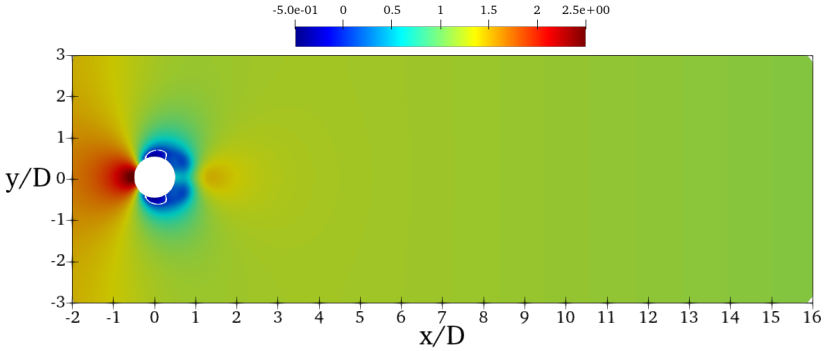

(b) Instantaneous local cavitation number contour.

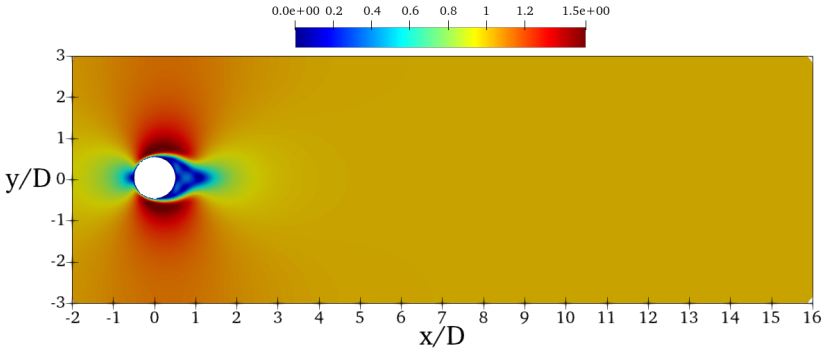

(c) Instantaneous adimensional velocity magnitude contour.

Figure 4.9: **Main features of the cavitating flow: instantaneous snapshot at $\bar{t} = 2.6$.** This snapshot is taken few timesteps after the final value of the inlet velocity is reached at $\bar{t} = 2.0$: the flow on the lower and upper side of the cylinder is accelerated and the pressure drops under the vapor pressure, resulting in cavitation inception. The wake starts to develop as the velocity magnitude plot shows.

instances in a portion of the fluid domain. The pressure is not shown as a dimensional quantity, instead, for each point of the grid the local cavitation number σ_l is computed:

$$\sigma_l = \frac{P_l - P_v}{\frac{1}{2}\rho_l u_\infty^2}. \tag{4.4}$$

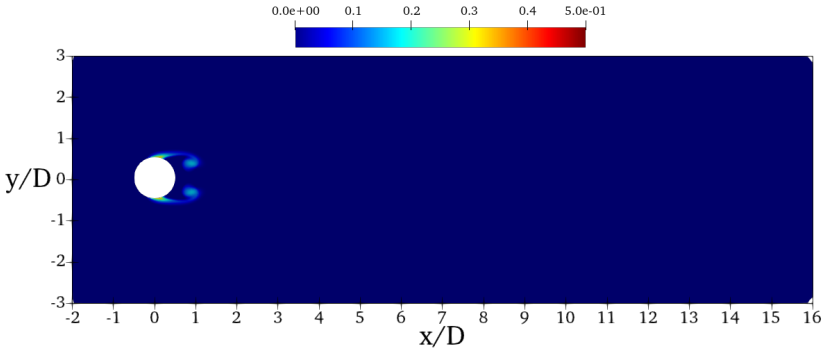

(a) Instantaneous vapor fraction contour.

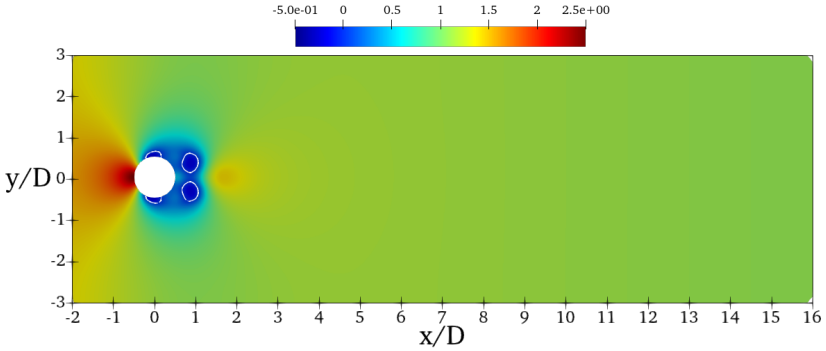

(b) Instantaneous local cavitation number contour.

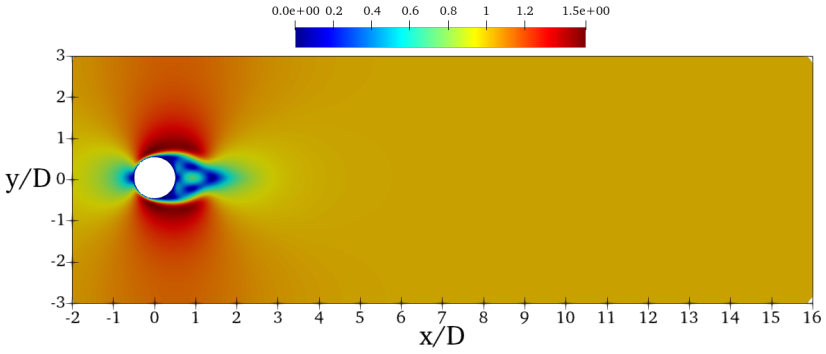

(c) Instantaneous adimensional velocity magnitude contour.

Figure 4.10: **Main features of the cavitating flow: instantaneous snapshot at $\bar{t} = 3.4$.** The pressure on both sides of the cylinder remains below the critical value and this results in an higher value of the vapor fraction. Some vapor fraction is convected by the flow. At the same time two counter rotating vortexes develop in the wake. Pressure in the vortexes cores is lower than the critical value, this results in posivite value of α in the wake.

Above the local cavitation number contours, the line $\sigma_l = 0$ is highlighted: where $\sigma_l < 0$, the net production of vapor fraction is positive, whereas where $\sigma_l > 0$, if some vapor fraction is present, it condensates back to the liquid phase. The velocity magnitude is adimensionalized with respect to the inlet final value $\mathbf{u}_f$. All results in Figures 4.9, 4.10, 4.11 and 4.12 are obtained using the fine grid, Mesh 3.

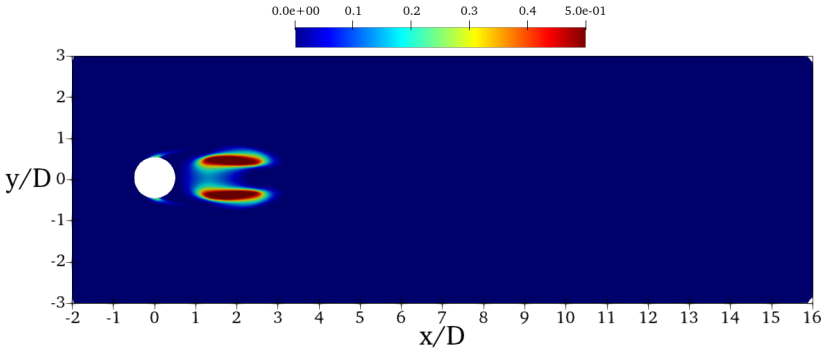

(a) Instantaneous vapor fraction contour.

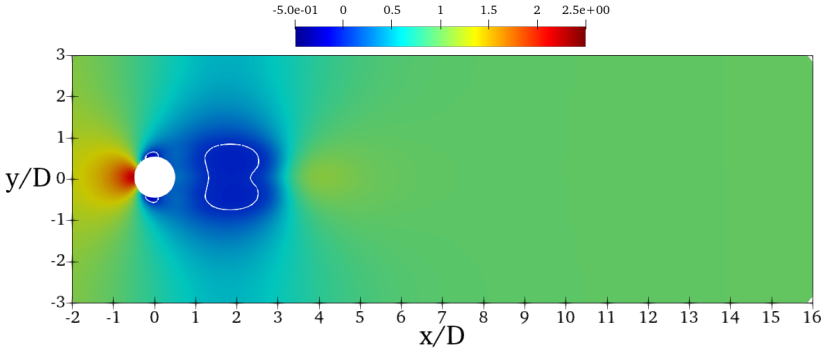

(b) Instantaneous local cavitation number contour.

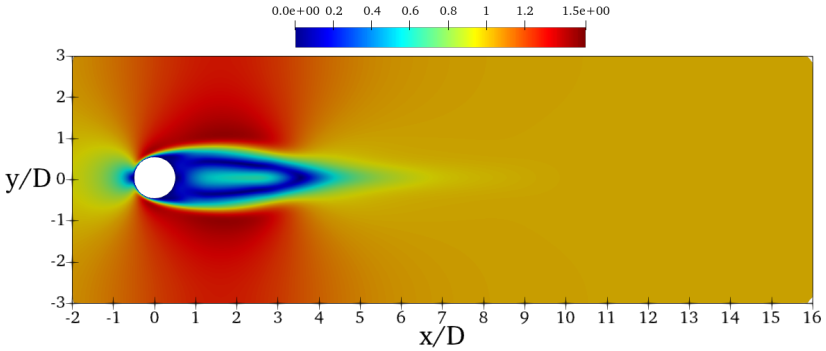

(c) Instantaneous adimensional velocity magnitude contour.

Figure 4.11: **Main features of the cavitating flow: instantaneous snapshot at $\bar{t} = 10$.** The vortexes in the wake interact creating a lower pressure zone and resulting in higher values of α in the cores. The presence of vapor fraction, reduces the local density and viscosity of the fluid, resulting in a more stable wake [26], for this reason the periodic vortex shedding is delayed in time with respect to the non-cavitating flow.

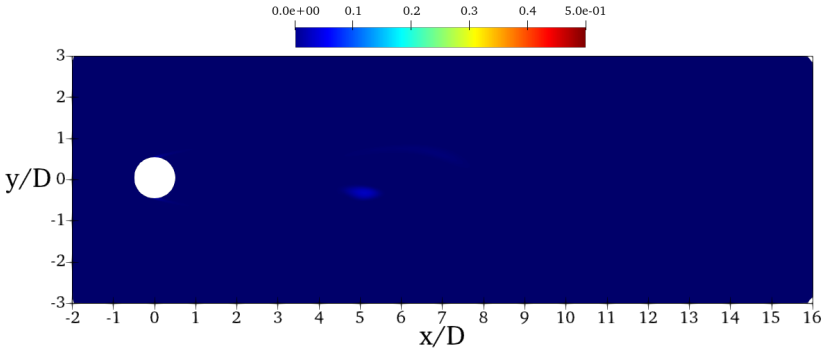

(a) Instantaneous vapor fraction contour.

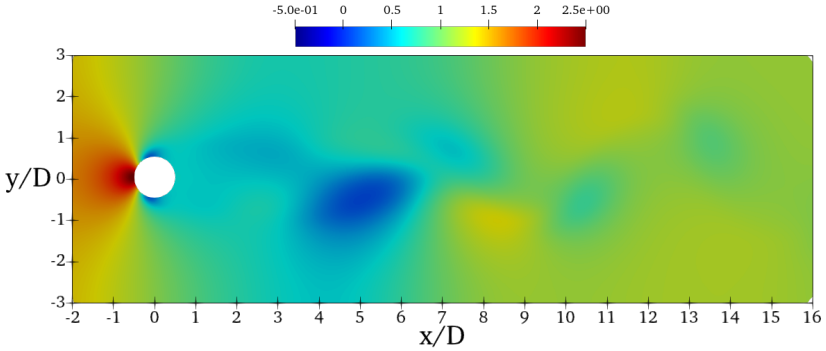

(b) Instantaneous local cavitation number contour.

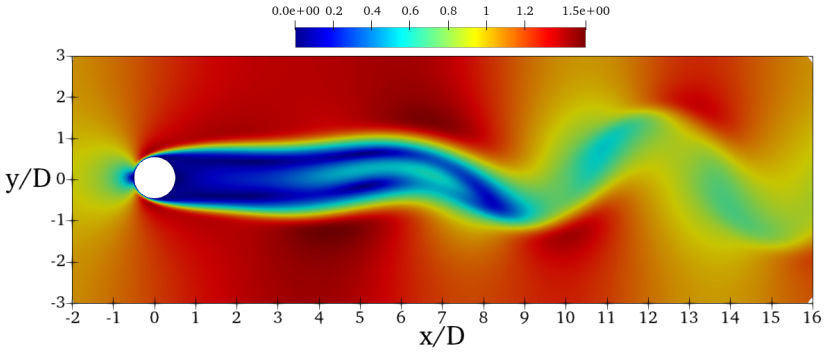

(c) Instantaneous adimensional velocity magnitude contour.

Figure 4.12: **Main features of the cavitating flow: instantaneous snapshot at $\bar{t} = 47$.** Once the flow is fully developed, the typical periodic vortex shedding feature appears. Non zero value of α are still present on the surface of the cylinder and in the vortex cores, even though the pressure recovery in the wake makes the pressure higher than the critical value, inducing the condensation of the vortex cores. The velocity magnitude contour, as well as the frequency of the shedding is modified by cavitation and will be discussed in detail in section 4.3.6.

4.3.4. Quantities of interest on the cylinder surface

In this section the quantities of interest on the cylinder surface are analyzed. The main focus is on the mean distribution of α and the mean pressure coefficient computed over

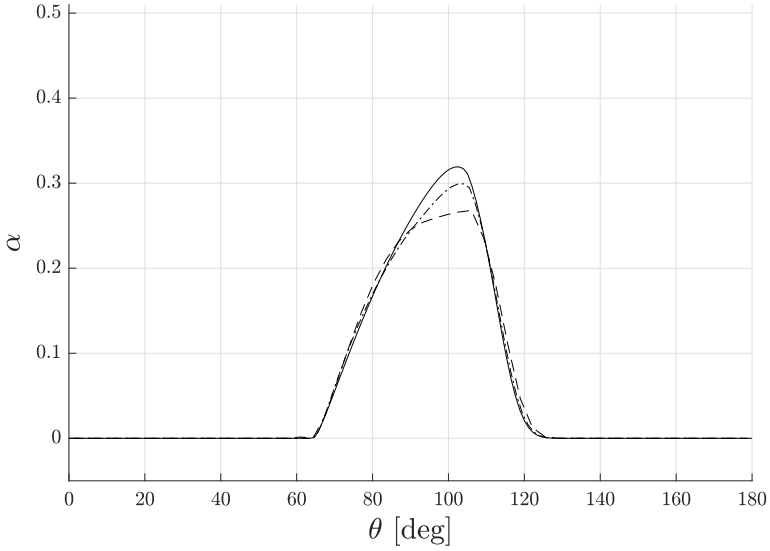

Figure 4.13: **Vapor fraction distribution on the cylinder surface:** - - - coarse mesh (Mesh 1), -·-· medium mesh (Mesh 2), —— fine mesh (Mesh 3). Cavitation bubble is predicted to start at $\theta = 65°$.

one period of oscillation. $\theta = 0°$ corresponds to the stagnation point, whereas $\theta = 180°$ is its diametrical opposite.

Figure 4.13 shows the distribution of the vapor volume fraction over the surface for the three mesh considered at $\mathbb{R}e = 200$ and $\sigma = 1.0$. The vapor bubble inception is predicted to start at $\theta = 65°$. This prediction is in accordance with the results from [26], where cavitation bubbles are predicted to start at $\theta = 60°$.

Figure 4.14, shows the pressure coefficient C_P distribution over the surface of the cylinder at $\mathbb{R}e = 200$, $\sigma = 1.0$ and $\sigma = 2.0$. C_P is computed as following:

$$C_P = \frac{P - P_\infty}{\frac{1}{2}\rho_l u_\infty^2} \tag{4.5}$$

When $\sigma = 2.0$, the outlet pressure is higher enough to avoid cavitation in all the domain. The C_P starts from $C_P = 1.0$ at the stagnation point, then pressure decays to its minimum value at approximately 80° as the flow accelerates from the stagnation point, then increases as the flow decelerates, prior to becoming approximately constant in the wake region at the trailing edge. Cavitation is seen to decrease the magnitude of minimum C_P magnitude, as shown in Figure 4.14. This result is in accordance with the available literature data and can be motivated as following: once flow cavitates (close to the minimum C_P location), the pressure in the vapour region remains close to the P_v, it does not further decrease with fluid acceleration. The upstream flow therefore sees lower values of favourable pressure gradient and the downstream flow experiences approximately constant pressure.

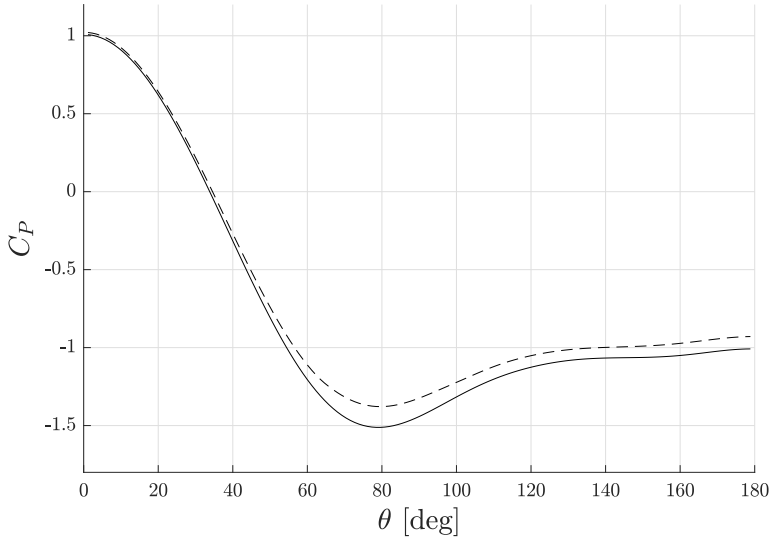

Figure 4.14: **Pressure coefficient distribution on the cylinder surface:** —— $\sigma = 2.0$, - - - $\sigma = 1.0$. Cavitation decreases the magnitude of the minimum C_P and results in an higher pressure recovery on the cylinder surface.

4.3.5. Divergence of the velocity field

Cavitation causes density change, which implies a considerable change in the divergence of the velocity field. Figure 4.15 shows the mean velocity divergence $\nabla \cdot \mathbf{u}$ contours when $\sigma = 1.0$. The divergence is properly normalized trough the diameter D and the inlet velocity u_∞. Expansion caused due to cavitation produces positive velocity divergence and, as the flow cavitates more, the region of positive divergence also increases due to the increased amount of vapor. It is interesting to note a compression region (negative divergence) downstream of the expansion region. This region is an indication of some amount of vapour being converted back to liquid due to the pressure recovery. This comment is in accordance with the distribution of α on the cylinder surface plotted in Figure 4.13, where starting from $\theta \approx 100°$, the value of vapor fraction decreases.

The mean velocity divergence contour from [26] is reported for a direct comparison.

4.3.6. Unsteady loads on the cylinder

In section 4.3.3,velocity distribution at different instances have been discussed: Figure 4.12 provides the pressure and velocity contours when the flow is fully developed, showing the typical vortex shedding behaviour. In this section the unsteady loads on the cylinder are analysed through the Strouhal number, investigating how cavitation affects the frequency of this periodic phenomenon. The power spectrum of the lift time history for both the non-cavitating ($\sigma = 2.0$) and the cavitating ($\sigma = 1.0$) case is computed and plotted in

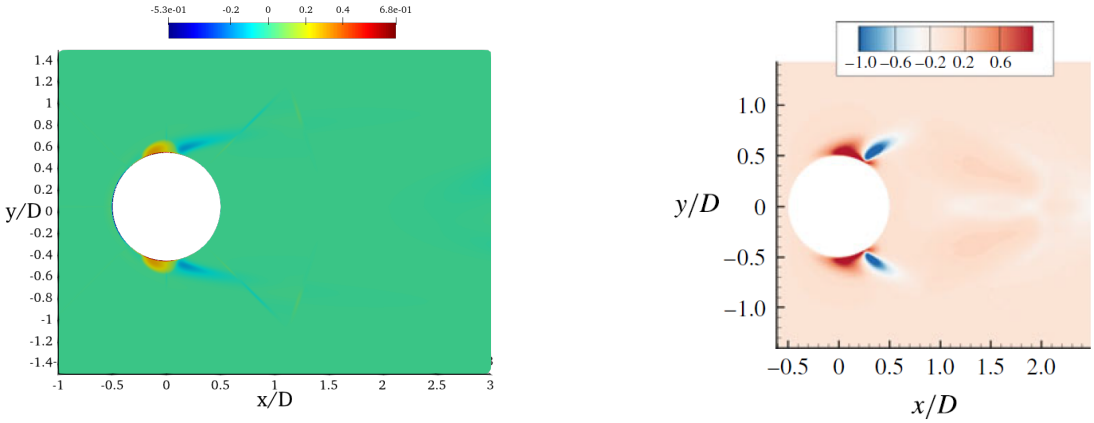

(a) Mean velocity divergence.

(b) Mean velocity divergence from [26].

Figure 4.15: **Mean velocity divergence contour:** $\mathbb{R}e = 200$, $\sigma = 1.0$. Positive values of velocity divergence correspond to evaporation zones; negative values of divergence are instead due to some vapor condensing back to the liquid phase.

Figure 4.16 as function of the Strouhal number $\mathbb{S}t = fD/u_\infty$. The vortexes shed from the cylinder are responsible for the primary peaks in the power spectrum, thus the value of the Strouhal number is obtained identifying the primary peaks of the lift history power spectrum.

The Strouhal number for the non-cavitating flow is $\mathbb{S}t_{\sigma=2} = 0.171$; this result is in agreement with the work by [35] where the Strouhal number has been computed for a wide range of Reynolds numbers. In the cavitating case the Strouhal number is reduced to $\mathbb{S}t_{\sigma=1} = 0.153$, resulting in an 11% decrease of the frequency. This reduction of the frequency vortex shedding is a phenomenon observed also in [26], where the Strouhal number is decreased by 19% when $\sigma = 1.0$. Thus, decreasing cavitation number has an important side effect on the unsteady loads: vapor bubbles induce a reduction of the frequency of oscillation, pointing to a more steady behaviour near the cylinder.

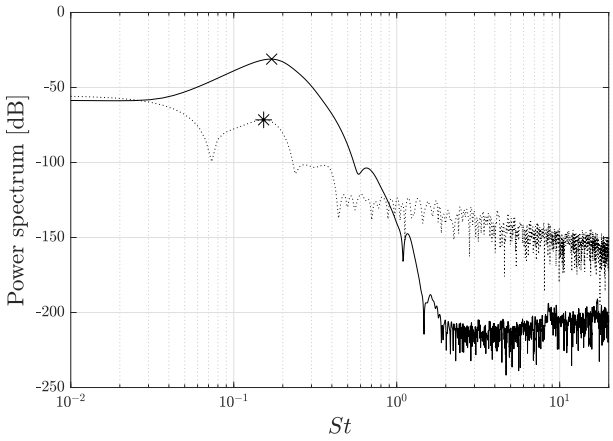

Figure 4.16: **Unsteady loads on the cylinder - Power Spectrum:** —— non-cavitating case ($\sigma = 2.0$), ····· cavitating case ($\sigma = 1.0$), $\times\ \mathbb{S}t_{\sigma=2.0} = 0.171$, $*\ \mathbb{S}t_{\sigma=1.0} = 0.153$. The Strouhal number associated to vortex shedding is identified as the primary peak of the power spectrum. In the cavitating case the shedding frequency is reduced due to the presence of the vapor bubbles.

5 | Numerical simulation of the FDA nozzle benchmark

In this chapter, the numerical results obtained on the nozzle FDA geometry are presented. This benchmark has been proposed by the U.S. Food and Drug Administration (FDA) to bridge the lack of biological benchmarks to validate CFD simulations applied to complex human anatomy and physiology. In [48], two hemodynamics benchmarks are proposed: a nozzle model and a blood pump model. In this chapter we consider the nozzle model because it is representative of the closing valves Venturi-type geometry. In literature only non-cavitating cases have been investigated; for this reason only results without cavitation will be compared to literature results, whereas the cavitating case will be analyzed with respect to the non-cavitating one.

The nozzle model benchmark is represented in Figure 5.1 and consists of an axisymmetric geometry composed of a 0.012 m diameter cylindrical inlet, a 20° conical nozzle, a 0.004 m diameter throat and a 0.012 m diameter cylindrical expansion region. The flow is accelerated progressively in the conical section, then it encounters a sudden expansion after the end of the throat. Shear layers and recirculating flows are expected. The length of the inlet and the outlet channels are set respectively to 0.120 m and 0.144 m to avoid the influence of the boundary at the throat as suggested in [54].

We use the same values for density and viscosity described in Chapter 4 for both the liquid and vapor phase; thus the density and viscosity ratios R_ρ and R_μ have the same values as in the cylinder benchmark. The same is done for the constants F_{vap} and F_{cond}.

The Reynolds number, following what is done in [48] and [84], is defined using the throat diameter and the mean velocity $\bar{u}_{z,t}$ in the throat:

$$\mathbb{R}e = \frac{\rho_l \bar{u}_{z,t} D_t}{\mu_l} = \frac{4}{\pi} \frac{Q}{D_t} \frac{\rho_l}{\mu_l}. \tag{5.1}$$

In the above expression, Q is the volumetric flow rate. In the following we impose a volumetric flow rate $Q = 5.2026 \cdot 10^{-6}$ m^3/s at the inlet, resulting in $\mathbb{R}e = 500$.

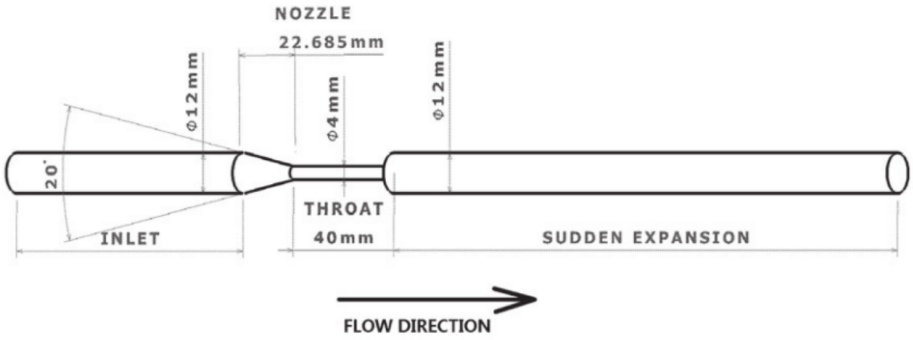

Figure 5.1: **FDA nozzle model benchmark geometry.** Taken from [84].

The cavitation number σ, for the present benchmark is computed as follows:

$$\sigma = \frac{P - P_v}{\frac{1}{2}\rho_l u^2} = \frac{P - P_v}{\frac{1}{2}\rho_l \left(\frac{4Q}{\pi D^2}\right)^2}. \tag{5.2}$$

The outlet pressure is considered as the reference pressure; as for the reference velocity, both the inlet mean velocity and the throat mean velocity are considered; the resulting values for the cavitation numbers are:

$$\sigma_{\text{inlet}} = 18.90, \tag{5.3}$$

$$\sigma_{\text{throat}} = 0.23. \tag{5.4}$$

5.1. Mesh generation

The mesh is generated using Gmsh [23]. An OH-grid topology is adopted in order to properly mesh the circular domain. The nozzle is divided into five different subdomains: a central square block with H-grid topology and four external regions with an O-grid topology; Figure 5.2 shows the 2D topology of the mesh. The mesh is then extruded in order to model the whole 3D nozzle domain as shown in Figure 5.3.

We considered two different meshes: a coarse mesh (Mesh 1) and a finer mesh (Mesh 2). In Mesh 2, the mesh spacing along the longitudinal direction is $0.25D_t$, whereas along the radial direction the mesh element size is $0.04D_t$, where D_t is the diameter of the throat section. In Table 5.1 the main features of each grid are reported: the number of the cells of the different meshes, the number of active degrees of freedom (DOFs), and the maximum, minumum and mean value of the cell diameters: $h_{\max}$, $h_{\min}$ and h_{mean}.

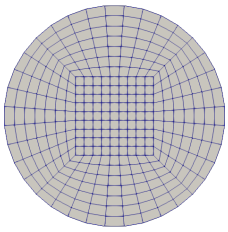

Figure 5.2: **FDA nozzle model 2D topology.** The center of the domain is meshed using an H-grid topology; the four external regions are meshed with an O-grid topology.

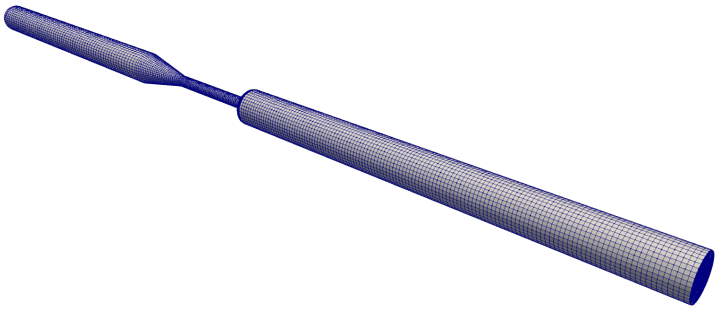

Figure 5.3: **FDA nozzle benchmark 3D mesh.** The 2D surface is extruded to the final 3D mesh.

	Mesh 1	**Mesh 2**
Number of cells	36128	217287
Number of velocity DOFs	116442	670704
Number of pressure DOFs	38814	223568
Number of α DOFs	38814	223568
$h_{\mathbf{max}}$	$4.1 \cdot 10^{-3}$ m	$2.3 \cdot 10^{-3}$ m
$h_{\mathbf{min}}$	$1.2 \cdot 10^{-3}$ m	$9.2 \cdot 10^{-4}$ m
$h_{\mathbf{mean}}$	$3.1 \cdot 10^{-3}$ m	$1.3 \cdot 10^{-3}$ m

Table 5.1: **Comparison of the different grids used to perform numerical simulations.**

5.2. Boundary conditions

In this section, we provide boundary conditions for the mixture velocity $\mathbf{u}$, pressure P and vapor fraction α. As for the vapor fraction, an homogeneous Dirichlet boundary

condition is set at the inlet, and an homogeneous Neumann boundary condition is set at the outlet and on the FDA nozzle walls. In this set of simulations the non-conservative formulation of the transport equation is used; this means that Neumann homogeneous boundary condition reduces to null gradient of the vapor fraction on the outlet boundary.

As for the mixture velocity, a no-slip boundary condition is set on the FDA nozzle walls; on the outlet boundary a pressure boundary condition is set, whereas two different time evolving Dirichlet boundary conditions for velocity are considered at the inlet:

- the first is a time evolving ramp, which follows the expression provided in equation (4.2). The solution starts from still fluid and evolves towards a steady state where $Q = 5.2026 \cdot 10^{-6}$ m^3/s;
- the second is a pulsatile condition, which is intended to model the heart periodic behaviour. The flow Q has the following evolution in time:

$$Q(t) = Q_{\min} + (Q_{\max} - Q_{\min})\frac{1}{2}\Big(1 - \cos\Big(\frac{2\pi t}{T}\Big)\Big) \tag{5.5}$$

  corresponding to a sinusoidal oscillation between $Q_{\min} = 0$ and $Q_{\max} = 5.2026 \cdot 10^{-6}$ m^3/s with a period T. The periodicity of the flow rate profile is $T = 0.6475$s, corresponding to a cardiac cycle of about 92 beats per minute.

The space velocity profile distribution at the inlet is parabolic, resembling a Poiseuille velocity profile, since for the Reynolds number considered ($Re = 500$) the flow at the inlet is laminar:

$$\mathbf{u}(\mathbf{x}, t) = \frac{2Q(t)}{\pi(D/2)^2}\Big(1 - \frac{r^2(\mathbf{x})}{(D/2)^2}\Big). \tag{5.6}$$

5.3. Numerical results

In this section we present the numerical results on the different grids described in section 5.1. Simulations were carried out on gigat computing system available at MOX laboratories, using one node with 32 CPUs. The total simulation time, for each simulation, resulted in 2 h 10 min for Mesh 1, and 20 h 36 min for Mesh 2.

This section is divided as follows: we first present the grid convergence analysis, comparing the results obtained with the coarse and the fine mesh both in the non-cavitating and cavitating case; then we provide some additional comments on the choice of the diffusion parameter κ. In the subsequent sections, the results of the cavitating flows are presented, with a specific focus on the shear stresses distribution.

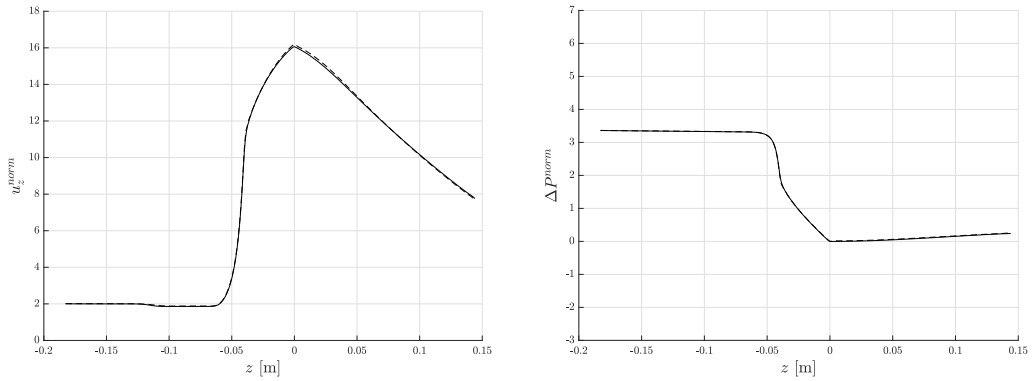

(a) Normalized axial velocity profile. (b) Normalized pressure profile.

Figure 5.4: **Plot of the normalised velocity and pressure along the centerline. Results from the coarse and fine grid are compared for mesh convergence:** —— fine mesh, - - - coarse mesh.

5.3.1. Grid convergence

In order to assess grid convergence, Figure 5.4 shows the distribution of the normalized axial velocity and pressure profile along the centerline of the FDA nozzle geometry.

Velocity and pressure are normalized as follows [55]:

$$\mathbf{u}^{\text{norm}} = \frac{\mathbf{u}}{\bar{u}_{\text{inlet}}}, \tag{5.7}$$

$$\Delta P^{\text{norm}} = \frac{P - P_{z=0}}{1/2\rho_l \bar{u}_t^2}, \tag{5.8}$$

where $\bar{u}_{\text{inlet}} = \frac{Q}{\pi(D_{\text{inlet}}/2)^2}$, $\bar{u}_t$ is the mean velocity in the throat and $P_{z=0}$ is the pressure in $z = 0$, where the throat ends. Figure 5.4 shows that results coming from the coarse and finer mesh are very similar, meaning that the mesh is fine enough to properly model the centerline behaviour.

Figure 5.5, shows the profiles of vapor volume fraction along different lines at a fixed axial position and in a specific time instance. Figure 5.6 sketches the lines considered. The values of vapor fraction α predicted by the coarse mesh and the fine mesh are similar in the center of the domain, where both the meshes are finer. On the contrary near the walls of the FDA nozzle geometry the values of α are not predicted accurately by the coarse mesh, especially in the sudden expansion region near the end of the throat.

To validate the non-cavitating case, the centerline profiles of the normalised velocity and pressure are reported in Figure 5.7. The results obtained match the literature results confirming that the case setup matches with the available results.

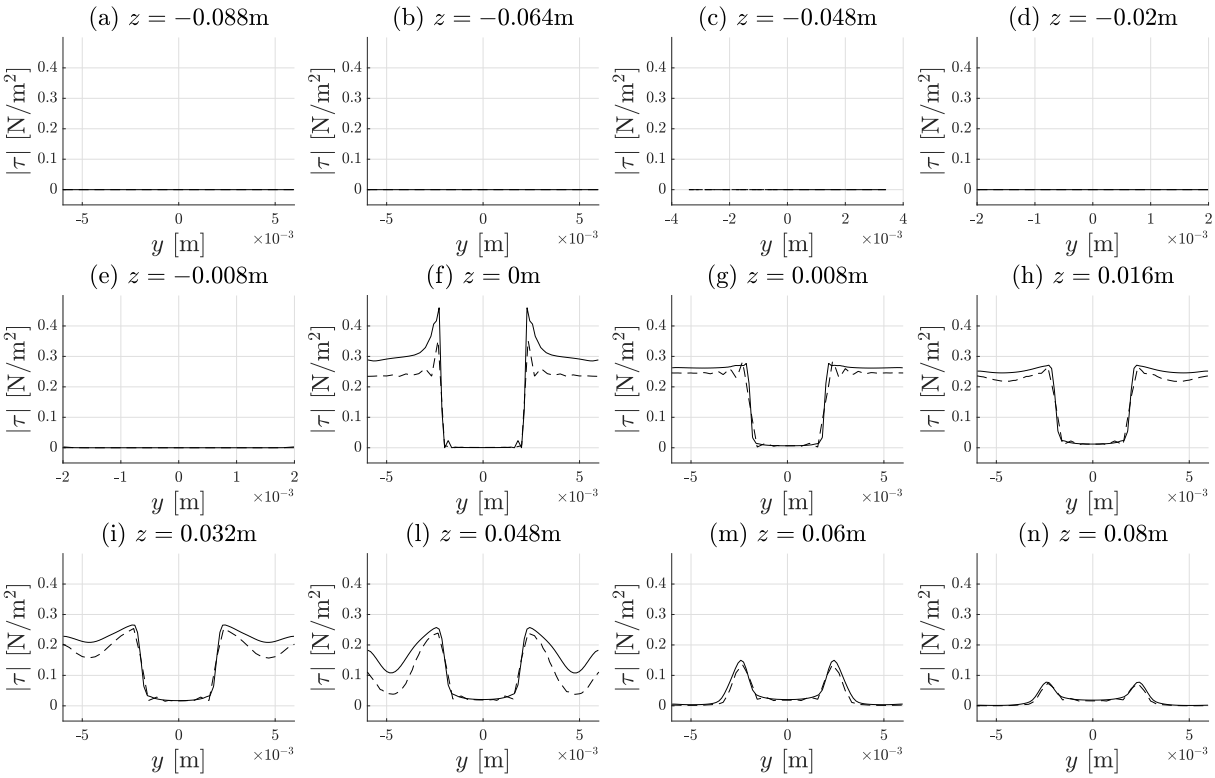

Figure 5.5: **Plot of the vapor fraction distribution along different axial positions. Results from the coarse and fine grid are compared for mesh convergence:** —— fine mesh, - - - coarse mesh. The axial positions are sketched in Figure 5.6. Near the center the coarse mesh predicts well the values of α; near the walls results are different in the expansion region. Results are at $\bar{t} = 12.95$; time is normalised through D_t and $\bar{u}_t$.

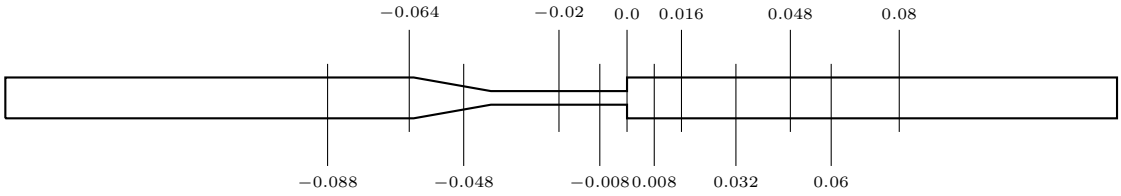

Figure 5.6: **Axial coordinates of the extracted data**. Dimensions are in meters.

5.3.2. Parametric study on κ

Following the procedure proposed in section 4.3.2, a parametric study on the diffusion parameter κ is performed in order to avoid excessive diffusion and, at the same time, prevent the solution from numerical instabilities. The study is performed on the fine grid imposing an inlet velocity ramp.

Different values for the diffusion parameter κ have been tested: $\kappa = 10^{-4}, 10^{-6}, 10^{-7}, 10^{-8}$.

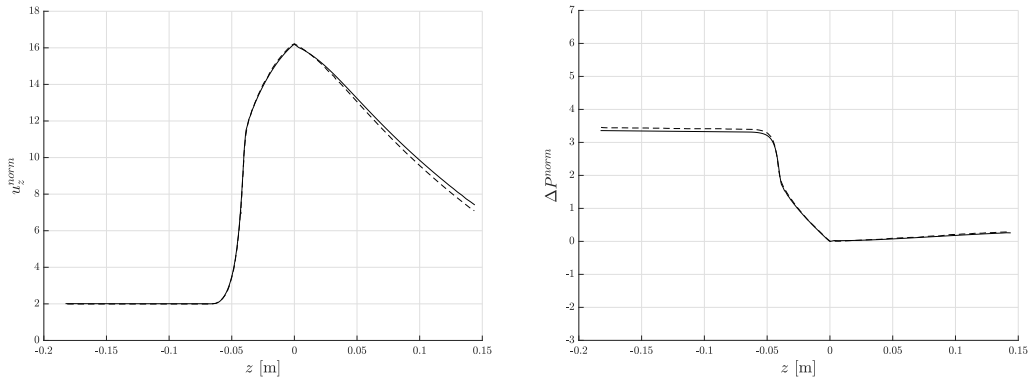

(a) Normalized axial velocity profile. (b) Normalized pressure profile.

Figure 5.7: **Non-cavitating normalised velocity and pressure along the centerline, compared to literature results.** —— coarse mesh numerical result, ····· literature results [55]. The profiles of the normalised velocity and pressure along the centerline of the geometry match the literature results.

Numerical instabilities arise for $k < 10^{-7}$ whereas when $\kappa = 10^{-4}$ diffusion dominates the solution. Thus, $k = 10^{-7}$ is chosen for the fine grid of the present geometry.

The two parametric studies performed in this section and in section 4.3.2, allow to provide meaningful indications upon the right κ value to use. Stabilization parameters have proven to be related to the local mesh size: Forti et al. [19] propose to choose stabilization parameters proportional to h^2, where h is the local mesh characteristic size. We propose to choose k proportional to the maximum cell diameter of the mesh: in the cavitating cylinder case the maximum cell diameter is $h_{\max} = 5.5 \cdot 10^{-2}$ m and $\kappa = 10^{-4}$ is used; in the FDA nozzle benchmark, the maximum cell diameter is $h_{\max} = 2.3 \cdot 10^{-3}$ m and $\kappa = 10^{-7}$, in both cases $\kappa \approx \frac{1}{10} h^2$. This result is consistent with [19] and will be used in the following chapter when testing a complex geometry resembling a MHV.

5.3.3. Numerical results in the case of an inlet velocity ramp

In this section we present the main flow features resulting from a transient simulation in the case of an inlet velocity ramp, as described in section 5.2. Time is normalized with respect to the throat diameter D_t and the mean flow velocity in the throat $\bar{u}_t$. The ramp reaches its maximum value at $\bar{t}_{\text{ramp}} = 0.25$. We first present the velocity, pressure and α distribution at different instances, we then focus on the divergence of velocity field and on the shear stresses

Figures 5.8-5.13 show some snapshots of the main quantities describing the flow at different instances in a portion of the fluid domain. The pressure is not shown as a dimensional quantity, instead, for each point of the grid the local cavitation number $\sigma_{l,t}$ is computed

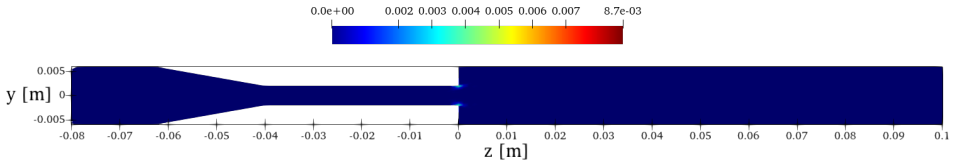

(a) Instantaneous vapor fraction contour.

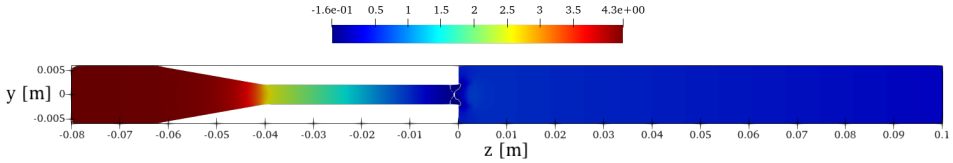

(b) Instantaneous local cavitation number contour.

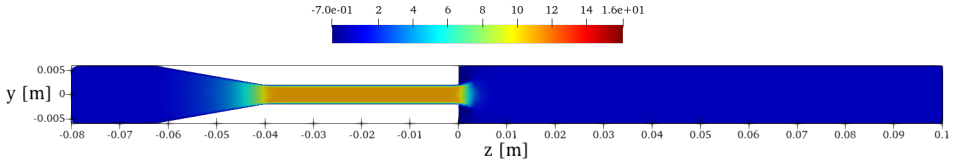

(c) Instantaneous adimensional velocity magnitude contour.

Figure 5.8: **Main features of the cavitating flow: instantaneous snapshot at $\bar{t} = 0.39$.** The impulsive start of the flow produces local negative cavitation numbers near the edges of the expansion region. This induces the mixture to cavitate. The velocity of the jet is higher in the throat; more timespteps are needed to reach the maximum value of velocity in the throat.

using the mean throat velocity $\bar{u}_t$. Above the local cavitation number contours, the line $\sigma_l = 0$ is highlighted. The velocity magnitude is adimensionalized with respect to the inlet mean velocity value $\bar{u}_{\text{inlet}}$. All results are obtained using the fine grid.

The impulsive start of the flow generates two vortexes at the edges of the expansion region, these are convected downstream by the jet and condenstate. When the jet reaches the regime velocity, the shear between the jet and the still fluid induces low pressures and the mixture cavitates near the jet front. At the same time when the jet reaches the maximum velocity, pressure near the edges of the expansion region is low enough to induce cavitation. Recirculation produces an accumulation of α until the steady configuration is reached. We refer to the Figure's captions for a more detailed description of the the flow. Figures 5.14, 5.15 and 5.16 also show some tridimensional views of the α contour.

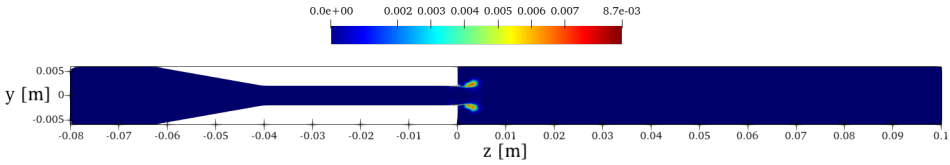

(a) Instantaneous vapor fraction contour.

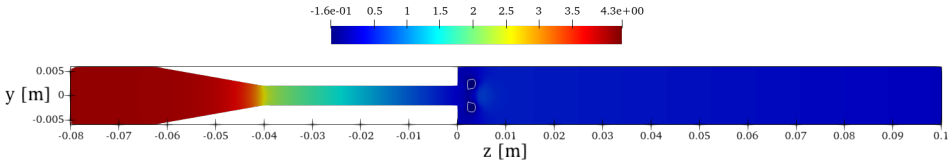

(b) Instantaneous local cavitation number contour.

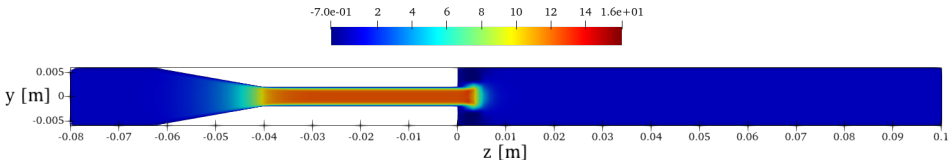

(c) Instantaneous adimensional velocity magnitude contour.

Figure 5.9: **Main features of the cavitating flow: instantaneous snapshot at $\bar{t} = 0.78$.** The vortex cores are convected away from the edge; the mixture velocity in the throat grows and the jet develops in the expansion region.

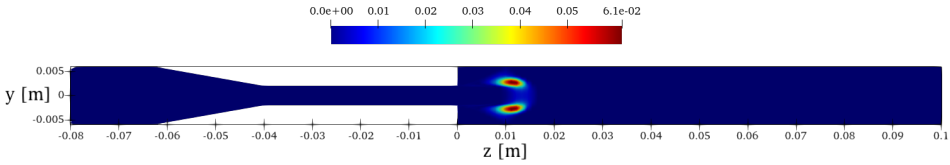

(a) Instantaneous vapor fraction contour.

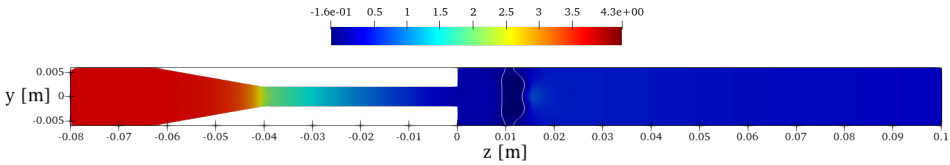

(b) Instantaneous local cavitation number contour.

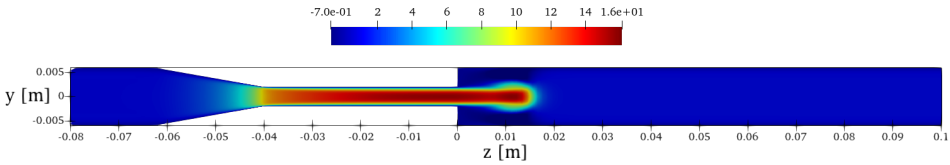

(c) Instantaneous adimensional velocity magnitude contour.

Figure 5.10: **Main features of the cavitating flow: instantaneous snapshot at $\bar{t} = 1.94$.** The cavitation bubbles produced due to the impulsive start condensates. At the same time the velocity of the jet starts saturating. The shear between the jet front and the sorrounding still fluid produces low pressure zones which induce the fluid to cavitate.

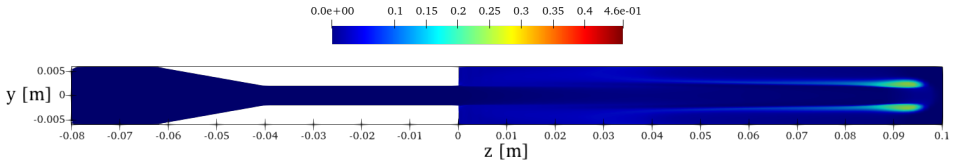

(a) Instantaneous vapor fraction contour.

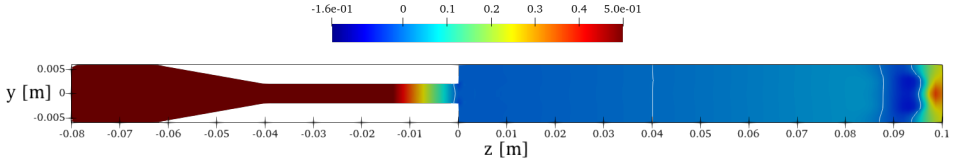

(b) Instantaneous local cavitation number contour.

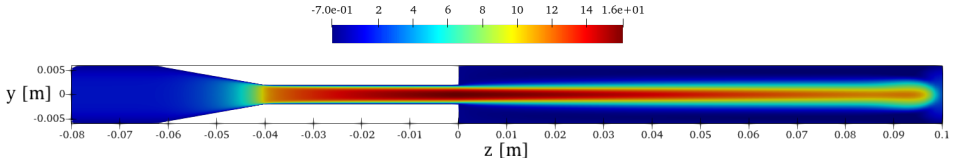

(c) Instantaneous adimensional velocity magnitude contour.

Figure 5.11: **Main features of the cavitating flow: instantaneous snapshot at $\bar{t} = 10.36$.** The jet is almost fully developed. Recirculating vortexes appear besides the jet and allows for an accumulation of vapor fraction α. At the same time pressure is close to the vapor pressure in a big portion of the domain. (Note that due to visualization issues the scale of the quantities is changed.)

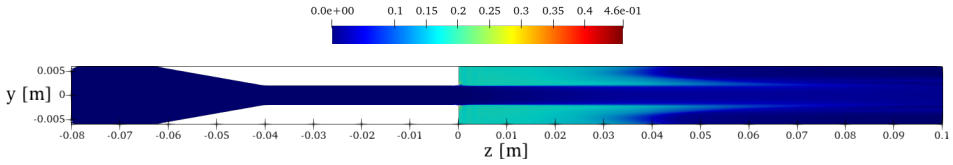

(a) Instantaneous vapor fraction contour.

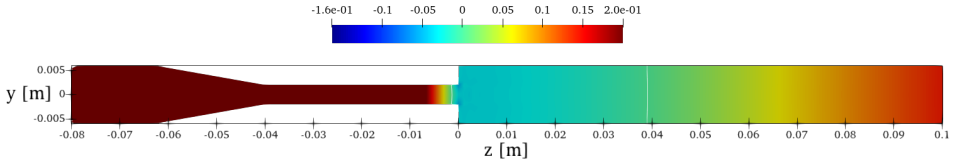

(b) Instantaneous local cavitation number contour.

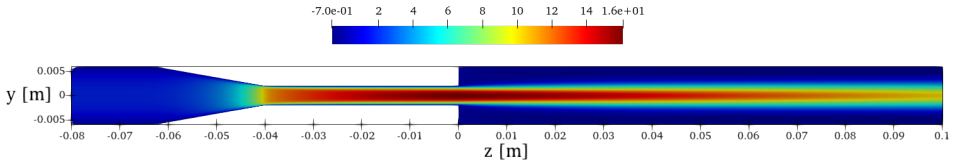

(c) Instantaneous adimensional velocity magnitude contour.

Figure 5.12: **Main features of the cavitating flow: instantaneous snapshot at $\bar{t} = 18.13$.** The jet is fully developed and velocity has reached its maximum value. The edges at the end of the throat induce a low pressure region where there is a positive production of vapor fraction α. Gaseous bubbles accumulate in the region near the edges due to the recirculating flows surrounding the jet.

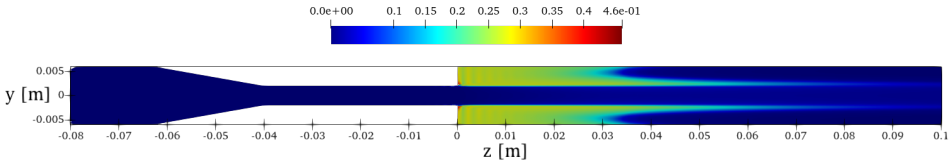

(a) Instantaneous vapor fraction contour.

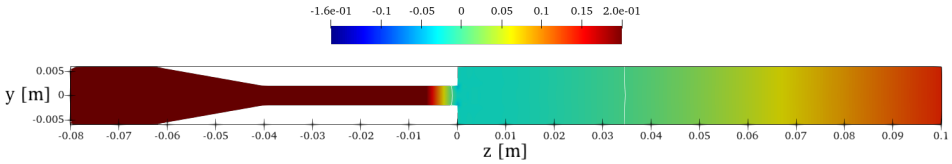

(b) Instantaneous local cavitation number contour.

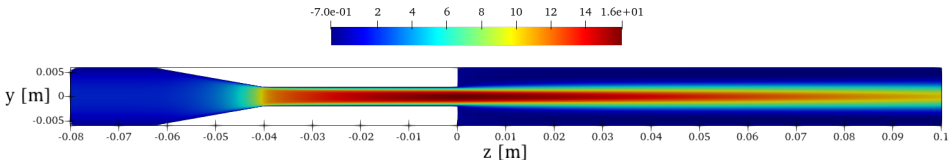

(c) Instantaneous adimensional velocity magnitude contour.

Figure 5.13: **Main features of the cavitating flow: instantaneous snapshot at $\bar{t} = 25$.** Steady state is reached as $\bar{t} = 10 \cdot \bar{t}_{\text{ramp}}$ and the α distribution reaches an equilibrium between the cavitation produced at the edge of the geometry and the condensating vapor fraction downstream.

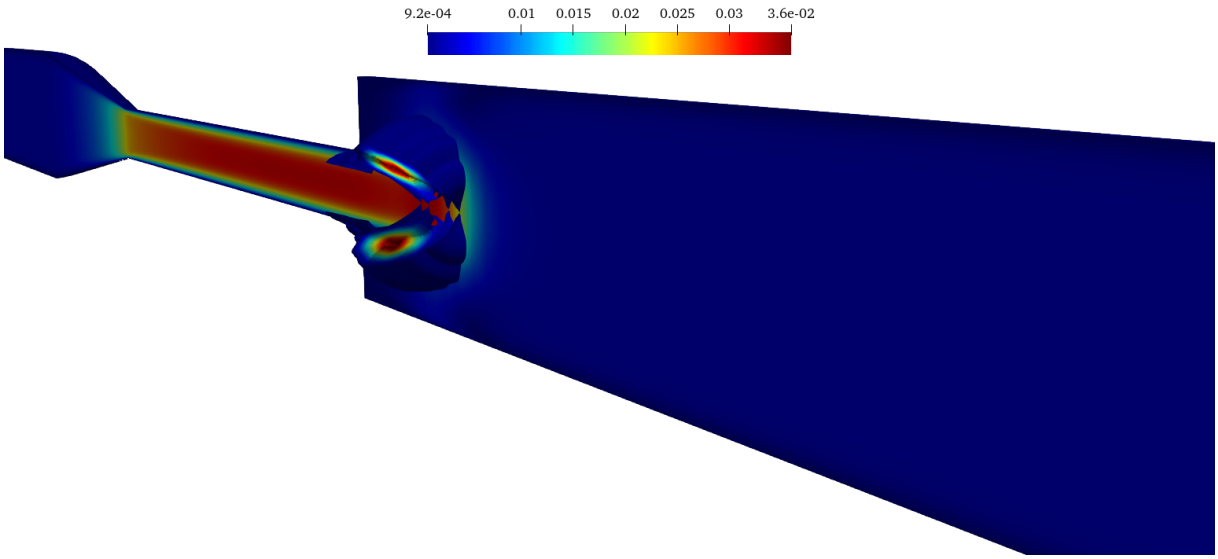

Figure 5.14: **Tridimensional view of the vapor fraction α contour at $\bar{t} = 1.43$.** The jet enters the sudden expansion region and cavitation arises due to the pressure drop near the jet front. In the background the axial velocity contour is reported.

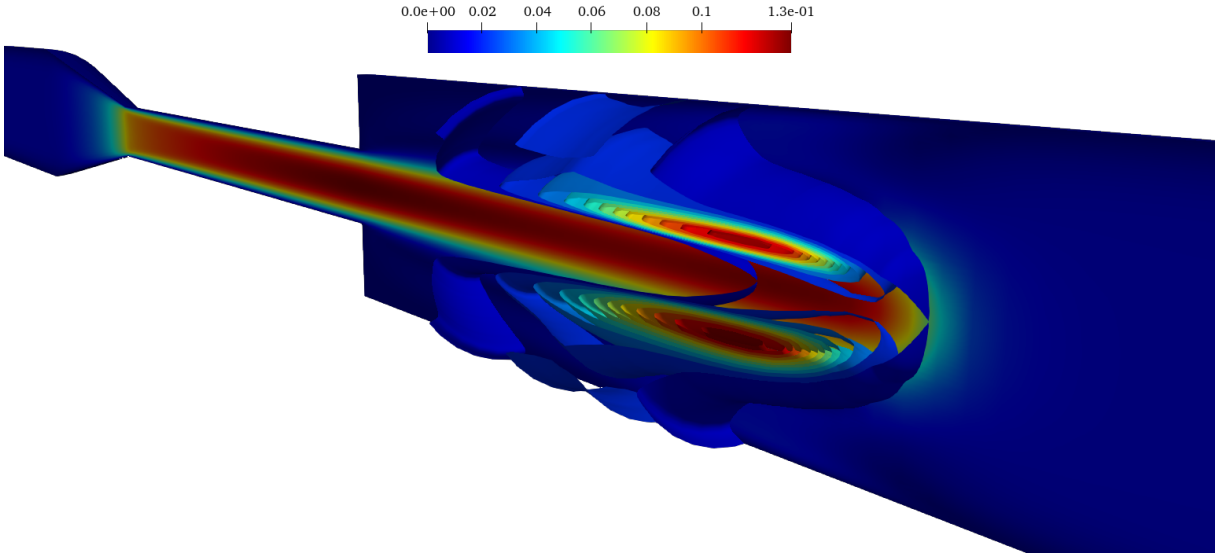

Figure 5.15: **Tridimensional view of the vapor fraction α contour at $\bar{t} = 4.0$.** The jet is fully developed: cavitation bubbles are created and transported downstream by the jet front. In the background the axial velocity contour is reported.

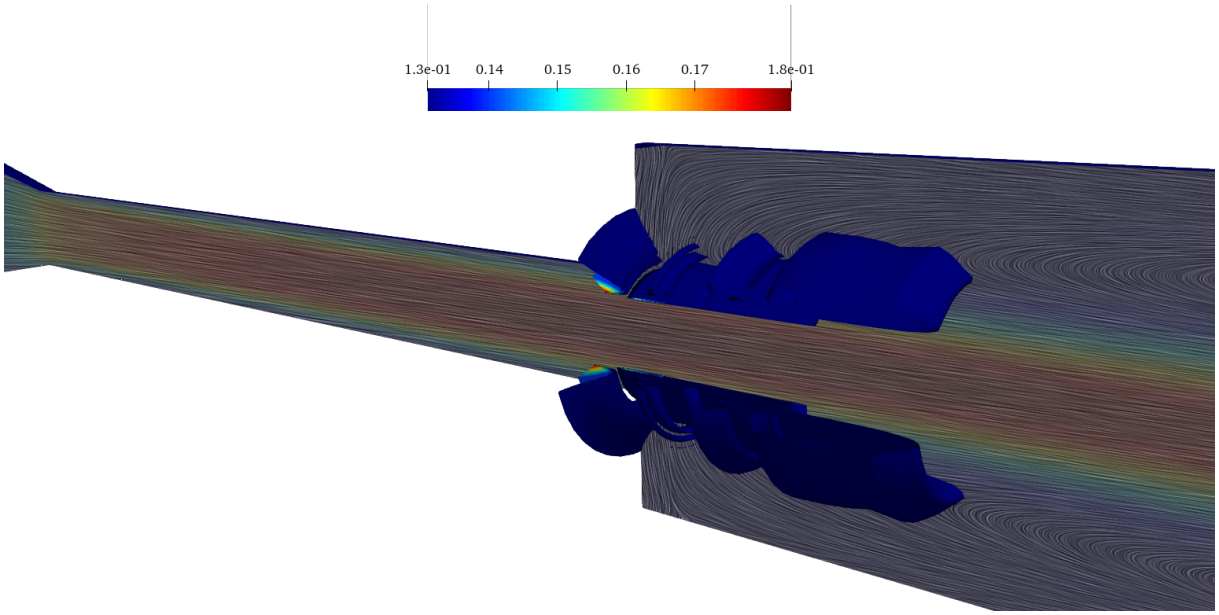

Figure 5.16: **Tridimensional view of the vapor fraction α contour at $\bar{t} = 15.6$.** When the velocity in the throat saturates, the local pressure near the edges falls below the vapor pressure and the fluid cavitates. The vapor fraction is accumulated in the vicinity of the edge due to the recirculating flow produced by the presence of the jet. In the background the axial velocity contour is reported.

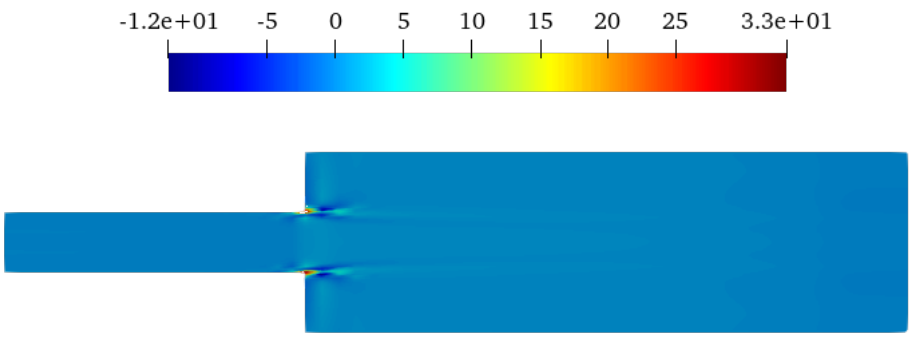

Figure 5.17: **Velocity divergence due to cavitation at $\bar{t} = 25$.** When the jet is fully developed, the only region where vapor fraction is produced is where the step introduces a pressure drop sufficient to activate cavitation.

Divergence of the velocity field

Figure 5.17 shows the divergence of the velocity field at $\bar{t} = 25$, hence when a steady configuration is reached in the sudden expansion region, downstream the nozzle throat. We remark that positive divergence means local production of vapor fraction, whereas negative divergence stands for a local condensation process. As observed also in Figures 5.12, 5.13 and 5.16, when the jet is fully developed, the sole production zone of vapor fraction is where the throat ends and the step introduces a local pressure drop able to activate cavitation. Vapor bubbles are then redistributed in the expansion region due to the presence of recirculating flow besides the jet.

Shear stresses

In this section the computation of the shear stresses is presented, comparing the cavitating and non-cavitating case for $\bar{t} = 25$. Shear stresses are important quantities in hemodynamics because they are directly related to hemolysis and platelets activation [11, 74]. According to [76], viscous shear stress is defined as follows:

$$\tau = 2\mu\epsilon(\mathbf{u}) = 2\mu\Big(\frac{1}{2}\big(\nabla\mathbf{u} + (\nabla\mathbf{u})^T\big)\Big). \tag{5.9}$$

Figure 5.19 shows the magnitude of the shear stresses computed along different lines at different axial positions. The axial coordinates considered are the same as sketched in Figure 5.6. In the inlet channel, the cone and the throat, the maximum shear stress is measured near the walls, whereas in the expansion region the peak is due to the jet and it is reached where the velocity difference between the jet and the surrounding liquid is maximum. The secondary peak is due to the recirculating flow.

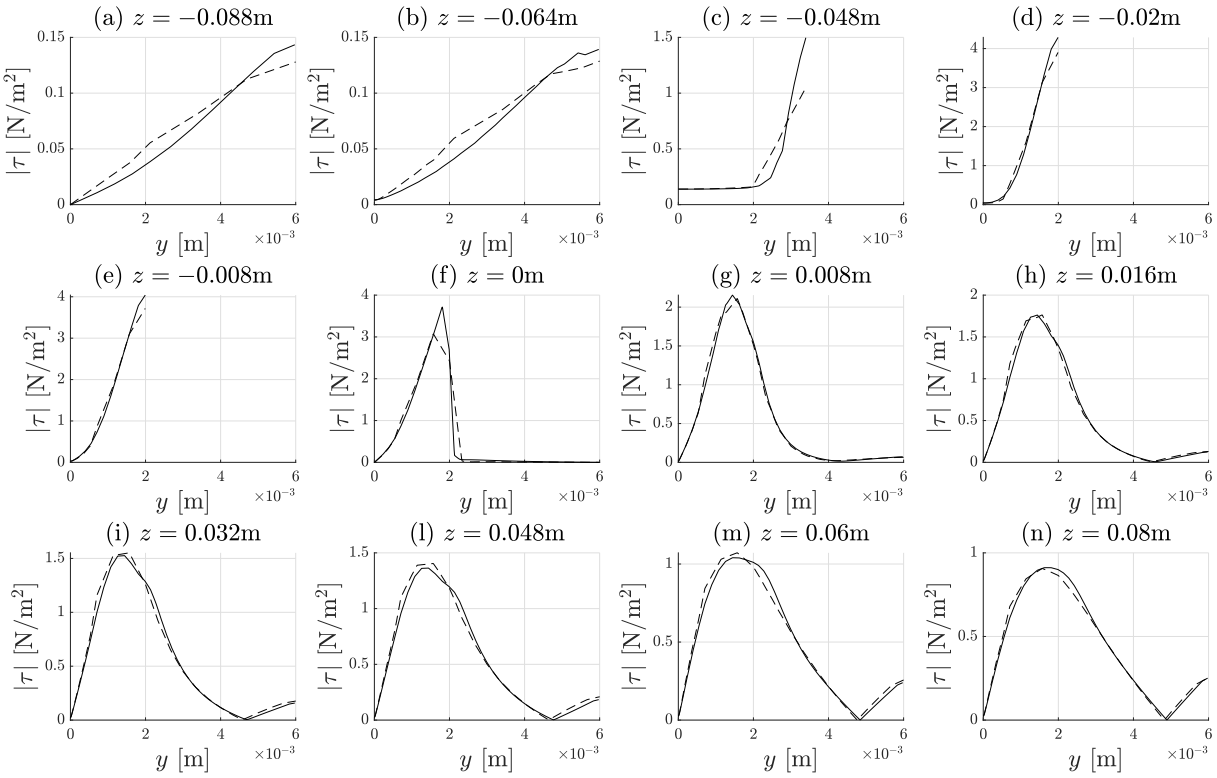

Figure 5.18: **Comparison of the shear stresses magnitude between the cavitating and non-cavitating case:** —— cavitating case, - - - non-cavitating case. Results are obtained at $\bar{t} = 25$ using the fine mesh. Across the end of the throat ($z = 0$), where vapor fraction is produced, the shear stresses predicted by the model including cavitation are higher with respect to the non-cavitating fluid. Only half of the domain is plotted due to symmetry.

The comparison between the non-cavitating and the cavitating case allows some comments: in the inlet channel and in the second part of the outlet channel, cavitation does not introduce relevant differences with respect to the non-cavitating case. This is expected because the amount of the vapor fraction is null or very limited. However, across the end of the throat, the peak of maximum shear stress is increased. This is more evident for $z = 0$, where most of the vapor fraction is produced. This result suggests that, if cavitation occurs, it is important to model its effect to obtain more accurate results in terms of shear stresses to properly estimate the expected damage on the blood tissue.

Wall shear stresses

Another important hemodynamic measure related to the velocity gradients is the wall shear stress defined as:

$$WSS = \tau\hat{\mathbf{n}} - (\tau\hat{\mathbf{n}} \cdot \hat{\mathbf{n}})\hat{\mathbf{n}}. \tag{5.10}$$

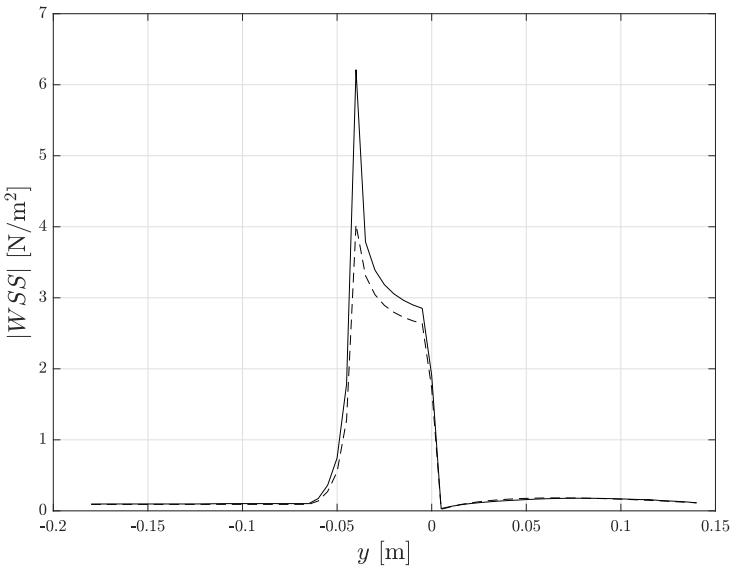

Figure 5.19: **Comparison of the wall shear stresses magnitude between the cavitating and non-cavitating case:** —— cavitating case, - - - non-cavitating case. The magnitude of the wall shear stress predicted by the cavitating case is higher in the throat region.

Figure 5.19 shows the magnitude of the wall shear stresses computed at different axial positions. Values are averaged over the circumferential direction. Once more, results coming from the model that includes cavitation are compared with the non-cavitating results. Similar conclusions to the previous paragraph can be drawn: in the inlet and the outlet region there is no noticeable difference, nevertheless in the region across the throat end and in the throat, an increased value of wall shear stress magnitude is found for the cavitating case.

5.3.4. Numerical results in the case of an inlet pulsatile velocity

In this section the results obtained imposing a pulsatile inlet flow rate are presented. We recall that the periodicity of the flow rate is $T = 0.6475$s, corresponding to a cardiac cycle of about 92 beats per minute; the maximum value of the flow rate is $Q = 5.2062 \cdot 10^{-6}$, corresponding to a maximum value for the Reynolds number of $Re = 500$.

Figures 5.20-5.24 show snapshots of the main quantities describing the flow at different instances in a portion of the fluid domain in one single cycle. Pressure and velocity are normalized as in the previous section. Time is normalized through the period duration. At the beginning of the cycle, the jet produced by the previous pulse is still visible in the velocity contour and cavitation bubbles are present at the jet's front. However, differently form the inlet velocity ramp case, the diminishing velocity produces a lower pressure in the throat and in the expansion region. This results in cavitation bubbles in the throat,

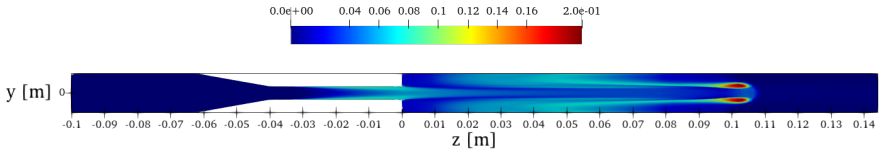

(a) Instantaneous vapor fraction contour.

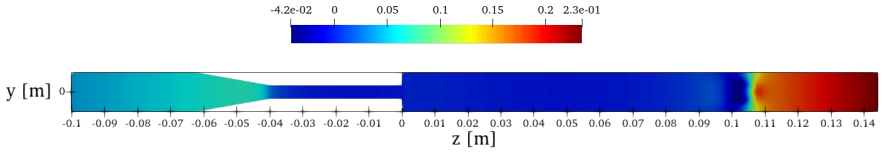

(b) Instantaneous local cavitation number contour.

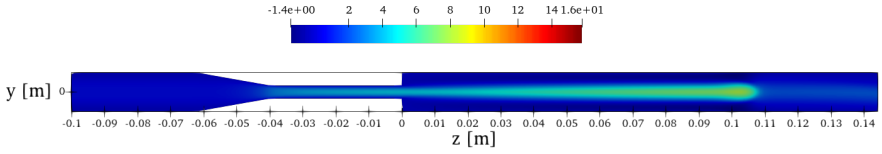

(c) Instantaneous adimensional velocity magnitude contour.

Figure 5.20: **Main features of the cavitating flow: instantaneous snapshot at t = 0.0T**. At the beginning of the period, the velocity contour shows the jet of the previous cycle. Pressure drops to lower values (negative values of the local cavitation number) and this induces cavitation in the throat.

which were not observed in the previous section. When the inlet velocity rises, pressure in the whole nozzle increases, resulting in condensation of the vapor bubbles, first in the throat section and then in the outlet channel. When the jet reaches the maximum speed, the quantities contours resemble the behaviour found in the inlet ramp velocity case. Finally, velocity decreases again and the contours observed at the end of the cycle are the same reported in the first Figure 5.20, confirming the periodicity.

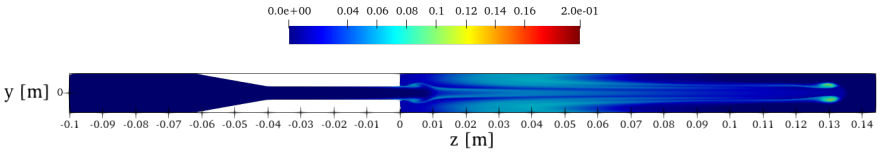

(a) Instantaneous vapor fraction contour.

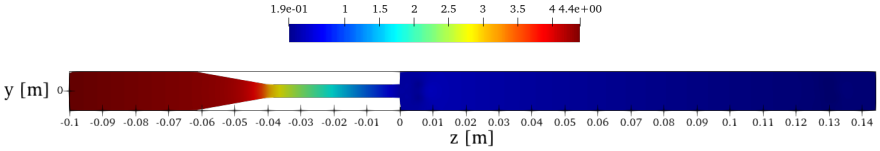

(b) Instantaneous local cavitation number contour.

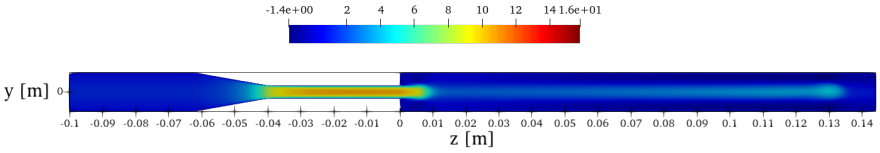

(c) Instantaneous adimensional velocity magnitude contour.

Figure 5.21: **Main features of the cavitating flow: instantaneous snapshot at t = 0.35T**. The inlet velocity is growing towards the maximum value. The flow velocity in the throat increases and this reduces in higher values of the pressure. The local cavitation number is positive in the whole domain and cavitation bubbles in the throat have condensated.

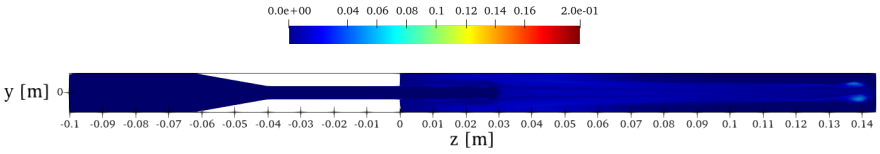

(a) Instantaneous vapor fraction contour.

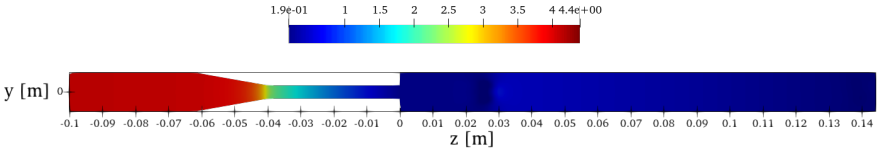

(b) Instantaneous local cavitation number contour.

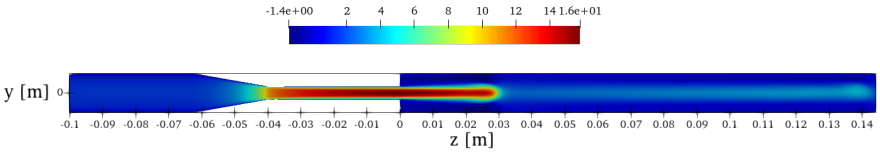

(c) Instantaneous adimensional velocity magnitude contour.

Figure 5.22: **Main features of the cavitating flow: instantaneous snapshot at t = 0.50T**. At the half of the period the inlet velocity reaches its maximum value and the jet develops in the expansion region. The higher pressures induce the flow to condensate and just small values of the vapor fraction are present in the expansion region.

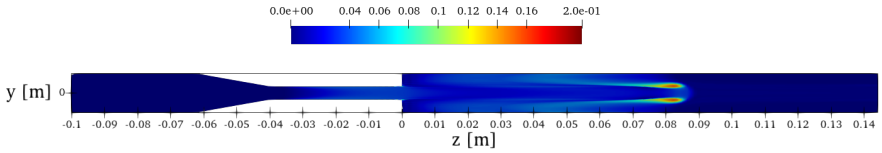

(a) Instantaneous vapor fraction contour.

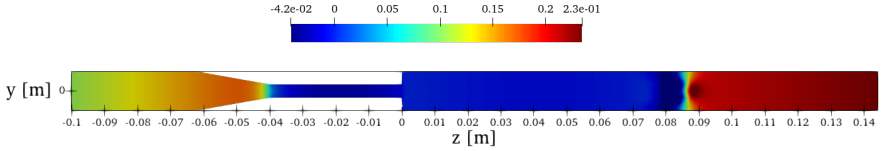

(b) Instantaneous local cavitation number contour.

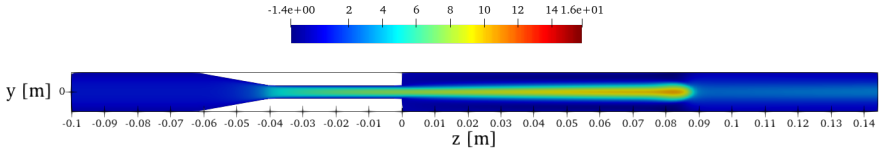

(c) Instantaneous adimensional velocity magnitude contour.

Figure 5.23: **Main features of the cavitating flow: instantaneous snapshot at t = 0.83T**. The front of the jet is fully developed and induces cavitation, just as in the case of the inlet velocity ramp. At the same time the inlet velocity is decreasing, this induces a pressure drop in the domain which results in negative values of the local cavitation number resulting in vapor bubbles forming in the throat.

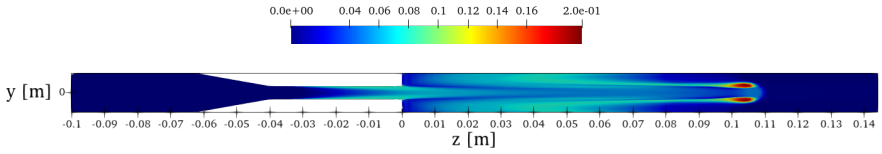

(a) Instantaneous vapor fraction contour.

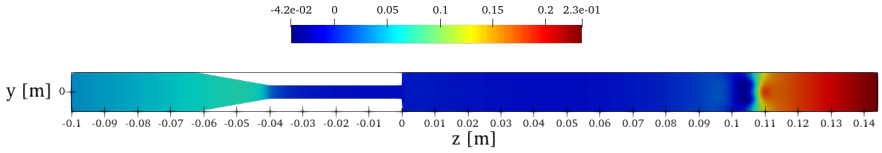

(b) Instantaneous local cavitation number contour.

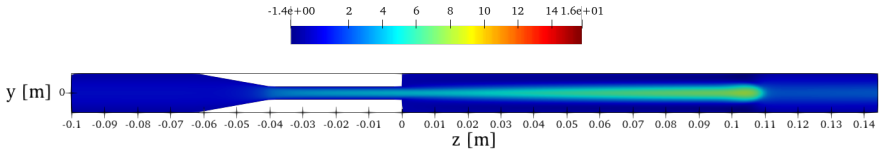

(c) Instantaneous adimensional velocity magnitude contour.

Figure 5.24: **Main features of the cavitating flow: instantaneous snapshot at t = 1.0T**. At the end of the period the contours are the same found in Figure 5.20, confirming the periodicity of the flow. The zones with negative values of local cavitation number produce positive values of volume vapor fraction α.

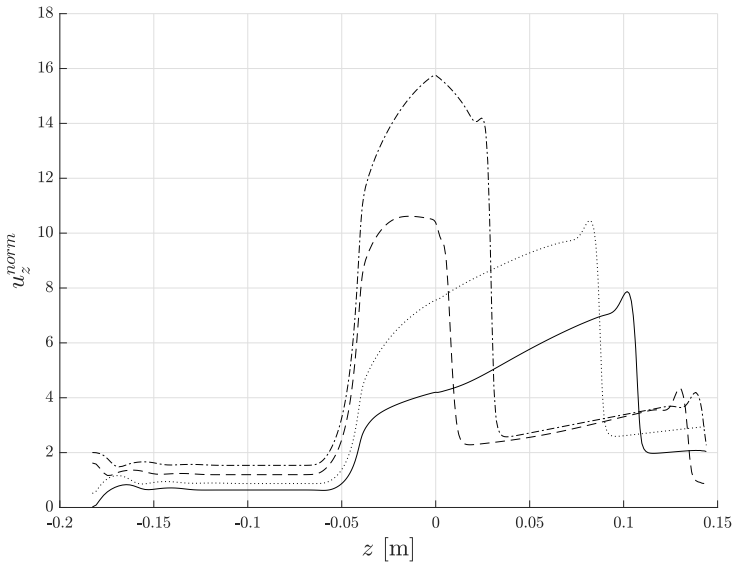

Figure 5.25: **Velocity profile along the centerline for different time instances of the pulsatile period:** —— $t = 0.0T$, - - - $t = 0.35T$, -·-· $t = 0.5T$, ····· $t = 0.83T$. The effects of the jet in the expansion region are visible more visible for $t = 0.0T$ and $t = 0.83T$, whereas the maximum velocity is reached in the throat at half of the period.

Figures 5.20 and 5.24 show the main features of the cavitation flow at the beginning of a new periodic cycle. At that stage the velocity at the inlet is at its minimum. A peculiar behaviour is observed in the throat, since the local pressure drop induced by the lower inlet velocity is responsible for cavitation. This phenomenon can be related to experimental results on cardiac valves: the occurrence of cavitation in valves has been mostly observed at the closing stages, when the inlet velocity reaches its minimum value. This is though to be mainly due to leakage backflows but at the same time these results suggest that the pressure drop due to a lower inlet velocity is also responsible for this phenomenon.

Distribution of velocity and α

In Figure 5.25 the normalized velocity distribution is plotted at the different instances of time considered in the previous section. It is remarkable that maximum velocity is reached at half of the period in the nozzle throat but the jet develops in the expansion region in the following instances, when the inlet velocity is decreasing.

In Figure 5.26 the distribution of the vapor fraction is plotted along different lines at different axial positions. Once again the attention is put on the positive value of α in the throat ($z = -0.02$m and $z = -0.08$m) for $t = 0.0T$ and on the cavitation occurring nearby the jet front in the expansion region ($z = 0.08$m) when the jet is developed in the outlet channel at $t = 0.83T$.

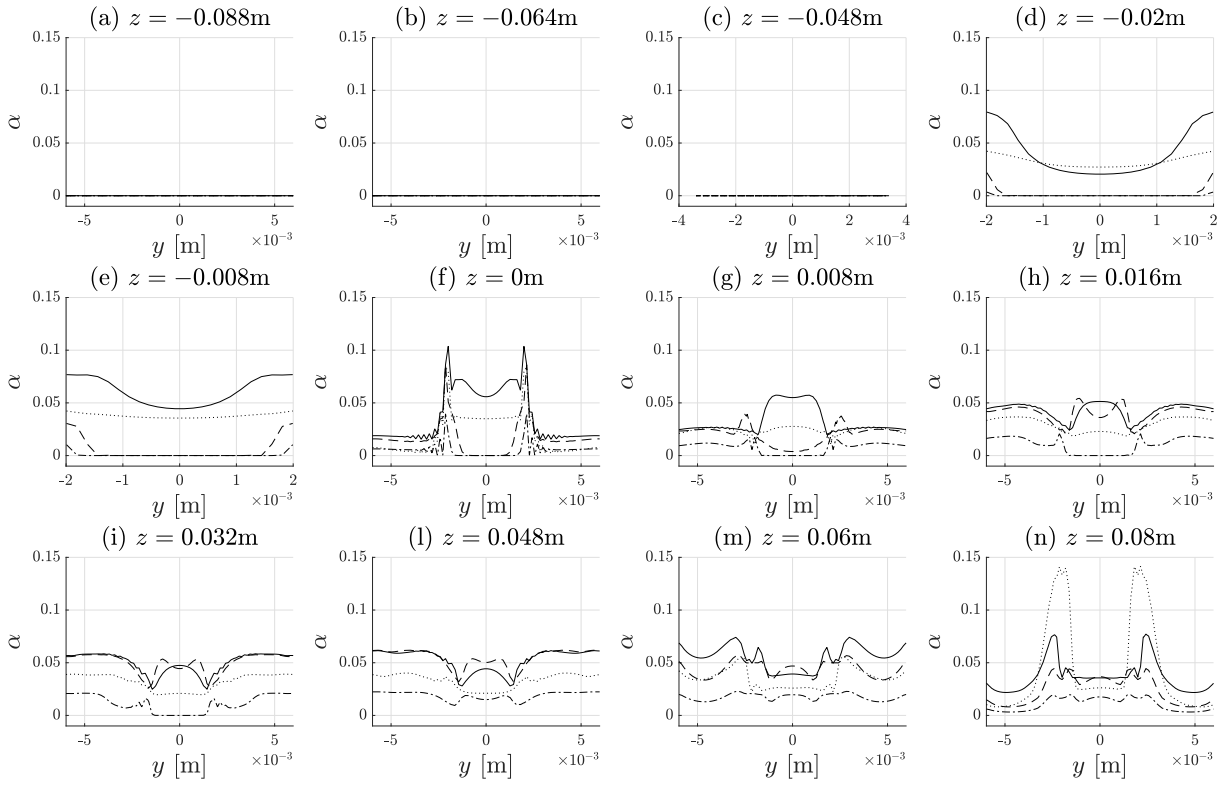

Figure 5.26: **Distribution of vapor fraction along different lines at different time instances of the pulsatile period:** —— $t = 0.0T$, - - - $t = 0.35T$, -·-· $t = 0.5T$, ····· $t = 0.83T$. Positive values of vapor fraction are found in the throat at the beginning of the period, then the increasing pressure induce condensation. When the jet is fully developed in the expansion region, cavitation bubbles appears nearby the jet front.

Shear stresses

Figure 5.27 collects the distribution of the magnitude of the shear stresses along the different lines depicted in Figure 5.6. The maximum value of the shear at each position is obtained at the instance of time when the flow velocity is higher. If we look to the throat and the accelerating cone, this happens at half period, when the inlet velocity has reached the maximum value. If, instead, we look at the expansion region, the maximum velocity is reached at $t = 0.83T$ and this reflects in an higher value of the shear stress.

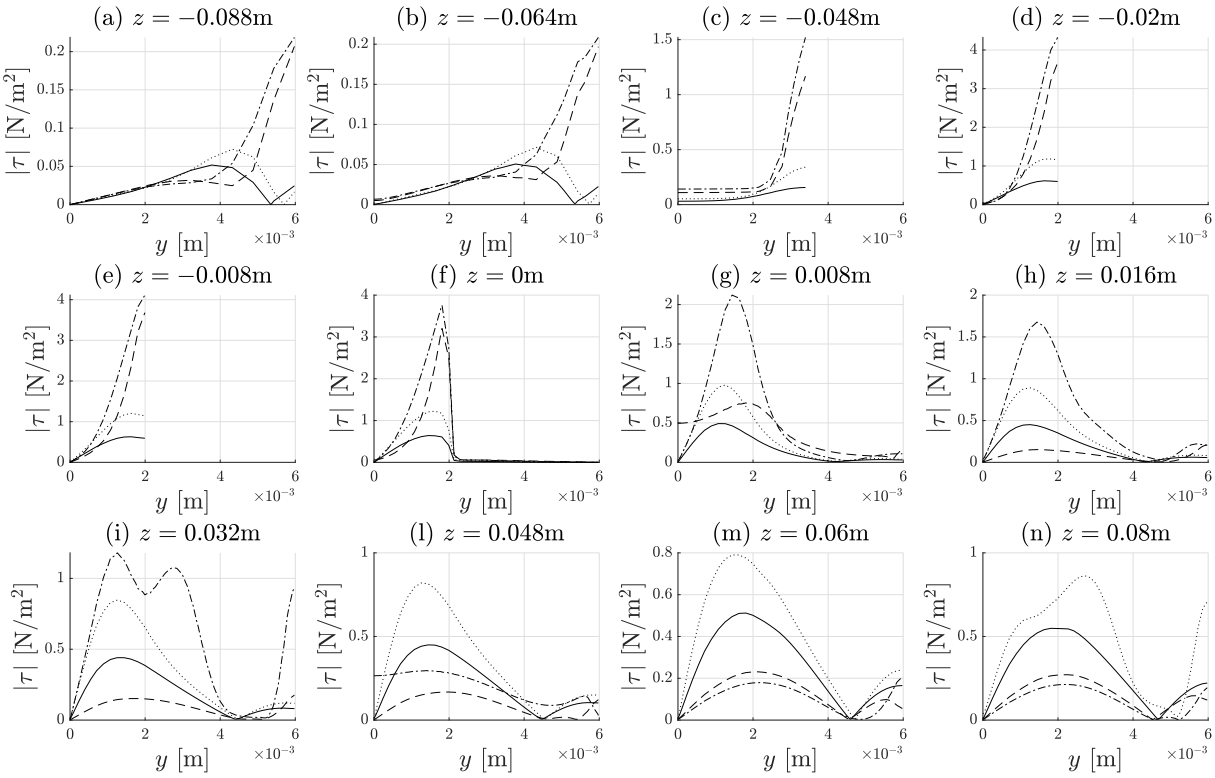

Figure 5.27: **Distribution of the magnitude of the shear stresses along different lines at different time instances in of the pulsatile period:** —— $t = 0.0T$, - - - $t = 0.35T$, -·-· $t = 0.5T$, ····· $t = 0.83T$. Higher values of flow velocity correspond to higher shear stresses: for this reason the maximum shears in the throat are reached at $t = 0.5T$, whereas in the expansion region the maximum values are at $t = 0.83T$.

6 | Numerical simulation of an idealized valve geometry

In this chapter, we present the numerical results obtained with a valve geometry. Since the first heart valve replacement performed with a caged-ball valve, more than 50 valve designs have been developed, differing principally in valve geometry, number of leaflets and material. Currently, the most commonly used valves are those with a bileaflet design [14], thus we numerically simulate a simplified version of this geometry. The bileaflet design consists of two semicircular leaflets that pivot on hinges; Figure 6.1 shows the Medtronic Open Pivot bileaflet valve [51] as a reference.

To perform numerical simulations, we consider a simplified version of the actual geometry modelled as a straight cylinder with two semicircular leaflets in a fixed position. We show the 2D and 3D views of the computational domain in Figure 6.2. The cylinder diameter is $D = 25$ mm, which is a typical size for MHVs [51]. The leaflets are in a fixed position, with an opening angle $\theta = 45°$. This is done to simulate the closing instances of the bileaflet valve, since most of *in vitro* cavitation is observed in these conditions [63]. The length of the inlet and the outlet channel is set to $L_{\text{in}} = L_{\text{out}} = 0.1$ m, to avoid the influence of the boundary conditions at the valve location.

The model parameters, as the density and viscosity of the liquid and vapor phase are set to the same values described in the previous chapters. The same holds for the constants of the Zwart cavitation model [85].

The Reynolds number is defined using the diameter and the mean inlet velocity $\bar{u}_z$:

$$\mathbb{R}e = \frac{\rho_l \bar{u}_z D}{\mu_l} = \frac{4}{\pi}\frac{Q}{D}\frac{\rho_l}{\mu_l}. \tag{6.1}$$

In the above expression, Q is the volumetric flow rate. From (6.1) the maximum Reynolds number of the simulation is $\mathbb{R}e = 4900$.

Figure 6.1: **Medtronic Open Pivot (TM) bileaflet valve.** Image taken from [51]. Bileaflet design consists of two semicircular leaflets that pivot on hinges

(a) 2D view of slice the computational domain.

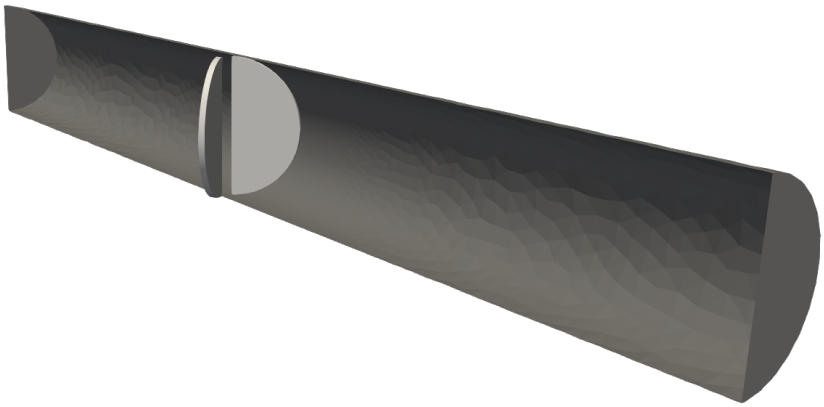

(b) 3D views of the computational domain.

Figure 6.2: **2D and 3D views of the computational domain**. The domain resembles a simplified version of a bileaflet mechanical valve at closing instances. Blood flows from left to right.

The cavitation number σ is computed using the value of the outlet pressure, as follows:

$$\sigma = \frac{P - P_v}{\frac{1}{2}\rho_l \bar{u}_z^2} = \frac{P - P_v}{\frac{1}{2}\rho_l \left(\frac{4Q}{\pi D^2}\right)^2} = 3.54. \tag{6.2}$$

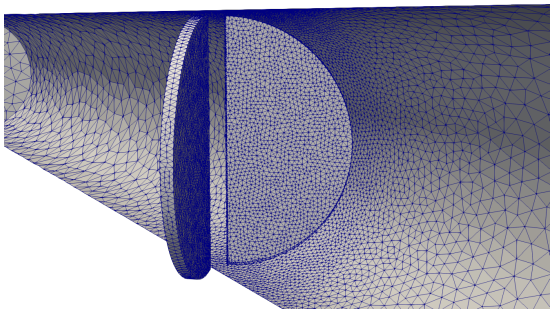

Figure 6.3: **Surfaces of the computational domain meshed in 2D.**

	Mesh
Number of cells	420549
Number of velocity DOFs	228525
Number of pressure DOFs	76175
Number of α DOFs	76175
$h_{\mathbf{max}}$	$6.4 \cdot 10^{-3}$ m
$h_{\mathbf{min}}$	$4.1 \cdot 10^{-4}$ m
$h_{\mathbf{mean}}$	$1.1 \cdot 10^{-3}$ m

Table 6.1: **Main features the mesh used to perform numerical simulations.**

The time step is set to $\Delta t = 10^{-3}$ s. The dimensionless time step is obtained and written as: $\Delta \bar{t} = \Delta t \bar{u}_z / D = 0.024$.

6.1. Mesh generation

As in the previous chapters, we use Gmsh [23] for the mesh generation. For this geometry an unstructured approach is followed. The tetrahedral mesh is obtained through the *MeshAdapt* algorithm, which is the most robust meshing algorithm for complex curved surfaces available in Gmsh [23].

We perform a local refinement in the valve location, where elements have a mesh spacing of $0.02D$. Elements are larger as the distance from the valves increases: the mesh spacing at the inlet and outlet boundaries is $0.16D$. Figure 6.3 shows a clip of the surfaces of the computational domain meshed in 2D. In Table 6.1, we report the number of the cells, the active degrees of freedom (DOFs) and the values of h_{max}, h_{min} and h_{mean}.

6.2. Boundary conditions

As in the case of the FDA nozzle benchmark described in Chapter 5, we select the cavitation model with the non-conservative formulation of the vapor fraction transport equation. We impose an homogeneous Dirichlet boundary condition on the inlet for α, and an homogeneous Neumann on the other boundaries (channel wall, outlet, leaflet surface).

We impose a Dirichlet boundary condition for the inlet velocity, whth a pulsatile evolution in time and a parabolic distribution in space. The periodicity of the flow is $T = 0.6475$ s, corresponding to a cardiac cycle of about 92 beats per minute. No-slip boundary conditions are set on the channel wall and on the leaflets. The flow rate imposed at the inlet varies from $Q = 0$ to $Q = 300$ ml/s $= 3.0 \cdot 10^{-4}$ m^3/s. On the outlet boundary, a pressure boundary condition is set: $P_{\text{out}} = 6700$ Pa. The values for the inlet flow rate and the outlet pressure are taken from [10]; the value for the pressure is chosen computing the mean pressure in the left ventricle: $\bar{P}_{LV} = 50$ mmHg $= 6700$ Pa. The mitral valve hemodynamics is, in fact, more complex and considering the outlet pressure as a constant is a simplification.

6.3. Numerical results

In this section we present the numerical results on the valve geometry. The simulation was carried out on gigat computing system available at MOX laboratories, using one node with 32 CPUs. The total simulation time, for each period, resulted in 14 h 35 min. In the following, results over one period are presented; time is normalized through the period.

In Figures 6.4 and 6.5 the streamlines and the instantaneous structures of the flow, identified by means of Q-criterion [33] are shown at different instances. The maximum values for the velocity are found for $t = 0.5T$, when the inlet flow rate is maximum. The peak velocity is in the order of 3 m/s, which is comparable with the squeeze flows found at valve closing instances in [45, 60]. Figure 6.5 shows that coherent structures develop across the valve, and persist when the inlet velocity decreases. Cavitation appears starting from $t = 0.54T$ and all the vapor bubbles condensates within $t = 0.96T$. The vapor bubbles have a lifetime in the order to $10 - 20$ ms; in Figure 6.6 the evolution of a single vapor bubble is followed for few milliseconds: the recirculating flows convect the bubble near the valve structure, where vapor condensates, possibly causing some pitting and and damage on the leaflet. Figure 6.7 shows 3D contours of the vapor fraction in the whole domain at different instances: in Figure 6.7(a), some amount of α is recognized on the right leaflet and in Figure 6.8 the shear stress distribution at the same instant shows an higher stress

value in that spot, confirming that modelling cavitation is important to predict the shear stresses, as we found also in section 5.3.4.

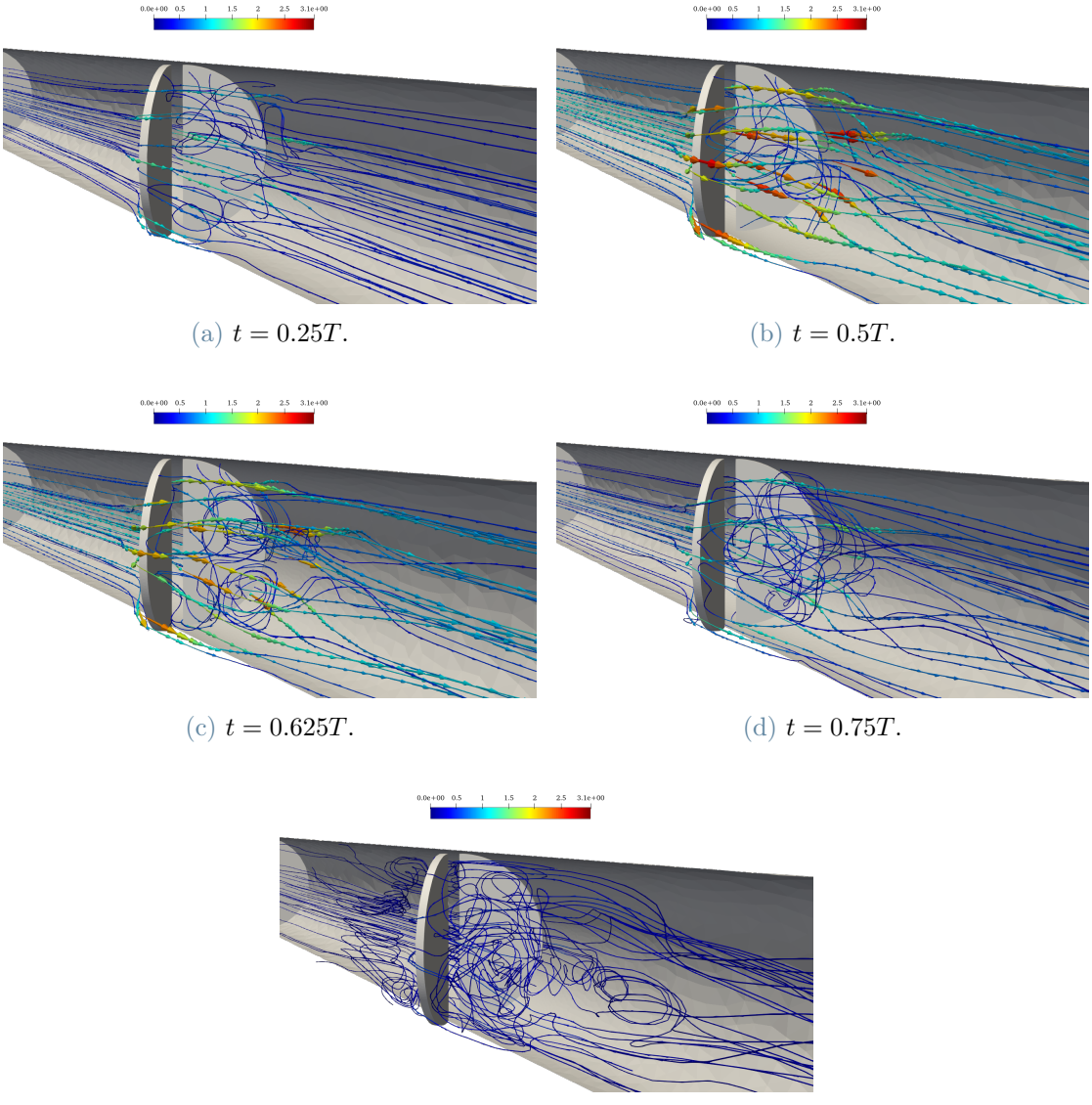

(a) $t = 0.25T$. (b) $t = 0.5T$.

(c) $t = 0.625T$. (d) $t = 0.75T$.

(e) $t = 0.875T$.

Figure 6.4: **Flow streamlines at different time instances**: The streamlines are colored by the velocity magnitude in m/s. **(a)**: the inlet flow rate is growing and velocity streamlines develop; **(b)**: the velocity reaches the maximum value, approximately 3 m/s, which matches literature results on MHVs squeeze flows [45, 60]; **(c)**: the flow becomes unstable, showing a turbulent behaviour due to the high Reynolds number $\mathbb{R}e = 4900$; **(d)** and **(e)**: the flow rate goes to zero and so the velocity field.

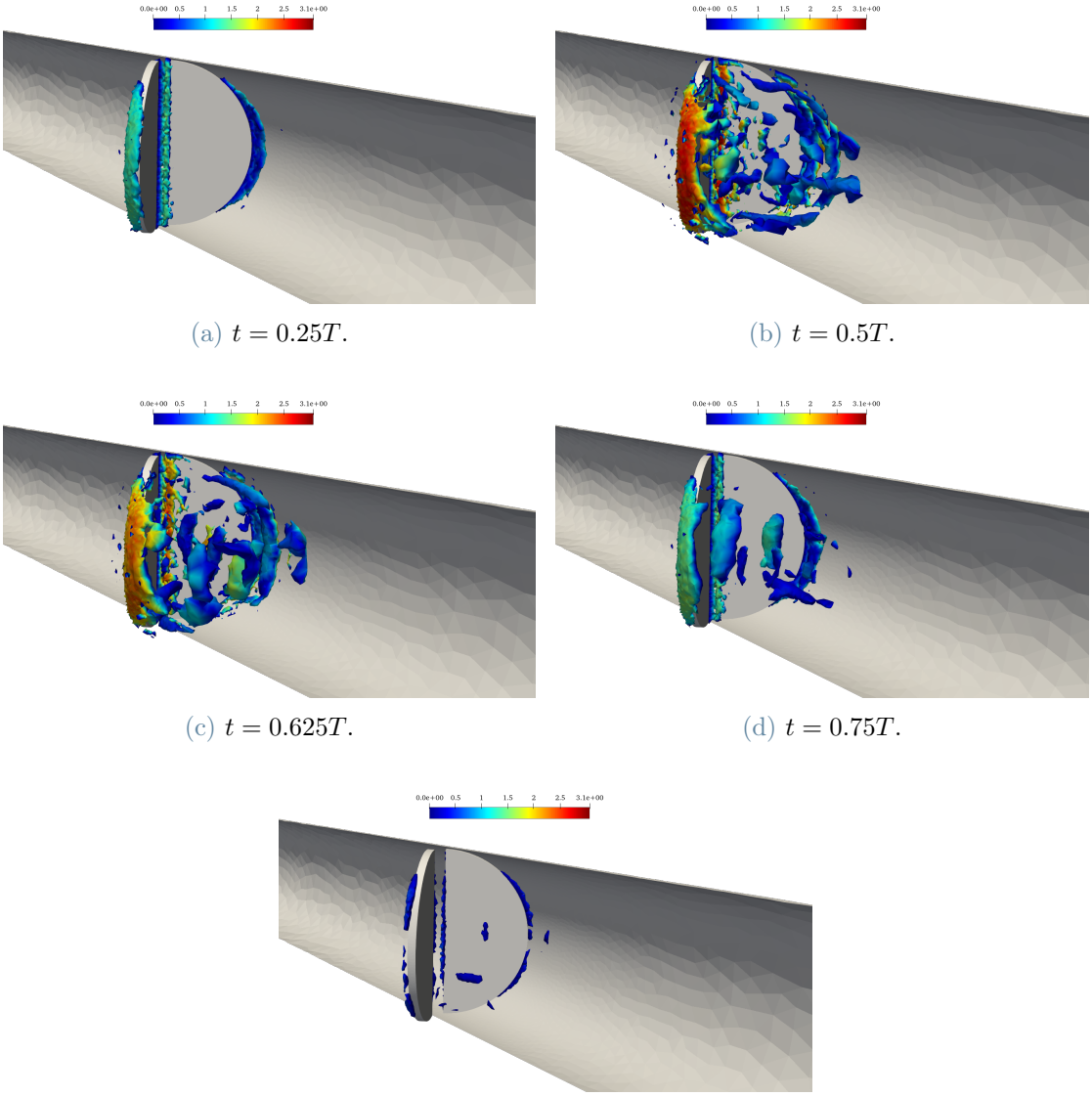

(a) $t = 0.25T$.

(b) $t = 0.5T$.

(c) $t = 0.625T$.

(d) $t = 0.75T$.

(e) $t = 0.875T$.

Figure 6.5: **Representation of the Q-criterion contours colored by velocity magnitude at selected times**. Starting from **(b)**, vortical structures according to the Q-criterion appear in the flow. The flow becomes unstable, and vortical structures are found in the wake also in **(c)** and **(d)**, when the inlet flow rate is decreasing. In **(e)** the flow is almost completely still and few vortical structures appear in the flow.

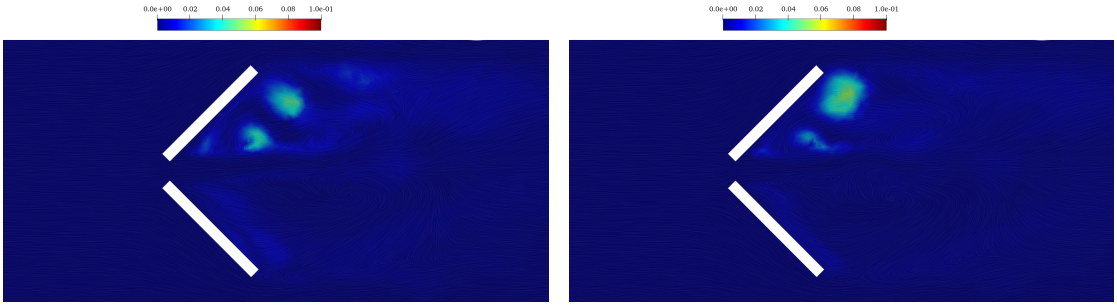

(a) α distribution at t_0.

(b) α distribution at $t_0 + 10$ ms.

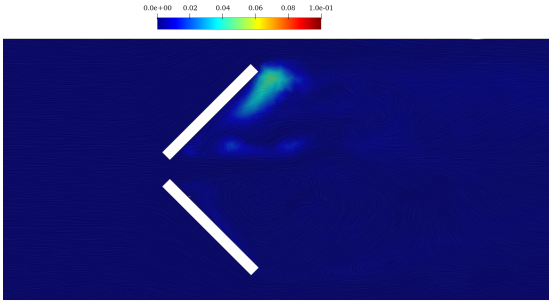

(c) α distribution at $t_0 + 20$ ms.

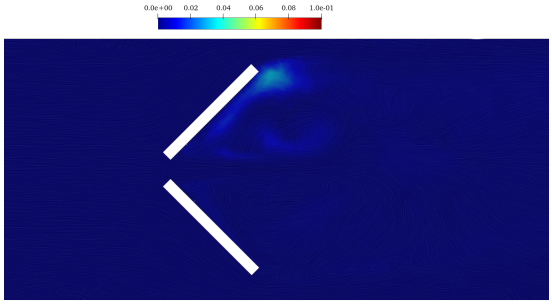

(d) α distribution at $t_0 + 30$ ms.

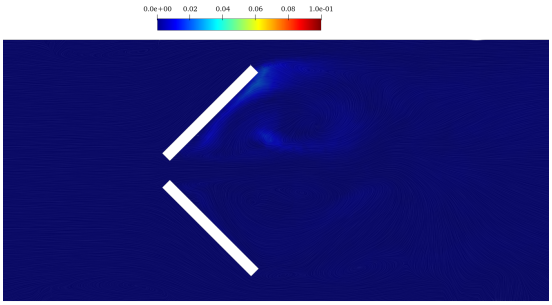

(e) α distribution at $t_0 + 40$ ms.

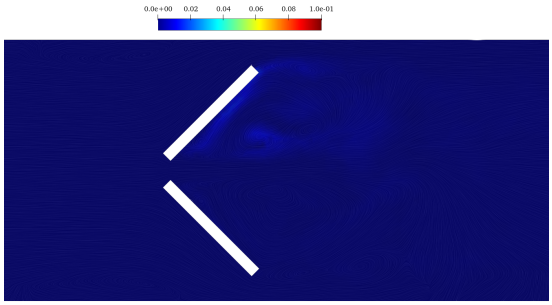

(f) α distribution at $t_0 + 50$ ms.

Figure 6.6: **Vapor bubble collapse dynamics**. The distribution of α over a portion of the domain is shown at different instances. A single vapor bubble is followed starting from $t_0 = 0.70T$, for a few milliseconds. The bubble has a life of $10 - 20$ ms. The recirculating flows convey the bubble near the valve structure, where it collapse, possibly causing some pitting and and damage on the leaflet.

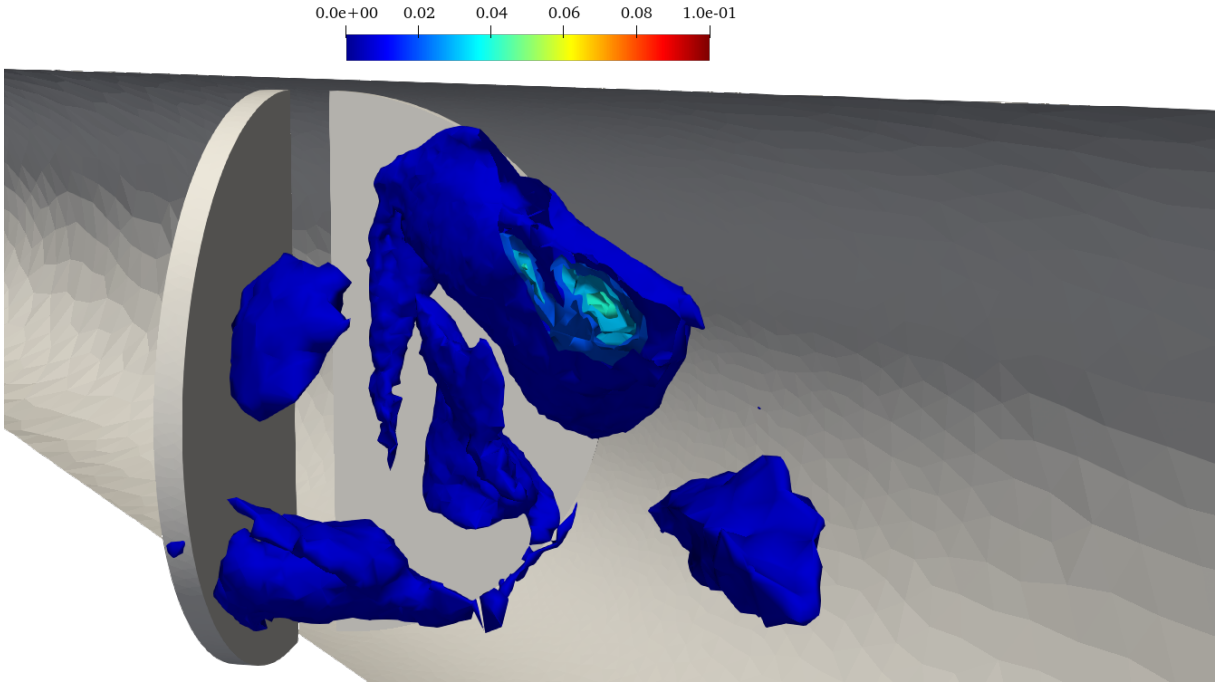

(a) $t = 0.75T$.

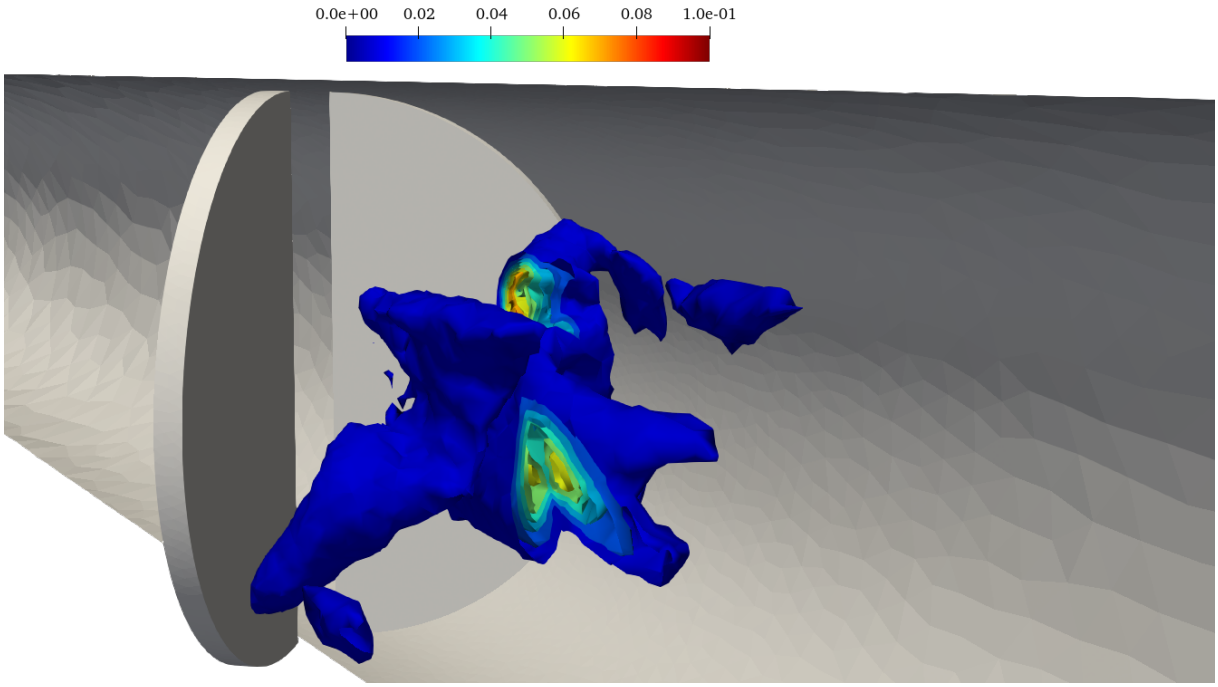

(b) $t = 0.875T$.

Figure 6.7: **Tridimensional contour of the vapor fraction distribution**. The vapor fraction contour is plotted in the whole domain. Some vapor bubbles are clipped for an inside better visualization. In **(a)**, some vapor fraction is recognized on the surface of the right leaflet. This information is correlated to the shear distribution plotted in Figure 6.8.

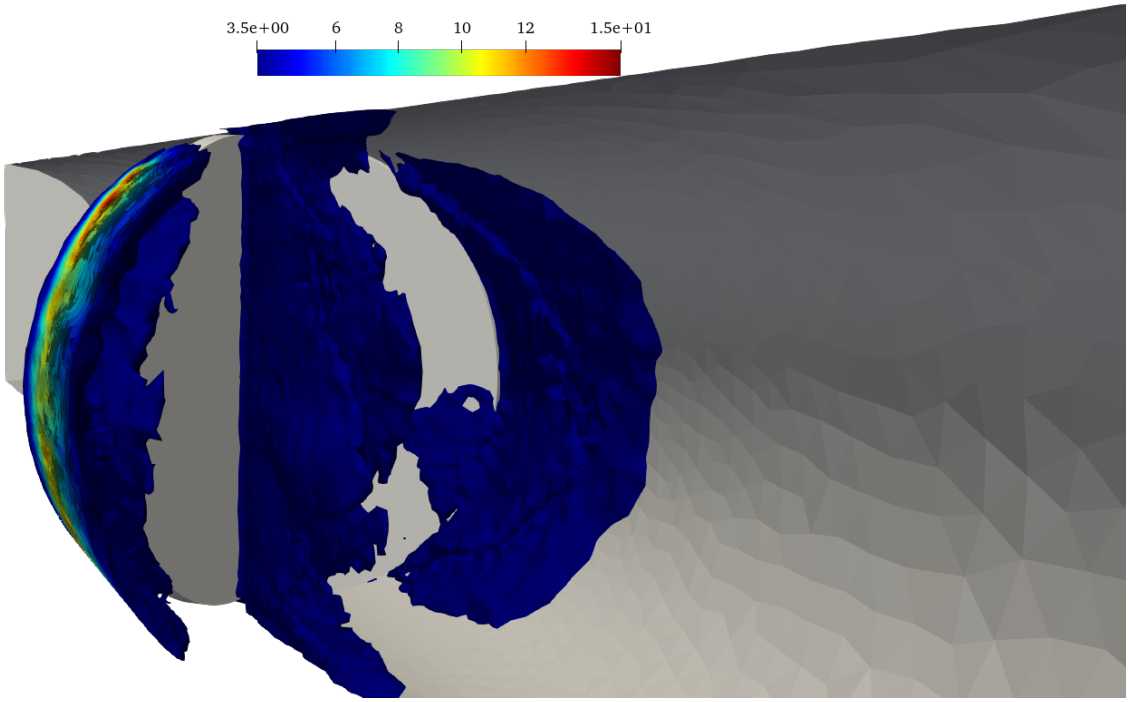

Figure 6.8: **Shear stress contour in the computational domain.** On the right leaflet we found an increased shear stress with respect to the left leaflet. This is because some vapor fraction has reached the leaflet (see Figure 6.7(a)), and is responsible for an enhanced shear stress.

7 | Conclusions and future developments

We proposed a numerical method to perform numerical simulation on cavitation occurring in blood flows. Indeed, very few examples examples of numerical simulations of the circulatory system including cavitation models have been found in the literature.

We first performed a literature review on the cavitation phenomena and the state-of-the-art models used to simulate cavitation. This led to consider an homogeneous mixture model, specifically the Zwart model [85], because it proved to be effective in modelling cavitation across Venturi-type geometries. We developed the mathematical model, highlighting the coupling between the mixture mass and momentum conservation with the vapor fraction transport equation. We proposed a novel stabilized Finite Element formulation for the numerical modeling of cavitation flow: space discretization was performed by means of finite elements, time discretization by means of finite differences. We implemented the cavitation model in `life`$^{\texttt{x}}$ [3], a C++ Finite Element library focused on cardiac applications. Insights have been provided on the stabilization methods used for the mixture mass and momentum conservation system and the additional equation of the cavitation model as well as on the coupling strategy. For the solution of the coupled problem, we followed a staggered approach mainly for its flexibility and its ease of generalization to the coupling of possible additional models, as for example models for the fluid-structure interaction or turbulence models. One of the main features of the cavitating mixture was the non-zero value of the velocity divergence where vapor fraction is generated or condensates to the liquid state. Hinging upon an energy estimate for the cavitation model, we highlighted the role of the velocity divergence.

The cavitating cylinder benchmark provided meaningful results when compared to literature data with the same geometry and boundary conditions. One of the most interesting outcomes was the change in the distribution of pressure over the cylinder surface, where cavitation limited the minimum value of C_P with respect to the non-cavitating case. We found interesting implications of cavitation on the Strouhal number, which was reduced

with respect to the non-cavitating case, as expected from the literature results.

We considered the FDA nozzle geometry because it is a common benchmark in hemodynamics and because it resembles the Venturi-type geometry characterizing the flow through mechanical heart valves at the closing stages. Also in this case, the cavitation model provided relevant insights: cavitation yielded an increase in shear stress, and the vapor phase was generated also within the narrower region of the domain in the case of pulsatile inlet velocity. This results suggested that considering cavitation is important to predict the stresses acting on the blood tissue. At the same time throat cavitation resembled the experimental results on MHVs, where most of the cavitation occurs at the closing stages, when the inlet pressure reached its minimum value.

In Chapter 6, we tested the cavitation model on a more complex geometry which resembled a bileaflet mechanical heart valve. The model demonstrated effective in predicting cavitation at high Reynolds ($\mathbb{R}e = 4900$), and allowed to locate the regions where the mixture evaporated and condensated. In the wake, the vapor bubbles showed a lifetime of the order of $10 - 20$ ms, matching the experimental measurements by [63]. We found larger values of the shear stress if cavitation bubbles interact with the leaflets, with respect to the non-cavitating regions, thus identifying the regions of the valve being more subjected to possible damage by cavitation.

In conclusion, the Zwart cavitation model [85] demonstrated capable of predicting cloud cavitation on different geometries and the computational tools that have been developed are fully integrated in a software library for clinical applications. Being able to model and predict the occurrence of cloud cavitation is very much relevant to develop strategies to suppress and avoid this phenomena, responsible for an enhanced erosion and pitting on implanted MHVs and for higher shear stresses acting on the blood tissue which force patient to be treated with anticoagulants.

Future developments of this work may be considered, along different directions. More complex geometries may be evaluated in order to investigate cavitation phenomena across more realistic mechanical heart valves. Domain motion may be included by implementing the arbitrary Lagrangian–Eulerian (ALE) Finite Element formulation of the cavitation model to account for the movement of the leaflets, possibly coupling the cavitation model with a model for the fluid-structure interaction. Finally, a turbulence model may be added to the cavitation model for turbulent simulations. The Variational Multiscale LES turbulence modeling [31] is already implemented in `life`$^{\mathtt{x}}$ and may be considered suitable for this purpose.

Bibliography

[1] Deal.ii - an open source finite element library. `https://www.dealii.org/`.

[2] Ansys fluent - fluid simulation software. `https://www.ansys.com/it-it/products/fluids/ansys-fluent`.

[3] Lifex. `https://lifex.gitlab.io/`.

[4] C. Alamprese. The effects of novel pasteurization technologies on egg product functionalities. 2019.

[5] T. S. Andersen, P. Johansen, B. O. Christensen, P. K. Paulsen, H. Nygaard, and J. M. Hasenkam. Intraoperative and postoperative evaluation of cavitation in mechanical heart valve patients. *The Annals of Thoracic Surgery*, 81(1):34–41, 2006. ISSN 0003-4975. doi: https://doi.org/10.1016/j.athoracsur.2005.06.080.

[6] A. Andriotis, M. Gavaises, and C. Arcoumanis. Vortex flow and cavitation in diesel injector nozzles. *Journal of Fluid Mechanics*, 610:195–215, 2008. doi: 10.1017/S0022112008002668.

[7] Y. Bazilevs, V. Calo, J. Cottrell, T. Hughes, A. Reali, and G. Scovazzi. Variational multiscale residual-based turbulence modeling for large eddy simulation of incompressible flows. *CMAME*, 197, 05 2007.

[8] J. R. Blake and D. C. Gibson. Cavitation bubbles near boundaries. *Annual Review of Fluid Mechanics*, 19(1):99–123, 1987. doi: 10.1146/annurev.fl.19.010187.000531.

[9] A. Brooks and T. Hughes. Streamline upwind/petrov-galerkin formulations for convection dominated flows with particular emphasis on the incompressible navier-stokes equations. *Computer Methods in Applied Mechanics and Engineering*, 32(1-3):199–259, 1982. doi: 10.1016/0045-7825(82)90071-8. cited By 3971.

[10] M. Broomé, E. Maksuti, A. Bjällmark, B. Frenckner, and B. Janerot-Sjöberg. Closed-loop real-time simulation model of hemodynamics and oxygen transport in the cardiovascular system. *Biomedical engineering online*, 12:69, 07 2013. doi: 10.1186/1475-925X-12-69.

[11] C. Caro. Discovery of the role of wall shear in atherosclerosis. *Arteriosclerosis, thrombosis, and vascular biology*, 29:158–61, 12 2008. doi: 10.1161/ATVBAHA.108.166736.

[12] K. B. Chandran and S. Aluri. Mechanical valve closing dynamics: Relationship between velocity of closing, pressure transients, and cavitation initiation. *Annals of Biomedical Engineering 1997 25:6*, 25:926–938, 1997. ISSN 1573-9686. doi: 10.1007/BF02684129.

[13] F. Chemat, Zill-E-Huma, and M. Khan. Applications of ultrasound in food technology: Processing, preservation and extraction. *Ultrasonics Sonochemistry*, 18(4):813–835, 2011. doi: 10.1016/j.ultsonch.2010.11.023.

[14] L. Dasi, H. Simon, P. Sucosky, and A. Yoganathan. Fluid mechanics of artificial heart valves. *Clinical and Experimental Pharmacology and Physiology*, 36(2):225–237, 2009.

[15] S. Deparis, D. Forti, G. Grandperrin, and A. Quarteroni. FaCSI: A block parallel preconditioner for fluid–structure interaction in hemodynamics. *Journal of Computational Physics*, 327, 10 2016. doi: 10.1016/j.jcp.2016.10.005.

[16] B. C. Earls. Cavitation in medicine. *Interface Focus*, 2015.

[17] L. Euler. Untersuchung einer nach den euler'schen vorschlägen gebauten wasserturbine. 1754.

[18] R. Farwig, H. Kozono, and H. Sohr. Global weak solutions of the navier-stokes equations with nonhomogeneous boundary data and divergence. *Rendiconti del Seminario Matematico della Università di Padova*, 125:51–70, 2011.

[19] D. Forti and L. Dede. Semi–implicit bdf time discretization of the navier–stokes equations with vms–les modeling in a high performance computing framework. *Computers & Fluids*, 117:168–182, 05 2015. doi: 10.1016/j.compfluid.2015.05.011.

[20] S. Gaggero, G. Tani, M. Viviani, and F. Conti. A study on the numerical prediction of propellers cavitating tip vortex. *Ocean Engineering*, 92:137–161, 2014. doi: 10.1016/j.oceaneng.2014.09.042.

[21] S. Gao, K. Wong, T. Hansberg, W. Lam, D. Droste, and E. Ringelstein. Microembolic signal predicts recurrent cerebral ischemic events in acute stroke patients with middle cerebral artery stenosis. *Stroke*, 35:2832–2836, 12 2004. ISSN 1524-4628. doi: 10.1161/01.STR.0000147035.31297.B6.

[22] D. Georgiadis, A. Wenzel, D. Lehmann, A. Lindner, H. Zerkowski, S. Zierz, and

M. Spencer. Influence of oxygen ventilation on doppler microemboli signals in patients with artificial heart valves. *Stroke*, 28:2189–2194, 1997. ISSN 0039-2499. doi: 10.1161/01.STR.28.11.2189.

[23] C. Geuzaine and J.-F. Remacle. Gmsh: A 3-d finite element mesh generator with built-in pre- and post-processing facilities. *International Journal for Numerical Methods in Engineering*, 79:1309 – 1331, 09 2009. doi: 10.1002/nme.2579.

[24] M. Ghorbani, O. Oral, S. Ekici, D. Gozuacik, and A. Kosar. Review on lithotripsy and cavitation in urinary stone therapy. *IEEE reviews in biomedical engineering*, 9: 264–283, 2016. ISSN 1941-1189. doi: 10.1109/RBME.2016.2573381.

[25] F. Giussani, F. Piscaglia, G. Saez-Mischlich, J. Hèlie, F. Giussani, F. Piscaglia, G. Saez-Mischlich, and J. Hèlie. A three-phase vof solver for the simulation of in-nozzle cavitation effects on liquid atomization. *Journal of Computational Physics*, 406:109068, 4 2020. ISSN 0021-9991. doi: 10.1016/J.JCP.2019.109068.

[26] A. Gnanaskandan and K. Mahesh. Numerical investigation of near-wake characteristics of cavitating flow over a circular cylinder. *Journal of Fluid Mechanics*, 790: 453–491, 2016. doi: 10.1017/jfm.2016.19.

[27] H. Gomez and K. G. van der Zee. Computational phase-field modeling. 2017.

[28] I. Harari and T. J. Hughes. What are c and h?: Inequalities for the analysis and design of finite element methods. *Computer Methods in Applied Mechanics and Engineering*, 97(2):157–192, 1992. ISSN 0045-7825. doi: https://doi.org/10.1016/0045-7825(92)90162-D.

[29] S. J. Head, M. Çelik, and A. P. Kappetein. Mechanical versus bioprosthetic aortic valve replacement. *European Heart Journal*, 38(28):2183–2191, 04 2017. ISSN 0195-668X. doi: 10.1093/eurheartj/ehx141.

[30] C. Hirt and B. Nichols. Volume of fluid (vof) method for the dynamics of free boundaries. *Journal of Computational Physics*, 39(1):201–225, 1981. ISSN 0021-9991. doi: https://doi.org/10.1016/0021-9991(81)90145-5.

[31] T. Hughes, L. Mazzei, and K. Jansen. Large eddy simulation and the variational multiscale method. *Computing and Visualization in Science*, 3:47–59, 01 2000. doi: 10.1007/s007910050051.

[32] T. J. Hughes and M. Mallet. A new finite element formulation for computational fluid dynamics: Iii. the generalized streamline operator for multidimensional advective-

diffusive systems. *Computer Methods in Applied Mechanics and Engineering*, 58(3): 305–328, 1986. ISSN 0045-7825. doi: https://doi.org/10.1016/0045-7825(86)90152-0.

[33] J. Hunt, A. Wray, and P. Moin. Eddies, streams, and convergence zones in turbulent flows. *Studying Turbulence Using Numerical Simulation Databases*, pages 193–208, 11 1988.

[34] B. Ji, X. Luo, R. E. Arndt, X. Peng, and Y. Wu. Large eddy simulation and theoretical investigations of the transient cavitating vortical flow structure around a naca66 hydrofoil. *International Journal of Multiphase Flow*, 68:121–134, 2015. ISSN 0301-9322.

[35] H. Jiang and L. Cheng. Strouhal–reynolds number relationship for flow past a circular cylinder. *Journal of Fluid Mechanics*, 832:170–188, 2017. doi: 10.1017/jfm.2017.685.

[36] P. Johansen. Mechanical heart valve cavitation. *Expert review of medical devices*, 1: 95–104, 2004. ISSN 1743-4440. doi: 10.1586/17434440.1.1.95.

[37] P. Johansen, T. Andersen, J. Hasenkam, H. Nygaard, and P. Paulsen. Mechanical heart valve cavitation in patients with bileaflet valves. *Annual International Conference of the IEEE Engineering in Medicine and Biology Society. IEEE Engineering in Medicine and Biology Society. Annual International Conference*, 2014:5655–5658, 11 2014. ISSN 2694-0604. doi: 10.1109/EMBC.2014.6944910.

[38] W. Klepetko, A. Moritz, J. Mlczoch, H. Schurawitzki, E. Domanig, and E. Wolner. Leaflet fracture in edwards-duromedics bileaflet valves. *The Journal of Thoracic and Cardiovascular Surgery*, 97:90–94, 1 1989. ISSN 0022-5223.

[39] P. Koukouvinis, C. Bruecker, and M. Gavaises. Unveiling the physical mechanism behind pistol shrimp cavitation. *Scientific Reports 2017*, 7:1–12, 10 2017. ISSN 2045-2322. doi: 10.1038/s41598-017-14312-0.

[40] A. Kubota, H. Kato, and H. Yamaguchi. A new modelling of cavitating flows: A numerical study of unsteady cavitation on a hydrofoil section. *Journal of Fluid Mechanics*, 240(3):59–96, 1992. doi: 10.1017/S002211209200003X.

[41] T. Lamson, D. Stinebring, S. Deutsch, G. Rosenberg, and J. Tarbell. Real-time in vitro observation of cavitation in a prosthetic heart valve. *ASAIO transactions*, 37 (3):M351—3, 1991. ISSN 0889-7190. URL `http://europepmc.org/abstract/MED/1751182`.

[42] H. Lee, T. Tsukiya, A. Homma, T. Kamimura, E. Tatsumi, Y. Taenaka, and S. Kita-

mura. A study on the mechanism for cavitation in the mechanical heart valves with an electrohydraulic total artificial heart.

[43] H. Lee, Y. Taenaka, and S. Kitamura. Mechanisms of mechanical heart valve cavitation in an electrohydraulic total artificial heart. *ASAIO journal (American Society for Artificial Internal Organs : 1992)*, 51:208–213, 5 2005. ISSN 1058-2916. doi: 10.1097/01.MAT.0000159383.40133.92.

[44] C. Li, S. Chen, C. Lo, and P. Lu. Role of vortices in cavitation formation in the flow at the closure of a bileaflet mitral mechanical heart valve. *Journal of artificial organs: the official journal of the Japanese Society for Artificial Organs*, 15:57–64, 3 2012. ISSN 1619-0904. doi: 10.1007/S10047-011-0612-6.

[45] W. Li, Z. Gao, Z. Jin, and J. Qian. Transient study of flow and cavitation inside a bileaflet mechanical heart valve. *Applied Sciences*, 10(7), 2020. ISSN 2076-3417. doi: 10.3390/app10072548.

[46] W. Lim, Y. Chew, H. Low, and W. Foo. Cavitation phenomena in mechanical heart valves: the role of squeeze flow velocity and contact area on cavitation initiation between two impinging rods. *Journal of biomechanics*, 36:1269–1280, 9 2003. ISSN 0021-9290. doi: 10.1016/S0021-9290(03)00161-1.

[47] J. Liu, H. Gomez, J. A. Evans, T. J. Hughes, and C. M. Landis. Functional entropy variables: A new methodology for deriving thermodynamically consistent algorithms for complex fluids, with particular reference to the isothermal navier-stokes-korteweg equations. *Journal of Computational Physics*, 248:47–86, 9 2013. doi: 10.1016/J.JCP.2013.04.005.

[48] R. Malinauskas, P. Hariharan, S. Day, L. Herbertson, M. Büsen, U. Steinseifer, K. Aycock, B. Good, S. Deutsch, K. Manning, and B. Craven. Fda benchmark medical device flow models for cfd validation. *ASAIO journal (American Society for Artificial Internal Organs : 1992)*, 63, 01 2017. doi: 10.1097/MAT.0000000000000499.

[49] C. L. Markle. Computational modeling of the dynamics of sheet cavitation. *Proc. 3rd International Symposium on Cavitation*, 2:307–311, 1998.

[50] M. Murtra. The adventure of cardiac surgery. *European Journal of Cardio-Thoracic Surgery*, 21(2):167–180, 02 2002. ISSN 1010-7940. doi: 10.1016/S1010-7940(01)01149-6.

[51] R. Naidoo, B. Pearse, P. Tesar, S.-A. Yap, A. Barnett, and T. Fayers. Long-term

outcomes following medtronic open pivot (TM) valved conduit. *The Journal of Heart Valve Disease*, 23:105–11, 04 2014.

[52] A. Niedźwiedzka, G. H. Schnerr, and W. Sobieski. Review of numerical models of cavitating flows with the use of the homogeneous approach. *Archives of Thermodynamics*, (No 2):71–88, 2016. doi: 10.1515/aoter-2016-0013.

[53] A. Nötzold, A. Khattab, and J. Eggers. Microemboli in aortic valve replacement. *Expert review of cardiovascular therapy*, 4:853–859, 11 2006. ISSN 1744-8344. doi: 10.1586/14779072.4.6.853.

[54] T. Passerini, A. Quaini, U. Villa, A. Veneziani, and S. Canic. Validation of an open source framework for the simulation of blood flow in rigid and deformable vessels. *International journal for numerical methods in biomedical engineering*, 29, 11 2013. doi: 10.1002/cnm.2568.

[55] S. Perdoncin. Numerical validation of a variational multiscale-les turbulence model for blood flows. Master's thesis, Politecnico di Milano., 2019.

[56] M. Plesset and R. Chapman. Collapse of an initially spherical vapour cavity in the neighbourhood of a solid boundary. *Journal of Fluid Mechanics*, 47(2):283–290, 1971. doi: 10.1017/S0022112071001058.

[57] M. S. Plesset. The Dynamics of Cavitation Bubbles. *Journal of Applied Mechanics*, 16(3):277–282, 04 1949. ISSN 0021-8936. doi: 10.1115/1.4009975.

[58] K. Potthast, G. Erdönmez, C. Schnelke, L. Sellin, U. Sliwka, F. Schöndube, M. Eichler, and H. Reul. Origin and appearance of hits induced by prosthetic heart valves: An in vitro study. *The International Journal of Artificial Organs*, 23:441–445, 3 2018. doi: 10.1177/039139880002300706.

[59] J. Qian, Z. Gao, C. Hou, and Z. Jin. A comprehensive review of cavitation in valves: mechanical heart valves and control valves. *Bio-Design and Manufacturing*, 2:119–136, 5 2019. ISSN 2522-8552. doi: 10.1007/S42242-019-00040-Z.

[60] J. Qian, Z. Gao, W. Li, and Z. Jin. Cavitation suppression of bileaflet mechanical heart valves. *Cardiovascular engineering and technology*, 11, 09 2020. doi: 10.1007/s13239-020-00484-w.

[61] A. Quarteroni. *Numerical Models for Differential Problems*, chapter 13. Springer, 2017. ISBN 9783319493152.

[62] A. Quarteroni, R. Sacco, and F. Saleri. *Numerical Mathematics.* Springer-Verlag Berlin Heidelberg, 2007.

[63] E. Rambod, M. Beizaie, M. Shusser, S. Milo, and M. Gharib. A physical model describing the mechanism for formation of gas microbubbles in patients with mitral mechanical heart valves. *Annals of Biomedical Engineering 1999 27:6*, 27:774–792, 1999. ISSN 1573-9686. doi: 10.1114/1.231.

[64] A. J. Reynolds. Thermo-fluid dynamic theory of two-phase flow. *Journal of Fluid Mechanics*, 78:638–639, 12 1976. ISSN 1469-7645. doi: 10.1017/S0022112076212656.

[65] Y. Saad. *Iterative methods for sparse linear systems.* Society for Industrial and Applied Mathematics, 2003.

[66] A. Sambola, J. Osende, J. Hathcock, M. Degen, Y. Nemerson, V. Fuster, J. Crandall, and J. J. Badimon. Role of risk factors in the modulation of tissue factor activity and blood thrombogenicity. *Circulation*, 107:973–977, 2 2003. doi: 10.1161/01.CIR.0000050621.67499.7D.

[67] M. Schäfer, S. Turek, F. Durst, E. Krause, and R. Rannacher. *Benchmark Computations of Laminar Flow Around a Cylinder*, pages 547–566. Vieweg+Teubner Verlag, Wiesbaden, 1996. ISBN 978-3-322-89849-4. doi: 10.1007/978-3-322-89849-4_39.

[68] G. H. Schnerr and J. Sauer. Physical and numerical modeling of unsteady cavitation dynamics. *ICMF-2001, 4th International Conference on Multiphase Flow*, 2001.

[69] H. Schwarz. *Numerical Analysis: A Comprehensive Introduction.* Wiley and Son, 1989.

[70] J. A. Sethian and P. Smereka. Level set methods for fluid interfaces. *Annual Review of Fluid Mechanics*, 35:341–372, 11 2003. doi: 10.1146/ANNUREV.FLUID.35.101101.161105.

[71] F. Shakib, T. J. Hughes, and Z. Johan. A new finite element formulation for computational fluid dynamics: X. the compressible euler and navier-stokes equations. *Computer Methods in Applied Mechanics and Engineering*, 89(1):141–219, 1991. ISSN 0045-7825. doi: https://doi.org/10.1016/0045-7825(91)90041-4. Second World Congress on Computational Mechanics.

[72] D. Shchukin, E. Skorb, V. Belova, and H. Möhwald. Ultrasonic cavitation at solid surfaces. *Advanced Materials*, 23(17):1922–1934, 2011. doi: 10.1002/adma.201004494.

[73] A. K. Singhal, M. M. Athavale, H. Li, and Y. Jiang. Mathematical Basis and Vali-

dation of the Full Cavitation Model . *Journal of Fluids Engineering*, 124(3):617–624, 08 2002. ISSN 0098-2202. doi: 10.1115/1.1486223.

[74] S. Sohrabi and Y. Liu. A cellular model of shear-induced hemolysis. *Artificial Organs*, 41, 12 2016. doi: 10.1111/aor.12832.

[75] D. Spalding. A method for computing steady and unsteady flows possessing discontinuities of density. *CHAM report*, 910(2), 1974.

[76] S. Stewart. Assessment of cfd performance in simulations of an idealized medical device: Results of fda's first computational interlaboratory study. *Cardiovascular Engineering and Technology*, 3:139–160, 2012.

[77] M. Sussman and E. G. Puckett. A coupled level set and volume-of-fluid method for computing 3d and axisymmetric incompressible two-phase flows. *Journal of Computational Physics*, 162(2):301–337, 2000. ISSN 0021-9991. doi: https://doi.org/10.1006/jcph.2000.6537.

[78] J. I. Thornycroft. Torpedo boat destroyers. *Journal of the American Society for Naval Engineers*, 7(4):711–736, 1895.

[79] M. N. Tillquist and T. M. Maddox. Cardiac crossroads: deciding between mechanical or bioprosthetic heart valve replacement. *Patient preference and adherence*, 5:91, 2011. doi: 10.2147/PPA.S16420.

[80] G. Tryggvason, B. Bunner, A. Esmaeeli, D. Juric, N. Al-Rawahi, W. Tauber, J. Han, S. Nas, and Y. J. Jan. A front-tracking method for the computations of multiphase flow. *Journal of Computational Physics*, 169:708–759, 5 2001. ISSN 0021-9991. doi: 10.1006/JCPH.2001.6726.

[81] P. Tullis. *Cavitation Data for Valves*, chapter 6, pages 133–166. John Wiley and Sons, 1989. ISBN 9780470172803. doi: https://doi.org/10.1002/9780470172803.ch6.

[82] O. Vriz, F. Arshi, M. Ahmed, M. Alhumaid, D. Galzerano, S. Emmanual, A. Kinsara, M. Aladmawi, B. Alamro, M. Alshahid, and G. Pedrizzettid. Cavitation phenomenon in mechanical prosthetic valves: Not only microbubbles. *Echocardiography (Mount Kisco, N.Y.)*, 37:876–882, 6 2020. ISSN 1540-8175. doi: 10.1111/ECHO.14692.

[83] C. Zapanta, D. Stinebring, D. Sneckenberger, S. Deutsch, D. Geselowitz, J. Tarbell, A. Synder, G. Rosenberg, W. Weiss, W. Pae, and W. Pierce. In vivo observation of cavitation on prosthetic heart valves. *American Society for Artificial Internal Organs*, 42, 1996. ISSN 1058-2916. doi: 10.1097/00002480-199609000-00047.

[84] V. Zmijanovic, S. Mendez, V. Moureau, and F. Nicoud. About the numerical robustness of biomedical benchmark cases: Interlaboratory fda's idealized medical device. *International Journal for Numerical Methods in Biomedical Engineering*, 33, 03 2016. doi: 10.1002/cnm.2789.

[85] P. Zwart, A. Gerber, and T. Belamri. A two-phase flow model for predicting cavitation dynamics. *Fifth International Conference on Multiphase Flow*, 01 2004.

List of Figures

List of Tables

List of Symbols

Variable	Description	SI unit
α_v, α	vapor volume fraction	-
α_l	liquid volume fraction	-
ρ_v	vapor density	$\mathrm{kg/m^3}$
ρ_l	liquid density	$\mathrm{kg/m^3}$
ρ_m	mixture density	$\mathrm{kg/m^3}$
μ_v	vapor viscosity	Pa·s
μ_l	liquid viscosity	Pa·s
μ_m	mixture viscosity	Pa·s
$\boldsymbol{u}$	mixture velocity	m/s
P	mixture Pressure	Pa
P_v	vapor pressure	Pa
τ	deviatoric stress tensor	Pa
$\dot{S}_\alpha$	vapor-liquid mass tranfer rate	$\mathrm{kg/(m^3 \cdot s)}$
κ	diffusion coefficient	$\mathrm{m^2/s}$
F_{vap}	evaporation coefficient	-
F_{cond}	condensation coefficient	-
r_{nuc}	nucleation volume fraction	-
R_B	nucleation site radius	m
St	Strouhal number	-
Re	Reynolds number	-
Eu	Euler number	-
Re_κ	Reynolds number based on κ	-
σ	cavitation number	-
R_ρ	vapor-liquid density ratio	-
R_μ	vapor-liquid viscosity ratio	-

Acknowledgements

I would like to express my deepest gratitude to my advisor, Luca Dede', who patiently guided me in the development of this thesis. Both me and this work treasured from its commitment, availability and competences. Also, I would like to thank Dr. Ivan Fumagalli and Michele Bucelli, for their priceless support. Their guidance in the development of the mathematical model and its implementation in `life`$^{\texttt{x}}$ have been essential.

I would like to thank also Prof. Stefano Berrone, who accepted to be my co-advisor from the Politecnico di Torino, and the staff of the MOX laboratories, for offering me the computational resources to run my simulations.

I would also like to thank all of my friends from the Aeronautical Engineering course: Edo, Umbe, Vito, Albert, Ste, Tara, Luca, Fede, Raf, Dav and my flat mates Seba and Ale, you made these years special and unforgettable.

Finally, my deep and sincere gratitude to my family for their continuous and unparalleled love, help and support. They selflessly encourage me to explore new directions in life and seek my own destiny. This journey would not have been possible if not for them, and I dedicate this milestone to them.